Gradient echo-based quantitative MRI of human brain at 7T

Mapping of T1, MT saturation and local flip angle

Olsson, Hampus

2021

Document Version:
Publisher's PDF, also known as Version of record

Gradient echo-based quantitative MRI of human brain at 7T

Mapping of T1, MT saturation and local flip angle

HAMPUS OLSSON
DEPARTMENT OF MEDICAL RADIATION PHYSICS | LUND UNIVERSITY

Gradient echo-based quantitative MRI of human brain at 7T

In this thesis, the process of implementing and optimizing quantitative magnetic resonance imaging (qMRI) methodologies based on spoiled gradient-recalled echo (GRE) pulse sequences for whole brain imaging at 7T is described. The thesis tackles 7T-specific challenges in qMRI, especially the increased inhomogeneities of the radio frequency (RF) field (B1) and increased specific absorption rate (SAR). Special attention is given to the mapping of two structural MR parameters linked to longitudinal magnetization, namely T1 and the semi-quantitative magnetization transfer saturation (MTsat) metric. The mapping is performed using either standard spoiled GRE sequences or MPRAGE-based techniques. Emphasis is also put on mapping of the local flip angle, critical for many qMRI methodologies.

Hampus Olsson is a licensed medical physicist and received his M.Sc. in medical radiation physics in 2014.

Printed by Media-Tryck, Lund 2021 NORDIC SWAN ECOLABEL 3041 0903

LUND UNIVERSITY

Department of Medical Radiation Physics
Faculty of Science
Department of Medical Radiation Physics
ISBN 978-91-7895-966-2

Gradient echo-based quantitative MRI of human brain at 7T

Gradient echo-based quantitative MRI of human brain at 7T

Mapping of T1, MT saturation and local flip angle

Hampus Olsson

LUND
UNIVERSITY

DOCTORAL DISSERTATION

by due permission of the Faculty of Science, Lund University, Sweden.
To be defended at Lundmarksalen, Astronomihuset, Sölvegatan 27, Lund, Friday the 29th of October 2021 at 9:00 a.m.

Faculty opponent
Dr. Gisela E. Hagberg, High Field Magnetic Resonance, Max-Planck Institute for Biological Cybernetics, Tübingen, Germany

Organization	Document name
LUND UNIVERSITY	**Doctoral thesis**
Department of Medical Radiation Physics	**Date of issue** **2021-10-05**
Author: Hampus Olsson	Sponsoring organization

Gradient echo-based quantitative MRI of human brain at 7T: Mapping of T1, MT saturation and local flip angle

Abstract

Quantitative MRI (qMRI) refers to the process of deriving maps of MR contrast parameters, such as relaxation times, from conventional images. If the qMRI maps have a high degree of precision and a low degree of bias, they can be compared longitudinally, across subjects, and (ideally) between measurement protocols and research sites. They also provide a more direct biophysical interpretation of the pixel intensities.

The increased magnetization of spins at ultra-high field (UHF) strengths of 7T and above could potentially be translated into higher spatial resolution and/or reduced scan time. This thesis tackles UHF-related challenges in qMRI, namely the increased inhomogeneity of the radio frequency (RF) field (B1) and increased specific absorption rate (SAR). The changing relaxation times (i.e. prolonged T1 and shortened T2) also needs to be accounted for.

Here, spoiled gradient-recalled echo (GRE) techniques are employed to map (primarily) two structural MR parameters, i.e. the longitudinal relaxation time (T1) and the magnetization transfer (MT) saturation (MTsat). Because of its influence at UHF, emphasis is also put on mapping of the local flip angle. Primarily, qMRI is performed by the inversion of analytical signal equations, as opposed to numerical approaches.

The process of implementing and modifying the dual flip angle (DFA) technique in conjunction with an MT-weighted GRE for 7T is described. Implementation is performed within the well-established multi-parameter mapping (MPM) framework and special attention is afforded to the reduction of biases as well as overcoming saftey restrictions imposed by SAR. An approach to obtain high-SNR low-bias flip angle maps at 7T, using the dual refocusing echo acquisition mode (DREAM) technique is also presented. This is important since high fidelity flip angle maps are a prerequisite in DFA-based T1-mapping and recommended for correcting MTsat at UHF. Furthermore, MPRAGE-based techniques are discussed. Firstly, it is demonstrated how to most effectively obtain B1-corrected MPRAGE images of “pure” T1 contrast using a sequential protocol This is followed by a description of T1-mapping using MP2RAGE. Finally, an innovative technique for simultaneous mapping of T1 and the local flip angle is introduced, dubbed “MP3RAGE”.

Key words: T1, MT, Ultra-high field, 7T, spoiled gradient echo, human brain, B1 mapping, dual flip angle, MPRAGE, longitudinal relaxation

Classification system and/or index terms (if any)

Supplementary bibliographical information		**Language: English**
ISSN and key title		**ISBN** **978-91-7895-966-2 (print)** **978-91-7895-965-5 (pdf)**
Recipient’s notes	**Number of pages** **95**	Price
	Security classification	

Gradient echo-based quantitative MRI of human brain at 7T

Mapping of T1, MT saturation and local flip angle

Hampus Olsson

LUND
UNIVERSITY

Cover by Chia-Yen Hsu

Faculty of Science
Department of Medical Radiation Physics

ISBN 978-91-7895-966-2 (print)
ISBN 978-91-7895-965-5 (pdf)

Printed in Sweden by Media-Tryck, Lund University
Lund 2021

Dedicated to the memory of Bonde Ohlsson (1931-2015)

Table of Contents

Abstract

Quantitative MRI (qMRI) refers to the process of deriving maps of MR contrast parameters, such as relaxation times, from conventional images. If the qMRI maps have a high degree of precision and a low degree of bias, they can be compared longitudinally, across subjects, and (ideally) between measurement protocols and research sites. They also provide a more direct biophysical interpretation of the pixel intensities.

The increased magnetization of spins at ultra-high field (UHF) strengths of 7T and above could potentially be translated into higher spatial resolution and/or reduced scan time. This thesis tackles UHF-related challenges in qMRI, namely the increased inhomogeneity of the radio frequency (RF) field (B1) and increased specific absorption rate (SAR). The changing relaxation times (i.e. prolonged T1 and shortened T2) also needs to be accounted for.

Here, spoiled gradient-recalled echo (GRE) techniques are employed to map (primarily) two structural MR parameters, i.e. the longitudinal relaxation time (T1) and the magnetization transfer (MT) saturation (MTsat). Because of its influence at UHF, emphasis is also put on mapping of the local flip angle. Primarily, qMRI is performed by the inversion of analytical signal equations, as opposed to numerical approaches.

The process of implementing and modifying the dual flip angle (DFA) technique in conjunction with an MT-weighted GRE for 7T is described. Implementation is performed within the well-established multi-parameter mapping (MPM) framework and special attention is afforded to the reduction of biases as well as overcoming safety restrictions imposed by SAR. An approach to obtain high-SNR low-bias flip angle maps at 7T, using the dual refocusing echo acquisition mode (DREAM) technique is also described. This is important since high fidelity flip angle maps are a prerequisite in DFA-based T1-mapping and recommended for correcting MTsat at UHF. Furthermore, MPRAGE-based techniques are discussed. Firstly, it is demonstrated how to most effectively obtain B1-corrected MPRAGE images of "pure" T1 contrast using a sequential protocol This is followed by a description of T1-mapping using MP2RAGE. Finally, an innovative technique for simultaneous mapping of T1 and the local flip angle is introduced, dubbed "MP3RAGE".

Populärvetenskaplig sammanfattning

Största delen av den mänskliga kroppen består av vatten. Vattnets kärnmagnetiska egenskaper utnyttjas inom magnetresonanstomografi (MRT) till att avbilda kroppens insida. Jämfört med till exempel röntgen är MRT mycket bra på att urskilja olika sorters mjukvävnad såsom vit och grå hjärnsubstans. I konventionell MRT är pixelvärdena i den digitala bilden av en arbiträr natur och kan vara svåra att tolka. Utöver detta är konventionella MRT-bilder generellt sett inte jämförbara när de har upptagits vid olika tillfällen eller med olika magnetkameror. Detta är ett problem både inom forskning och i kliniska tillämpningar, exempelvis när en läkare vill följa hur en patient svarar på en viss behandling.

Kvantitativ MRT använder matematiska samband mellan den uppmätta signalen, inställningar på magnetkameran, och underliggande egenskaper hos den avbildade vävnaden till att beräkna dessa vävnadsspecifika egenskaper. De olika ”MR-parametrarna” är känsliga för olika förhållanden i kroppen, till exempel mängden järn eller hur friska nervtrådarna är. Genom kvantitativ MRT omvandlas magnetkameran från att vara ”bara en kamera” till ett vetenskapligt mätinstrument från vilket ”kartor” över vävnadsspecifika parametrar kan erhållas. Två centrala MR-parametrar i denna avhandling är den ”longitudinella relaxationstiden, T_1” samt ”magnetization transfer saturation”.

Alla magnetkameror genererar ett statiskt magnetiskt fält som alltid är aktivt. Styrkan på detta fält anges i enheten tesla (T) och är på kliniska kameror vanligtvis 1.5 T eller 3.0 T. Ett starkare magnetiskt fält betyder generellt en högre signal vilket kan användas till att öka detaljskärpan (upplösningen) och/eller minska undersökningstiden. En högre fältstyrka kan dock även innebära svårigheter eftersom den uppmätta signalen tenderar att bli olika stark på olika ställen i kroppen. Ett annat potentiellt problem är att uppvärmningen av kroppen under undersökningen ökar.

I denna avhandling har olika kvantitativa MRT-metoder implementerats på en magnetkamera med fältstyrkan 7 T i syfte att kartlägga de två ovanstående MR-parametrarna i den mänskliga hjärnan. Arbetet har resulterat i att metoderna levererat mer exakta resultat, genom att korrigera för, eller helt undvika, olika sorters felkällor. De implementerade metoderna innefattar beprövade tekniker som modifierats utefter förutsättningarna på 7 Tesla såväl som en helt ny teknik som kan kartlägga två parametrar samtidigt.

Original papers

The thesis is based on the following publications and manuscripts, referred to by their roman numerals:

I. Olsson H, Novén M, Lätt J, Wirestam R, Helms G. Radiofrequency bias correction of magnetization prepared rapid gradient echo MRI at 7.0 Tesla using an external reference in a sequential protocol. Tomography 2021;7(3). doi: 10.3390/tomography7030038.

II. Olsson H, Andersen M, Lätt J, Wirestam R, Helms G. Reducing bias in dual flip angle T1-mapping in human brain at 7T. Magn Reson Med 2020;84(3):1347-1358. doi: 10.1002/mrm.28206.

III. Olsson H, Andersen M, Helms G. Reducing bias in DREAM flip angle mapping in human brain at 7T by multiple preparation flip angles. Magn Reson Imaging 2020;72:71-77. doi: 10.1016/j.mri.2020.07.002.

IV. Olsson H, Andersen M, Wirestam R, Helms G. Mapping magnetization transfer saturation (MTsat) in human brain at 7T: Protocol optimization under specific absorption rate constraints. Magn Reson Med. 2021; 00: 1-15 (Early View). doi:10.1002/mrm.28899.

V. Olsson H, Andersen M, Kadhim M, Helms G. MP3RAGE – Simultaneous mapping of T1 and B1+ in human brain at 7T. Submitted to Magn Reson Med. Under revision.

List of contributions

This is a summary of my contributions to each paper in this thesis.

I. I participated in the experimental setup and acquisition of the data. I evaluated the data, prepared the figures and developed the lookup table approach for T_1 quantification. I was the main author of the paper.

II. I participated in the experimental setup, sequence programming and acquisition of the data. I evaluated the data, prepared the figures and developed methods for validation. I was the main author of the paper.

III. I participated in the experimental setup and acquisition of the data. I evaluated the data and prepared the figures. I was the main author of the paper.

IV. I participated in the experimental setup, sequence programming and acquisition of data. I evaluated the data, prepared the figures and calibrated the B_1^+ correction for 7T. I was the main author of the paper.

V. I participated in the conceptualization of the idea and took initiative to ensure its realization. I participated in the experimental setup, sequence programming and data collection. I was the main author of the manuscript.

Papers not included in this thesis

I. Novén M, Olsson H, Helms G, Horne M, Nilsson M, and Roll M. Cortical and white matter correlates of language-learning aptitudes. Human Brain Mapping, 2021;42(15):5037-5050. doi:10.1002/hbm.25598.

II. Helms G, Lätt J, and Olsson H. 2020. Cross-vendor transfer and RF coil comparison of high-resolution MP2RAGE protocol for brain imaging at 7T, Acta Scientiarum Lundensia, 2020: 1-12.

III. Lundberg A, Lind E, Olsson H, Helms G, Knutsson L, Wirestam R. Comparison of MRI methods for measuring whole brain oxygen extraction fraction under different geometric conditions at 7T. Unpublished manuscript.

Common Abbreviations

BSB	Binary spin bath
CNR	Contrast to noise ratio
DFA	Dual flip angle
DREAM	Dual refocusing echo acquisition mode
EPI	Echo-planar imaging
GM	Gray matter
GRE	Gradient-recalled echo
hMRI	In vivo histology using magnetic resonance imaging
IR	Inversion recovery
LUT	Lookup table
MPM	Multi-parameter mapping
MPRAGE	Magnetization prepared rapid gradient echo
MP2RAGE	Magnetization prepared 2 rapid gradient echoes
MT	Magnetization transfer
MTR	Magnetization transfer ratio
MT_{sat}	Manetization transfer saturation
PD	Proton density
PSF	Point spread function
qMRI	Quantitative MRI
qMT	Quantitative magnetization transfer
SAR	Specific absorption rate
SNR	Signal to noise ratio
UHF	Ultra-high field
VFA	Variable flip angle
WM	White matter

Mathematical symbols

M_z	Longitudinal magnetization
M_0	Longitudinal magnetization at thermal equilibrium
M_0^*	Longitudinal magnetization at driven equilibrium
S	Signal amplitude
A	Maximum signal amplitude
A_{app}	Apparent maximum signal amplitude
T_1	Longitudinal relaxation time
$T_{1,app}$	Apparent longitudinal relaxation time
T_1^*	Time constant with which M_z approaches M_0^*
$T_{1,s}$	Longitudinal relaxation time biased by incomplete spoiling
T_2	Transverse relaxation time
T_2^*	Effective transverse relaxation time
TI	Inversion time
TR	Repetition time
TE	Echo time
TD	Time from last excitation to next inversion
TC	Cycle duration
TF	Turbo factor
ω_1	Amplitude of RF pulse
α	Nominal flip angle
α_{loc}	Local flip angle
f_T	Transmit field bias
f_R	Receive field bias
f_{inv}	Inversion efficiency
δ_{MT}	MT_{sat} calculated using local flip angles
$\delta_{MT,app}$	MT_{sat} calculated using nominal flip angles
$\delta_{MT,corr}$	MT_{sat} corrected for residual transmit field bias
$\delta_{MT,inc}$	Incidental MT_{sat} caused by excitation pulse
δ_b	Instantaneous saturation of bound pool
δ_f	Instantaneous saturation of free pool
F_b	Bound pool fraction
$g_b(\Delta, T_{2b})$	Bound pool absorption lineshape
Δ	MT pulse offset frequency
t_{RF}	Duration of excitation pulse
t_{sat}	Duration of MT pulse
Q	Pulse shape factor

1 - Introduction and aims

Magnetic resonance imaging (MRI) utilizes the interactions between the magnetic moments of hydrogen nuclei and externally applied electromagnetic fields to produce anatomical images of high resolution, wide coverage, and excellent soft tissue contrast. Different types of contrast can be obtained by careful tailoring of the externally applied electromagnetic fields to emphasize a particular biophysical MR parameter. Such parameters include, for instance, the longitudinal relaxation time, T_1, the transverse and effective transverse relaxation times, T_2 and T_2^*, proton density (PD), magnetization transfer (MT) and diffusion. In conventional MRI, the image results from a mixture of MR parameters, but is said to be "weighted" by whichever parameter dominates the contrast. The measured signal depends nonlinearly on the MR parameters, as well as on imaging protocol, subject positioning and scanner hardware. The values of individual pixels, that collectively make up the image, thus lacks strict physical meaning and are generally not comparable across scanning sessions, subjects or research sites.

Quantitative MRI (qMRI) addresses this issue by converting the arbitrary pixel intensities into physical units to obtain a "map" of a specific MR parameter, thus transforming the MR scanner from merely an imaging device to a scientific measurement instrument. Performing qMRI generally requires the acquisition of more than one image. The images are then used to solve an inverse problem (either numerically or analytically) on a pixelwise level, thus obtaining a quantitative map (Nikolaus Weiskopf, Edwards, Helms, Mohammadi, & Kirilina, 2021). This is often followed up by some form of correction for expected biases, such as deviations from the nominal flip angle. Given that the bias is sufficiently low, and that the precision is sufficiently high, these maps can be compared in longitudinal studies, across large cohorts and (ideally) between different scanners and imaging protocols (Stikov et al., 2015; Voelker et al., 2021). Bias refers to a systematic error not accounted for in the qMRI methodology and can be estimated by comparison to a gold-standard reference technique. Precision refers to a random variability, either in a scan-rescan experiment performed during the same session and under identical conditions (repeatability) or under differing conditions such as different MRI scanners and/or separated by long-time intervals (reproducibility) (Kessler et al., 2015). It can be important to consider what degree of precision is needed for a certain purpose, and what amount of bias can be tolerated since improvements often entail an increase in scan time which is very precious in MRI.

A semi-quantitative technique refers to when the MR signal is normalized to some reference and denoted by a fraction or in percent units (p.u.). It pertains to obtain a "pure" contrast, i.e. dependent on only one MR parameter. Although it lacks a direct biophysical interpretation, and will vary based on pulse sequence parameters, it shares the improved reproducibility of a fully quantitative parameter in contrast to conventional MRI. A semi-quantitative approach is typically less time consuming than a fully quantitative one. The importance of achieving low bias and high repeatability applies to a semi-quantitative methodology as much as a fully quantitative one, and it is therefore considered a subset of qMRI in this thesis.

MRI scanners come with different strengths of the static magnetic field, B_0. Clinical MRI scanners typically operate at 1.5T or 3T. Ultra-high field (UHF) strengths refer to B_0 values of 7T or above and have become increasingly prevalent in recent years (Barisano et al., 2019). Increasing B_0 enhances the magnetization of the hydrogen nuclei in thermal equilibrium which *generally* translates into a higher signal to noise ratio (SNR) (Balchandani & Naidich, 2015). The higher SNR can alternatively be traded for either higher resolution or decreased scan time by alterations to the pulse sequence. Relaxation times change at higher B_0 as T_1 is prolonged while T_2 and T_2^* are shortened (Oros-Peusquens, Laurila, & Shah, 2008; Rooney et al., 2007). Depending on pulse sequence and application, this can be either a benefit or a detriment. Other effects are an increased sensitivity to susceptibility effects as well as an increased separation between metabolic peaks (Ugurbil et al., 2003). Further, the spatial inhomogeneities of both the B_0 field and the radio frequency (RF) B_1 field increases (Stockmann & Wald, 2018; Vaughan et al., 2001). Especially the inhomogeneity of the B_1 field, which governs both the local flip angle through the transmit (B_1^+) component as well as the receiver sensitivity, poses a great challenge for qMRI at 7T. Lastly, the specific absorption rate (SAR) increases quadratically with B_0 which acts as a bottle neck when frequent high-power pulses are used, as in MT experiments.

In this thesis, the process of implementing and optimizing qMRI methodologies based on spoiled gradient recalled echo (GRE) pulse sequences for whole brain imaging at 7T is described. Methodologies based on both the standard spoiled GRE sequence, acquired entirely in the steady state, as well as the magnetization prepared rapid gradient echo (MPRAGE) sequence is treated. Special attention is given to the mapping of two MR parameters linked to structural MRI, namely T_1 and the semi-quantitative magnetization transfer saturation (MT_{sat}) metric. Emphasis is also put on mapping of the local flip angle, critical for most qMRI methodologies at 7T.

The aims of the projects included in this thesis were to

I. Implement and evaluate a reference GRE for normalization in MPRAGE imaging, to obtain semi-quantitative T_1-weighted images

II. Implement and reduce bias in a dual flip angle (DFA) T_1-mapping protocol

III. Introduce a methodology to reduce bias in dual refocusing echo acquisition mode (DREAM) flip angle mapping

IV. Maximize MT under SAR constraints in an MT_{sat}-mapping protocol while avoiding bias

V. Introduce and implement a novel "MP3RAGE" approach for simultaneous mapping of T_1 and the local flip angle

2 – Background

This chapter serves as a review of the theoretical concepts on which the work of this thesis is based. The basics of MR physics, including T_1-relaxation, is explained through the phenomenological Bloch equations (Bloch, 1946). To explain the phenomenon of MT, the Bloch equations are expanded to include exchange with a second pool of motionally restricted spins, forming the Bloch-McConnel equations (McConnell, 1958). The biophysical origin of T_1 and MT is discussed, as well as some common applications in neuroscientific research. Lastly, some of the most well-established techniques used to measure T_1 and MT are briefly described.

Bloch equations

Hydrogen nuclei (protons) possess a spin angular momentum, $\mathbf{J}$, which gives them a magnetic moment, $\boldsymbol{\mu} = \gamma\mathbf{J}$, where $\gamma = 2\pi \times 42.58$ MHz/T is the gyromagnetic ratio. For an ensemble of spin isochromats, the net magnetization is denoted $\mathbf{M} = (M_x, M_y, M_z)$. If an external magnetic field, $\mathbf{B} = (B_x, B_y, B_z)$, is applied, $\mathbf{M}$ experiences a torque, $\boldsymbol{\tau} = \mathbf{M} \times \mathbf{B}$, causing precession around $\mathbf{B}$. This is described by the equation of motion (Bloch, 1946):

$$d\mathbf{M}/dt = \mathbf{M} \times \gamma\mathbf{B}, \tag{2.1}$$

where the angular frequency of precession is given by the Larmor equation as $\omega = \gamma|\mathbf{B}|$. Replacing the generic $\mathbf{B}$ by the static magnetic field $\mathbf{B_0} = (0,0,B_0)$ (by definition in the longitudinal direction) where $B_0 = 7$ T, the Larmor frequency of water is obtained:

$$\nu_0 = \frac{\omega_0}{2\pi} = \frac{\gamma}{2\pi} B_0 = 298.06 \text{ MHz}. \tag{2.2}$$

To achieve resonance, a time-varying RF field, $\mathbf{B_1}$, with carrier frequency ω close to ω_0 and amplitude ω_1, is applied perpendicular to $\mathbf{B_0}$. To simplify the behaviour of $\mathbf{M}$, the rotating frame of reference is introduced which rotates like $\mathbf{B_1}$ with ω around $\mathbf{B_0}$. In this frame, $\mathbf{B_1} = (B_1, 0,0)$ is fixed and $\mathbf{M}$ precesses around the

oblique effective field $\mathbf{B}_\mathrm{e} = \mathbf{B}_1 \times (\mathbf{B}_0 - \hat{\boldsymbol{z}}\,\omega/\gamma)$ instead of $\mathbf{B}_0$, where $\hat{\boldsymbol{z}} = (0,0,1)$ is a unit vector. Deriving the three components of $\mathbf{M}$ from Eq. (2.1) and transforming them to the rotating frame yields:

$$dM_\mathrm{x}/dt = (\omega_0 - \omega)M_\mathrm{y}, \tag{2.3a}$$

$$dM_\mathrm{y}/dt = -(\omega_0 - \omega)M_\mathrm{x} + \omega_1 M_z, \tag{2.3b}$$

$$dM_\mathrm{z}/dt = -\omega_1 M_\mathrm{y}. \tag{2.3c}$$

The precession of $\mathbf{M}$ around $\mathbf{B}_\mathrm{e}$ rotates (or nutates) $\mathbf{M}$ towards the transverse plane where a signal magnitude proportional to $\left|\mathbf{M}_\mathrm{xy}\right| = \sqrt{M_x^2 + M_y^2}$ is induced in a receiver coil. The phase $\phi = \tan^{-1}\left(M_\mathrm{y}/M_\mathrm{x}\right)$ of $\mathbf{M}_\mathrm{xy}$ can also be obtained if the signal is measured in quadrature mode. In this case, the signal is complex, where the real part of the signal denotes the x-axis and the imaginary part denotes the y-axis.

The magnetization will also undergo two forms of relaxation governed by two phenomenological time constants. First, there is the longitudinal or "spin-lattice" relaxation which governs the return of M_z to its thermal equilibrium value, M_0, by T_1. Secondly, there is the transverse or "spin-spin" relaxation which describes the dephasing of the spin isochromats and subsequent decay of M_x and M_y by $T_2 \leq T_1$. Adding relaxation terms to Eq. (2.3) yields the full Bloch equations in the rotating frame (de Graaf, 2018):

$$dM_\mathrm{x}/dt = (\omega_0 - \omega)M_\mathrm{y} - M_\mathrm{x}/T_2, \tag{2.4a}$$

$$dM_\mathrm{y}/dt = -(\omega_0 - \omega)M_\mathrm{x} + \omega_1 M_z - M_\mathrm{y}/T_2, \tag{2.4b}$$

$$dM_\mathrm{z}/dt = -\omega_1 M_\mathrm{y} + \frac{M_0 - M_\mathrm{z}}{T_1}. \tag{2.4c}$$

In the special case of perfect on-resonance, i.e. $\omega = \omega_0$ and $\mathbf{B}_\mathrm{e}(t) = \mathbf{B}_1(t)$, the Bloch equations simplify to:

$$dM_x/dt = 0, \tag{2.5a}$$

$$dM_y/dt = \omega_1 M_z - M_y/T_2, \tag{2.5b}$$

$$dM_z/dt = -\omega_1 M_y + \frac{M_0 - M_z}{T_1}. \tag{2.5c}$$

After B_1 has been applied on-resonance for a certain duration, t_{RF}, there exists a fixed angle which **M** has been tilted away from the longitudinal z-axis. This angle is referred to as the flip angle:

$$\alpha = \gamma \int_0^{t_{RF}} B_1(t) = \int_0^{t_{RF}} \omega_1(t) dt. \tag{2.6}$$

Eq. (2.6) implies that $\omega_1(t)$ can be time-dependent during t_{RF}, described by the pulse shape envelope of $B_1(t)$. However, since $t_{RF} \ll T_2$ for many pulse sequences (hence the term RF "pulse"), the Bloch equations can often be separated into periods of instantaneous irradiation followed by periods of free relaxation. In this way, the Bloch equations can be numerically simulated using matrix operators applied to **M**. These operators are for irradiation (Yarnykh, 2010):

$$\mathbf{R} = \begin{bmatrix} 1 & 0 & 0 \\ 0 & \cos\alpha & \sin\alpha \\ 0 & -\sin\alpha & \cos\alpha \end{bmatrix}, \tag{2.7}$$

and for relaxation:

$$\mathbf{E} = \begin{bmatrix} E_2 \cos\psi_l & E_2 \sin\psi_l & 0 \\ -E_2 \sin\psi_l & E_2 \cos\psi_l & 0 \\ 0 & 0 & E_1 \end{bmatrix}, \tag{2.8}$$

where $E_1 = \exp(-TR/T_1)$, $E_2 = \exp(-TR/T_2)$, TR is the repetition time (time between excitation RF pulses) and $\psi_l = l \cdot 2\pi/(N-1)$ with index $l = 0,1,\ldots,N$ denoting a spatially unique phase for each of the N spin isochromats (needed to simulate T_2 decay).

Under the assumption of instantaneous irradiation interspersed by intervals of relaxation, it is often possible to derive analytical signal equations from the more fundamental Bloch equations. A famous example is the Ernst equation, describing spoiled gradient echoes (Ernst & Anderson, 1966). In this thesis, qMRI was based

mainly on such signal equations. In particular, the rational approximation for small flip angles and short TR was used to facilitate the calculation of, for example, T_1, by analytical inversion (Helms, Dathe, & Dechent, 2008).

The longitudinal relaxation time: T_1

Definition and biophysical origin

The longitudinal relaxation time, T_1, describes how rapidly the longitudinal magnetization, $M_z(t)$, of an ensemble of spins return to M_0 after absorption of energy through RF irradiation. Relaxation is facilitated by transfer of excess energy from the spins to a "lattice" of surrounding molecules, and it is thus sometimes referred to as spin-lattice relaxation. The process is exponential and the time constant T_1 is of the order of a second. Solving the longitudinal relaxation part of equations (2.4c) and (2.5c), $dM_z/dt = (M_0 - M_z)/T_1$, yields:

$$M_z(t) = M_0 + (M_z(0) - M_0)\exp(-t/T_1). \tag{2.9}$$

The presence of macromolecules as well as iron has a shortening effect on T_1 (Callaghan, Helms, Lutti, Mohammadi, & Weiskopf, 2015). In vivo, myelin forms sheaths around the axons while iron is stored inside ferritin proteins or in the blood (Schenck & Zimmerman, 2004). Consequently, T_1 in CSF is much longer than in tissue while white matter (WM) experiences a shorter T_1 than gray matter (GM) due to its higher concentration of myelinated axons and overall macromolecular content. In cortical GM, T_1 has been used as a surrogate parameter of myelination (Lutti, Dick, Sereno, & Weiskopf, 2014). Further, increased iron concentration results in slightly shorter T_1 in deep brain GM compared to cortical GM (Vymazal et al., 1999). Likewise, blood shows a shorter T_1 than CSF albeit not as short as tissue (Rooney et al., 2007).

Applications in neuroscience

Mapping of T_1 can be useful in the study of demyelinating disorders such as multiple sclerosis (MS) where WM and GM that appear normal on conventional MRI have shown prolonged T_1 in relapsing-remitting patients (Davies et al., 2007; Griffin et al., 2002). The connection to iron, makes T_1-mapping suitable to study Parkinson's disease (Vymazal et al., 1999) where excess iron (outside the ferritin) is prevalent (Dexter, Jenner, Schapira, & Marsden, 1992). Changes in T_1 are, however, not as specific to iron as T_2^* or quantitative susceptibility mapping (QSM). It has been suggested that T_1 could be more useful to study progression of Parkinson's disease

in the form of general neuronal loss (Baudrexel et al., 2010), while T_2* or QSM could be used to measure iron accumulation in the basal ganglia, specifically the substantia nigra (Baudrexel et al., 2010; Langkammer et al., 2016; Loureiro et al., 2018; Nurnberger et al., 2017). Similarly, tumor progression in glioblastoma patients has been detected earlier compared to conventional MRI by using T_1-mapping to measure the spread of malignant cells outside the gross tumor volume (Lescher et al., 2015).

Inversion recovery (IR)

The gold-standard method for measuring T_1 is a single-slice inversion recovery (IR) experiment where after inversion and a subsequent waiting period, TI, magnetization is excited into the transverse plane and measured. This is repeated for $n = 1,2, \dots, N$ different values of TI and the acquired signal, S_n, is fitted (e.g. using the Levenberg-Marquardt algorithm) to a three-parameter model:

$$|S_\mathrm{n}| = \left|A\left(1 - 2f_\mathrm{inv}\exp(-TI_\mathrm{n}/T_1)\right)\right|, \tag{2.10}$$

where A is the hypothetical signal maximum at M_0 ($TI_\mathrm{n} \to \infty$) and f_inv is the efficiency of the, likely imperfect, inversion pulse. Here, the modulus of the signal equation is used to denote that the polarity of M_z is unknown. In the experiments pertaining to Papers II and V, Eq. (2.10) was used to validate the respective T_1-mapping protocols suggested.

A common rule-of-thumb is to allow a period of free relaxation of $TD = 5 \times T_1$ between excitation and the next inversion to allow M_z to return to equilibrium (Kingsley, 1999). However, it has been claimed that setting TR significantly longer than the longest TI improves neither accuracy nor precision, provided a three-parameter model is used (Kingsley & Monahan, 2001). Because of this, the reference phantom measurements reported in Paper II were performed with $TR = 10$ s and a maximum $TI_N = 4000$ ms which would only allow full relaxation for T_1 values up to 1200 ms.

Another important aspect to consider, is the choice of minimum TI. It is common and sometimes recommended that the minimum TI is set as short as possible to maximize precision (Kingsley & Monahan, 2001). However, the monoexponential behaviour hitherto implied by the Bloch equations is an oversimplification of the multi-compartment environment typically present within a voxel. In the two-pool bi-exponential model, this environment is described by a free pool with long T_1 ($T_{1\mathrm{f}}$) and a macromolecular pool with short T_1 ($T_{1\mathrm{b}}$) as well as MT between the two pools in either direction. Assuming a monoexponential behaviour immediately after inversion will lead to a reduction in the observed T_1 as magnetization returns more

quickly to equilibrium through MT. This is especially noticeable in WM where the macromolecular fraction (short T_1 component) is larger. Such "inverse MT" (from the free to the macromolecular pool) is induced because of the low power of the inversion pulse. It has, for instance, been observed that adiabatic pulses does not saturate non-aqueous signal (Reynolds et al., 2021). The issue is circumvented by choosing a minimum $TI \geq 200$ ms. From this time point and onwards, equilibrium between the two pools has been re-established at 7T and MT effects can be ignored (Rioux, Levesque, & Rutt, 2016). Such a minimum TI was thus set for the in vivo reference IR measurements in Papers II and V.

To save time when TR is long, phase encoding is often performed using a turbo spin echo (TSE) sequence where, following an inversion, a number of refocusing pulses are applied which result in an equal number of spin echoes (Hennig, Nauerth, & Friedburg, 1986). Scan time is reduced compared to a classic spin-echo sequence by the number of echoes acquired in each cycle, i.e. the echo train length (ETL). Alternatively, an echo planar imaging (EPI) sequence which can be either GRE- or spin echo-based, can be used (Stehling, Ordidge, Coxon, & Mansfield, 1990). In spin echo-based EPI, only one refocusing pulse is applied before the echo train. Consequently, there is no risk of unwanted stimulated echo pathways forming due to non-180° refocusing pulses (Hinks & Constable, 1994). In "single-shot" encoding, the whole of k-space is sampled within one echo train. This manifests as chemical shift artifacts in the phase encoding direction, governed by the phase encoding bandwidth. Such artifacts can be suppressed by a spectrally selective inversion pulse applied at such a time that the fat signal is saturated during readout (i.e. "fat suppression") (Kaldoudi, Williams, Barker, & Tofts, 1993). Also because of the very low phase encoding bandwidth, spatial distortions in the form of elongation/contractions occurs in the presence of B_0 inhomogeneities causing susceptibility differences (Zhou et al., 1998). An effective way to limit such distortions is to reduce the ETL through parallel imaging techniques such as SENSE (Pruessmann, Weiger, Scheidegger, & Boesiger, 1999) or to use a "multi-shot" acquisition. If a separately acquired B_0 map is acquired, distortions can be "un-warped" with post-processing tools such as FSL FUGUE (FMRIB's Utility for Geometrically Unwarping EPIs). Blurring in the phase encoding direction due to different T_2-weightings for different k-space lines may occur. The blurring is not as severe as in TSE or 3D imaging because of the shorter effective TE, but more severe than in multi-shot imaging. It can similarly be reduced by increasing the SENSE factor. For the phantom reference measurement described in Paper II, a multi-shot 2D IR-EPI with a SENSE reduction factor of 2.5 was used. For the in vivo reference measurements described in Paper II and V, a single-shot sequence was used to reduce motion sensitivity. The EPI distortions were then corrected for during post processing using FSL FUGUE.

Variable flip angle method (VFA)

The gold-standard IR experiment is much too slow to allow for high-resolution T_1-mapping in 3D. A more effective approach is to determine T_1 by varying the flip angle, first introduced in a non-clinical nuclear magnetic resonance (NMR) setting by Christensen, Grant, Schulman, & Walling) (1974). The VFA principle is favorably combined with the 3D spoiled GRE sequence, known as either FLASH, SPGR or T1-FFE depending on vendor (Haase, Frahm, Matthaei, Hanicke, & Merboldt, 1986). In this context, the VFA technique has been named driven-equilibrium single-pulse observation of T_1 relaxation (DESPOT) (Homer & Beevers, 1985). It was later popularized as DESPOT1 when used to obtain T_1 maps with whole-brain coverage at 1 mm isotropic resolution (Deoni, Rutt, & Peters, 2003).

The signal, S, of the spoiled GRE is primarily governed by M_z, which after a sufficient number of TR periods is in a steady state. The steady state signal is in turn determined by T_1, TR and the local flip angle, $f_T\alpha$, where f_T is the ratio of the local to the nominal (α) flip angle and thus represents the local transmit (B_1^+) field bias. From here on, f_T will be inserted in all signal equations to emphasize the large deviations from the nominal flip angle experienced at UHF. Using these variables, the spoiled GRE steady state signal is analytically described by the Ernst equation (Ernst & Anderson, 1966):

$$S(f_T\alpha) = A\sin(f_T\alpha)\frac{1-\exp(-TR/T_1)}{1-\cos(f_T\alpha)\exp(-TR/T_1)}, \tag{2.11}$$

where A is the signal amplitude acquired with $f_T\alpha = 90°$ at thermal equilibrium ($TR \gg T_1$). The signal is maximized for a certain f_T and tissue T_1 at the Ernst angle:

$$\alpha_E(f_T) = \cos^{-1}\big(\exp(-TR/T_1)\big)/f_T. \tag{2.12}$$

To obtain a function of the form $y = mx + b$ from which T_1 can be determined through linear regression, Eq. (2.11) is rearranged as:

$$\frac{S}{\sin(f_T\alpha)} = \exp\left(-\frac{TR}{T_1}\right)\frac{S}{\tan(f_T\alpha)} + A\left(1-\exp\left(-\frac{TR}{T_1}\right)\right), \tag{2.13}$$

where T_1 is determined from the slope m as $T_1 = -TR/\ln(m)$ and A from the intercept b as $A = b/(1-m)$.

If the VFA experiment consists of only two flip angles, i.e. a dual flip angle (DFA) experiment, T_1 can be solved for analytically through the elementary slope equation

although the derived expressions are rather unwieldly and not very intuitive. In Chapter 3, the rational approximation for small flip angles and short TR will be introduced which yields simple intuitive expressions for T_1 and A (Helms, Dathe, & Dechent, 2008).

The VFA technique is popular because of its simplicity, speed, high SNR per unit time and potential whole-brain coverage. A problem is the inherent quadratic f_{T} dependence, making accurate and precise external flip angle mapping mandatory even at non-UHF strengths. The precision of the flip angle map will greatly affect the precision of the T_1 map (Lee, Callaghan, & Nagy, 2017). It is not unlikely that the increased sensitivity to variations in the RF coil setup leads to the somewhat worse reproducibility observed for VFA-derived T_1 maps compared to the interleaved MP2RAGE (Voelker et al., 2021). It has further been shown to result in higher T_1 estimates compared to inversion recovery (Stikov et al., 2015). This could either be due to imperfect spoiling or incidental MT effects (A. G. Teixeira et al., 2020; Preibisch & Deichmann, 2009), both of which will be treated in Chapter 3.

MP2RAGE

Mapping of T_1 through the magnetization prepared 2 rapid acquisition gradient echoes (MP2RAGE) sequence (Marques et al., 2010) has become very popular and has shown a very high degree of reproducibility across sites (Voelker et al., 2021). As the signal dependence is more complicated than in the spoiled GRE, it becomes difficult to obtain an analytical solution for T_1. Thus, a lookup table- (LUT-) based approach facilitated by forward signal modeling is the method of choice. MP2RAGE will be covered in more detail in Chapter 5.

Magnetization transfer (MT)

Definition and biophysical origin

MT is a unique contrast mechanism inherent to tissue where magnetization is transferred from protons in rotationally restricted water bound to macromolecules, to protons in rotationally free water (Henkelman, Stanisz, & Graham, 2001; Wolff & Balaban, 1989). A macromolecule is characterized by its reduced mobility, e.g. due to its size or being part of a membrane. It includes, for instance, proteins and phospholipids which comprise the dry mass in myelin. The strong coupling of neighbouring protons leads to almost instant dephasing of signal and a very broad absorption lineshape. To induce MT, a high-energy RF pulse is applied off-resonance, targeting this broad absorption lineshape. Through cross-relaxation, the magnetization is dispersed within the macromolecule (spin diffusion), transferred to

the bound water and then to the free water. Macromolecular content can thus be indirectly detected as a decrease in signal amplitude. Since the transverse magnetization of the bound pool dephases during the MT pulse itself, the concepts of "excitation" and "flip angle" does not apply. Hence, the MT is always in the form of a saturation and cannot result in echo formation. MT between bound and free water can also manifest through the exchange of the protons themselves, i.e. chemical exchange saturation transfer (CEST). CEST resonances are much narrower and relate to specific macromolecular groups, unlike the broad lineshape of the "general" macromolecular resonance. Due to the longer T_2, CEST can result in transfer of transverse magnetization and not just saturation transfer (van Zijl, Lam, Xu, Knutsson, & Stanisz, 2018). Cross-relaxation is, however, believed to be the dominant mechanism in a standard MT experiment where the general macromolecular lineshape is targeted, as was done in the experiments pertaining to Paper IV.

Applications in neuroscience

MT is more sensitive to demyelination than T_1 (Janve et al., 2013). It is therefore often used in studies of multiple sclerosis (Filippi & Agosta, 2007). Particularly remitting-relapsing multiple sclerosis where each relapse is often accompanied by a new WM lesion (De Stefano et al., 2006; York, Thrippleton, Meijboom, Hunt, & Waldman, 2021).

Experimental considerations

MT techniques were traditionally developed in non-clinical NMR settings. In such environments, MT is often induced using long periods (0.1-1.0 s) of continuous wave irradiation. This produces a very narrow frequency response which heavily saturates the macromolecules while leaving free water unaffected (Hajnal, Baudouin, Oatridge, Young, & Bydder, 1992). This is not feasible in a clinical MRI setting, since data cannot be collected during irradiation and the RF coils are designed for pulsed irradiation (Pike, 1996). Instead, pulsed saturation techniques with pulses of a couple of milliseconds are employed (Graham & Henkelman, 1997). Due to the limited B_1 amplitude and safety restrictions regarding SAR, the macromolecular water can only be partially saturated and some degree of direct saturation of the free water is likely to occur. The most common pulse sequence for imaging and mapping MT is the spoiled GRE, in either 2D or 3D (York et al., 2021).

The magnetization transfer ratio

The most common, and simplest, metric to map MT is the semi-quantitative magnetization transfer ratio (MTR) (Dousset et al., 1992; York et al., 2021). In MTR, the relative difference (in percent) between an MT-weighted image, S_{MT}, and a reference image, S_{ref}, with identical sequence parameters but no MT pulse is calculated as:

$$MTR = 100\left(\frac{S_{\mathrm{ref}} - S_{\mathrm{MT}}}{S_{\mathrm{ref}}}\right). \tag{2.14}$$

Such an experiment will, however, be biased by both T_1 and B_1^+ inhomogeneities and has exhibited rather poor inter-site comparability (York et al., 2021).

Quantitative magnetization transfer

MT can be described by a two-pool model, where pool f represents the liquid/free spins and pool b represents the macromolecular/bound spins. This model is referred to as the binary spin bath (BSB) model. The BSB model is described by the longitudinal relaxation rates $R_{1\mathrm{f}} = 1/T_{1\mathrm{f}}$ and $R_{1\mathrm{b}} = 1/T_{1\mathrm{b}}$, (rates are used here to follow the convention in MT literature), the longitudinal magnetizations at thermal equilibrium $M_{0\mathrm{f}}$ and $M_{0\mathrm{b}}$, as well as the rate of transfer in either direction, k_{bf} and k_{fb}. From these parameters the bound pool fraction is obtained as:

$$F_{\mathrm{b}} = M_{0\mathrm{b}}/(M_{0\mathrm{f}} + M_{0\mathrm{b}}) \equiv k_{\mathrm{fb}}/(k_{\mathrm{fb}} + k_{\mathrm{bf}}). \tag{2.15}$$

The Bloch-McConnell equations modify the standard Bloch equations to include two coupled pools of spins (McConnell, 1958). To describe MT, the Bloch-McConnell equations are expressed as (Graham & Henkelman, 1997):

$$\frac{dM_{\mathrm{xf}}}{dt} = -2\pi\Delta M_{\mathrm{yf}} - \frac{M_{\mathrm{xf}}}{T_{2\mathrm{f}}}, \tag{2.16a}$$

$$\frac{dM_{\mathrm{yf}}}{dt} = 2\pi\Delta M_{\mathrm{xf}} - \omega_1(t)M_{zf} - \frac{M_{\mathrm{yf}}}{T_{2\mathrm{f}}}, \tag{2.16b}$$

$$\frac{dM_{\mathrm{zf}}}{dt} = \omega_1(t)M_{\mathrm{yf}} + R_{1\mathrm{f}}(M_{0\mathrm{f}} - M_{\mathrm{zf}}) - k_{\mathrm{fb}}M_{\mathrm{zf}} + k_{\mathrm{bf}}M_{\mathrm{zb}}, \tag{2.16c}$$

$$\frac{dM_{\mathrm{zb}}}{dt} = R_{1\mathrm{b}}(M_{0\mathrm{b}} - M_{\mathrm{zb}}) - (\pi g_{\mathrm{b}}(\Delta, T_{2\mathrm{b}})\omega_1^2(t) + k_{\mathrm{bf}})M_{\mathrm{zb}} + k_{\mathrm{fb}}M_{0\mathrm{b}}M_{\mathrm{zf}}. \quad (2.16\mathrm{d})$$

Here, $M_{0\mathrm{f}}$ can be normalized to 1 in the Henkelman model (Henkelman et al., 1993), $g_{\mathrm{b}}(\Delta, T_{2\mathrm{b}})$ is the bound pool absorption lineshape and $\Delta = (\omega - \omega_0)/2\pi$ is the MT pulse offset frequency in Hz. For an MT pulse of duration of t_{sat}, the differential absorption law in Eq. (2.16d) can also be expressed using the average saturation rate of M_{zb}:

$$W_{\mathrm{b}} = \pi g_{\mathrm{b}}(\Delta, T_{2\mathrm{b}}) \frac{1}{t_{\mathrm{sat}}} \int_0^{t_{\mathrm{sat}}} \omega_1^2(t) dt, \quad (2.17)$$

where the integral is referred to as the "power integral".

Similarly as for a spoiled GRE sequence, a pulsed MT experiment can be separated into periods of free cross-relaxation between the two pools (no RF irradiation) interspersed with instantaneous events of saturation (Pike, 1996). The instantaneous saturation of the bound pool can then be described by a unitless factor:

$$\delta_b = \frac{M_{\mathrm{b}}(0) - M_b(t_{\mathrm{sat}})}{M_{\mathrm{b}}(0)} \propto F_{\mathrm{b}} W_{\mathrm{b}}. \quad (2.18)$$

In fully quantitative MT (qMT), the MR parameters k_{bf}, F_{b}, $R_{1\mathrm{f}}$, $T_{2\mathrm{f}}$ and $T_{2\mathrm{b}}$ can all be solved for numerically by performing a set of MT-weighted measurements with varying $\int_0^{t_{\mathrm{sat}}} \omega_1^2(t) dt$ (typically through the flip angle) and Δ (Sled & Pike, 2001). The bound pool relaxation rate, $R_{1\mathrm{b}}$, is often set arbitrarily to 1 s^{-1} since it has a limited effect on the other parameters (Henkelman et al., 1993). In vivo, $R_{1\mathrm{b}} = 1\ s^{-1}$ could be an underestimation by a more than a factor of 5, however, which could lead to a systematic underestimation of F_{b} (Helms & Hagberg, 2009). Modelling is preferentially performed after reaching a steady state between the two pools has been reached (Helms & Hagberg, 2004). Since qMT requires a fair number of separate scans (~10-20), it is rather time consuming and thus mostly performed in a single slice. It is, however, highly reproducible and more specific to macromolecular content than MTR (York et al., 2021). The long acquisition time of full qMT and the poor reproducibility/specificity of MTR motivates the use of the semi-quantitative magnetization transfer saturation (MT_{sat}) metric (Helms, Dathe, Kallenberg, & Dechent, 2008), covered in detail in Chapter 3.

Ultra-high field strengths

The move to UHF strengths is often motivated by the increase in magnetization and consequently, the MR signal. This implies an increase in SNR and contrast to noise ratio (CNR). The induced signal in a receiver coil will increase by the square of B_0 while the dominant subject-related noise increases linearly. Theoretically, the increase in SNR with B_0 should thus be linear. However, the actual increase in SNR also depends on the pulse sequence, the properties of the imaged objects (such as relaxation times) as well as the decreased transmit (B_1^+) and receive sensitivity (B_1^-) homogeneity (the B_1 inhomogeneity at UHF is elaborated on in Chapter 4). The SNR is difficult to quantify in absolute terms because, at UHF strengths, the receive sensitivity cannot feasibly be derived from the transmit field through the principle of reciprocity (Hoult, 2000) (described below). Thus, the SNR increase at UHF has often been reported as a relative increase compared to lower fields. In a comparison between 4T and 7T, where full relaxation was allowed, the average SNR in a slice increased linearly (Ugurbil et al., 2003). The increase was spatially varying, however, with the periphery (low B_1^+) experiencing a smaller increase. A review article suggested an increase by $\sqrt{B_0}$ as a lower limit due to T_1 saturation effects and increased T_2^* decay (Duyn, 2012). A third study using spoiled GREs at 3T, 7T, and 9.4T reported an overall increase in the intrinsic SNR (corrected for relaxation and transmit field effects) across the cerebrum by $\sim B_0^{1.65}$ (Pohmann et al., 2016).

The CNR is, of course, dependent on the main contrast mechanism. In the case of T_1, the increase with B_0 has been determined as a power law up to 100 MHz (~2.3 T) (Bottomley, Foster, Argersinger, & Pfeifer, 1984):

$$T_1 = aB_0{}^b, \tag{2.19}$$

where a and b are tissue-specific constants to be empirically determined. For $B_0 =$ 0.2/1.0/1.5/4.0/7.0 T, these parameters were determined as $a = 583/867$ ms and $b = 0.382/0.376$ for WM and GM in the putamen respectively (Rooney et al., 2007). The T_1 in CSF was constant at 4.3±0.2 s. The exponential behaviour of T_1 indicates a decrease in the relative T_1 difference across tissues and thus implies a convergence and subsequent decrease in CNR. However, a study in rat brain using spoiled GREs showed an increase in CNR per unit time between WM and cortical GM even at 16.4 T (Pohmann, Shajan, & Balla, 2011). The observed CNR increase thus occurred despite the decrease in relative T_1 difference, and the authors expected improved image quality in T_1-weighted images up to 20 T.

On average, T_2^* in the cerebrum drops by approximately 50% when going from 3T to 7T (Pohmann et al., 2016). This influences obtainable signal but can be beneficial in multi-echo spoiled GRE measurements (Peters et al., 2007). The decrease is exponential as:

$$T_2^* = ae^{-bB_0}, \tag{2.20}$$

where the tissue specific parameters have been empirically determined to be $a =$ 64/90 ms and $b = 0.132/0.142$ T^{-1} for WM and GM respectively (Pohmann, Speck, & Scheffler, 2016). A plot of the B_0 dependences of T_1 and T_2^* is shown in Figure 2.1.

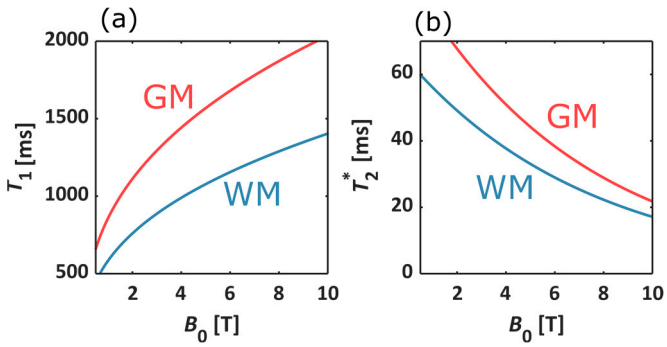

Figure 2.1. Increase in T_1 (a) and decrease in T_2* (b) as a function of B_0. The T_1 was plotted using Eq. (2.19) and the fitted parameters as obtained by Rooney et al. (2007) while T_2^* was plotted using Eq. (2.20) and the fited parameters as obtained by Pohmann, Speck, & Scheffler (2016).

In steady state imaging, longitudinal relaxation and MT are two competing processes constituting alternative pathways for the spin system to restore equilibrium magnetization (Henkelman et al., 2001). A longer T_1 thus means more MT-weighting in conventional imaging although the absolute MT does not necessarily increase. As both MT and SAR are governed by the square of the time-varying RF field, obtainable MT at UHF is curtailed by safety limits regarding tissue heating. SAR is governed by the induced electrical current of the applied field as well as local tissue conductivity and density, thus local "hot spots" of SAR deposition can arise that are difficult to predict.

The inhomogeneity of the B_0 field increases at UHF due to susceptibility effects and is most severe close to the nasal sinuses between diamagnetic tissue and paramagnetic air (Juchem & de Graaf, 2017). The choice of RF pulse shape is thus important to ensure a homogenous non-selective excitation and this issue was considered in an experiment pertaining to Paper II and is elaborated on in Chapter 3.

A benefit of the decreased homogeneity of the receive sensitivity is an increased performance of parallel imaging techniques (Wiesinger et al., 2004). The geometry (g) factor is a spatially dependent measure denoting the noise enhancement for a certain receive coil array (Pruessmann et al., 1999). Past a certain reduction factor, the g-factor will be lower at UHF compared to lower field strengths. This is because the sensitivity profiles of individual receive elements overlap less and noise correlation is reduced.

The separation of metabolic peaks increases at UHF which can be beneficial in MR spectroscopy as well as in CEST imaging. An interesting consequence of this is the increasing shift of the macromolecular absorption lineshape relative the free water resonance (Hua et al., 2007). This was exploited for Paper IV and will be elaborated on in Chapter 3.

Phase differences due to susceptibility effects increase at UHF which is beneficial in QSM (Acosta-Cabronero et al., 2018). The increased susceptibility effects are also beneficial for the blood oxygenation level dependent (BOLD) contrast used in functional MRI (Yacoub et al., 2001).

Table 2.1 shows a summary of parameters and whether they increase/decrease at increasing B_0.

Table 2.1. Paramater dependence on increasing B_0.

Parameter	Increase/Decrease (+/-)
SNR	+
CNR	+
SAR	+
T_1	+
T_2	–*
T_2^*	–
MT	+
B_0 homogeneity	–
B_1 homogeneity	–
Susceptibility effects	+
Chemical shift	+
g factor	–

* The actual T_2 relaxation is theoretically independent of B_0 but there is an apparent decrease due to increasing microscopic susceptibility gradients caused by diffusion.

Hardware and signal combination

A hardware specific peculiarity of UHF is the lack of an integral RF transmit body coil within the bore. Instead, a dedicated transmit head coil is used for transmission. To improve SNR and/or allow for parallel imaging, reception should be performed using a phased array consisting of multiple receive elements (Larkman & Nunes, 2007; Roemer, Edelstein, Hayes, Souza, & Mueller, 1990). Each receive element is connected to its own channel (receiver pathway) and preamplifier to minimize noise correlation. The signals measured by each element will have a local sensitivity field distribution as well as a spatially dependent phase. This receiver phase needs to be corrected to avoid signal cancellation and to preserve phase changes during *TE* due to susceptibilities in the imaged object (Robinson et al., 2017). To this end, complex

sensitivity maps of each element needs to be obtained from a separate reference scan. These sensitivity maps should be free of anatomical information and, on a clinical system, the anatomical information is thus removed through division by an image acquired with the homogeneous body coil (when used for reception). On the UHF system used here, the sensitivity maps are instead divided by the sum of squares of the phased array signals. For a phased array with N elements, a combined, SNR-optimized, and phase-corrected signal is obtained as:

$$S_{\mathrm{opt}} = \sum_{\mathrm{i}=1}^{N} w_{\mathrm{i}} \frac{S_{\mathrm{i}}}{C_{\mathrm{i}}}, \tag{2.21}$$

where S_{i} is the measured signal of element i, C_{i} is the respective sensitivity and $w_i = C_{\mathrm{i}}^{*} C_{\mathrm{i}} / \sum_{j=1}^{N} C_{\mathrm{j}}^{*} C_{\mathrm{j}}$ is the weighting (index j also denotes individual coil elements and the asterisk denotes the complex conjugate). The process is analogous to a SENSE reconstruction with a reduction factor of 1 (Pruessmann et al., 1999). The experimental parts of this thesis were all conducted on an actively shielded 7T Achieva scanner, (Philips Healthcare, Best, NL), using a head coil with two transmit channels at fixed phase settings (Nova Medical, Wilmington, MA) and a 32-channel phased array for reception.

Principle of reciprocity

According to the principle of reciprocity, the receive sensitivity and transmit field of a coil are identical in the non-radiative near field region, i.e. when the phase of the RF irradiation is constant across the imaged object (Hoult & Richards, 1976; Ilott & Jerschow, 2018). Theoretically, this allows for direct sensitivity mapping of individual receive coil elements by flip angle mapping if the receive coil elements were used for transmission. Thus, the receive field bias (f_{R}) is determined from the transmit field bias (f_{T}). Strictly speaking, it is the complex conjugate of the negatively rotating field (i.e. $B_1^{-*} \approx B_1^{+}$) that determines receive sensitivity, and not B_1^{-} as is more commonly referred to. The seemingly simple principle quickly becomes complicated as spatially dependent phase changes need to be accounted for, i.e. in the intermediate region of 3T and above, and in a sample with varying conductivity (Hoult, 2000). Often, errors arise as complex numbers are used to denote both the direction of rotation of B_1^{+} and B_1^{-} in the laboratory frame, as well as spatially dependent phase changes across the sample in the rotating frame (Ilott & Jerschow, 2018). Although theoretically sound, the principle of reciprocity becomes unfeasible to apply in a practical imaging experiment at UHF. Since normalized sensitivity mapping is also not an option (no homogenous body coil), f_{R} must be modeled through numerical approaches such as the unified segmentation approach (Ashburner & Friston, 2005).

3 – Multi-parameter mapping (MPM) using spoiled gradient echoes

Multi-parameter mapping (MPM) refers to the process of simultaneously deriving maps of more than one MR contrast parameter. The versatile 3D spoiled GRE sequence lends itself well to this purpose (Weiskopf et al., 2013). Simple changes in the pulse sequence result in image contrast being dominated by a different tissue-specific MR parameter. For instance, increasing the flip angle leads to a more T_1-weighted, as opposed to PD-weighted, image (the concept behind VFA-based T_1-mapping). MT-weighting can be induced by a high-energy, off-resonance RF pulse, applied prior to each *TR* cycle. The T_2*-weighting is governed by *TE*, which can be varied in a single sequence through a multi-echo readout and, provided that phase data are available, also facilitates QSM. Thus, from only three multi-echo spoiled GRE sequences, maps of T_1, PD, MT_{sat}, T_2* and magnetic susceptibility, χ, can be derived. In this chapter, special attention will be given to the mapping of T_1 and MT_{sat} using a spoiled GRE-based MPM protocol.

This chapter will explain:

1. How to derive simple expressions for T_1 and MT_{sat} through a rational approximation and inversion of the Ernst signal equation.
2. Aspects of reducing bias in derived T_1 and MT_{sat} estimates
3. How to increase the obtainable MT_{sat} under the SAR constraints present at 7T

Rational approximation of the Ernst equation

For sufficiently small flip angles and short TR, the Ernst equation can be approximated as a rational function of $f_T\alpha$ and TR (Dathe & Helms, 2010). To derive this, the linear approximation $\exp(-TR/T_1) \approx 1 - TR/T_1$ (i.e. a first-order Taylor polynomial) valid for $TR/T_1 \ll 1$ must be introduced. The Ernst equation (Eq. 2.11) then becomes:

$$S(f_{\mathrm{T}}\alpha) \approx A \sin(f_{\mathrm{T}}\alpha) \frac{TR/T_1}{1 - \cos(f_{\mathrm{T}}\alpha)(1 - TR/T_1)}. \tag{3.1}$$

After removing the exponential terms, the trigonometric terms are dealt with through the tangent half-angle substitution:

$$t = \tan(f_{\mathrm{T}}\alpha/2). \tag{3.2}$$

This allows to substitute the trigonometric functions in Eq. (3.1) using the double-angle formulas and then some other trigonometric identities as: $\sin(f_{\mathrm{T}}\alpha) = 2\sin(f_{\mathrm{T}}\alpha/2)\cos(f_{\mathrm{T}}\alpha/2) = 2\tan(f_{\mathrm{T}}\alpha/2)\cos^2(f_{\mathrm{T}}\alpha/2) = 2\tan(f_{\mathrm{T}}\alpha/2)/\sec^2(f_{\mathrm{T}}\alpha/2) = 2\tan(f_{\mathrm{T}}\alpha/2)/(1 + \tan^2(f_{\mathrm{T}}\alpha/2)) = 2t/(1 + t^2)$ and $\cos(f_{\mathrm{T}}\alpha) = 2\cos^2(f_{\mathrm{T}}\alpha/2) - 1 = 2/\sec^2(f_{\mathrm{T}}\alpha/2) - 1 = 2/(1 + \tan^2(f_{\mathrm{T}}\alpha/2)) - 1 = (1 - \tan^2(f_{\mathrm{T}}\alpha/2))/(1 + \tan^2(f_{\mathrm{T}}\alpha/2)) = (1 - t^2)/(1 + t^2)$. The Ernst equation now becomes a rational function of t:

$$S(t) \approx A \frac{2t\, TR/T_1}{[1 + t^2][1 - (1 - t^2/1 + t^2)(1 - TR/T_1)]}, \tag{3.3}$$

where simplification of the denominator yields:

$$S(t) \approx A \frac{2t\, TR/T_1}{2t^2 + (1 - t^2)\, TR/T_1}. \tag{3.4}$$

Applying a linear approximation also to Eq. (3.2), this time with regard to the flip angle, yields $t \approx f_{\mathrm{T}}\, \alpha/2$, valid for $f_{\mathrm{T}}\, \alpha/2 \ll 1$. The Ernst equation is now regained as a function of $f_{\mathrm{T}}\alpha$:

$$S(f_{\mathrm{T}}\alpha) \approx A f_{\mathrm{T}}\alpha \frac{TR/T_1}{(f_{\mathrm{T}}\alpha)^2/2 + (1 - (f_{\mathrm{T}}\alpha)^2/4)\, TR/T_1}. \tag{3.5}$$

Note that if the linear approximation for small flip angles were to be performed without the tangent half-angle substitution, i.e. $\sin(f_{\mathrm{T}}\alpha) \approx f_{\mathrm{T}}\alpha$ and $\cos(f_{\mathrm{T}}\alpha) \approx 1$, then $f_{\mathrm{T}}\alpha$ would cancel out from the equation which would make for a poor approximation. The final approximation is $TR/T_1 \cdot (f_{\mathrm{T}}\alpha)^2/4 \approx 0$. This yields the final rational approximation of the Ernst equation for small flip angles and short TR as:

$$S(f_{\mathrm{T}}\alpha) \approx A f_{\mathrm{T}}\alpha \frac{TR/T_1}{(f_{\mathrm{T}}\alpha)^2/2 + TR/T_1}. \tag{3.6}$$

Interestingly, since this last approximation can only lead to an overestimation of $S(f_{\mathrm{T}}\alpha)$, Eq (3.6) is closer to the exact solution than Eq. (3.5). From here, the Ernst angle is solved for as:

$$\alpha_E \approx \frac{\sqrt{2\,TR/T_1}}{f_{\mathrm{T}}}. \tag{3.7}$$

Figure 3.1 shows the spoiled GRE steady state signal as a function of $f_{\mathrm{T}}\alpha$ for the sequence parameters used in the experiments pertaining to Paper II ($\alpha = 16°$, $TR =$ 18 ms) and 7T specific conditions, i.e. $0 \leq f_{\mathrm{T}} \leq 2.0$ and $T_1 = 1300$, 1900 and 4300 ms. It also shows the slight deviation of the rational approximation compared to the exact equation at moderately high local flip angles and/or short T_1.

Eq. (3.6) has a pedagogical value in that the influence of $f_{\mathrm{T}}\alpha$ on $S(f_{\mathrm{T}}\alpha)$ and thus the contrast of the resulting image becomes very clear. At very small $f_{\mathrm{T}}\alpha$, the right-hand quotient approaches unity and $S(f_{\mathrm{T}}\alpha)$ is dominated by A, resulting in a PD-weighted image. Vice versa, if $f_{\mathrm{T}}\alpha$ is large, $S(f_{\mathrm{T}}\alpha)$ is dominated by the ratio containing T_1, resulting in a T_1-weighted image. As f_{T} varies across the brain, so does the local contrast. Nevertheless, a small α results in a predominant PD-weighting while a large α results in predominant T_1-weighting. Thus, the lower nominal flip angles in a DFA experiment is referred to as α_{PD} and the higher α_{T1}. The resulting signals are referred to as S_{T1} and S_{PD}.

Rearranging Eq. (3.6) to form a linear equation ($y = mx + b$) yields:

$$\frac{S}{f_{\mathrm{T}}\alpha} \approx -\frac{T_1}{2TR} S f_{\mathrm{T}}\alpha + A. \tag{3.8}$$

Solving for T_1 and the signal amplitude through linear regression yields $T_1 \approx -2mTR$ and $A \approx b$. In a DFA experiment, using S_{T1}, S_{PD} and the elementary slope equations for slope and intercept, the rational equations for T_1 and A become:

$$T_1 = \frac{2TR}{f_{\mathrm{T}}^2} \cdot \frac{S_{\mathrm{PD}}/\alpha_{\mathrm{PD}} - S_{\mathrm{T1}}/\alpha_{\mathrm{T1}}}{S_{\mathrm{T1}}\alpha_{\mathrm{T1}} - S_{\mathrm{PD}}\alpha_{\mathrm{PD}}}, \tag{3.9}$$

$$A = \frac{S_{\mathrm{PD}} S_{\mathrm{T1}}}{f_{\mathrm{T}}} \cdot \frac{\alpha_{\mathrm{T1}}/\alpha_{\mathrm{PD}} - \alpha_{\mathrm{PD}}/\alpha_{\mathrm{T1}}}{S_{\mathrm{T1}}\alpha_{\mathrm{T1}} - S_{\mathrm{PD}}\alpha_{\mathrm{PD}}}. \tag{3.10}$$

Equations (3.9) and (3.10) expose the respective quadratic and linear f_{T} bias imposed on the T_1 and A calculations when using nominal flip angles. In other words, it is instead the apparent counterparts of T_1 and A ($T_{1,\mathrm{app}}$ and A_{app}) that will be obtained when using nominal flip angles. Their relationships to the true estimates are written as

$$T_1 = T_{1,\mathrm{app}}/f_{\mathrm{T}}^2, \tag{3.11}$$

$$A = A_{\mathrm{app}}/f_{\mathrm{T}}. \tag{3.12}$$

The appearance of these biases is not evident when using the traditional VFA linearization in Eq. (2.13).

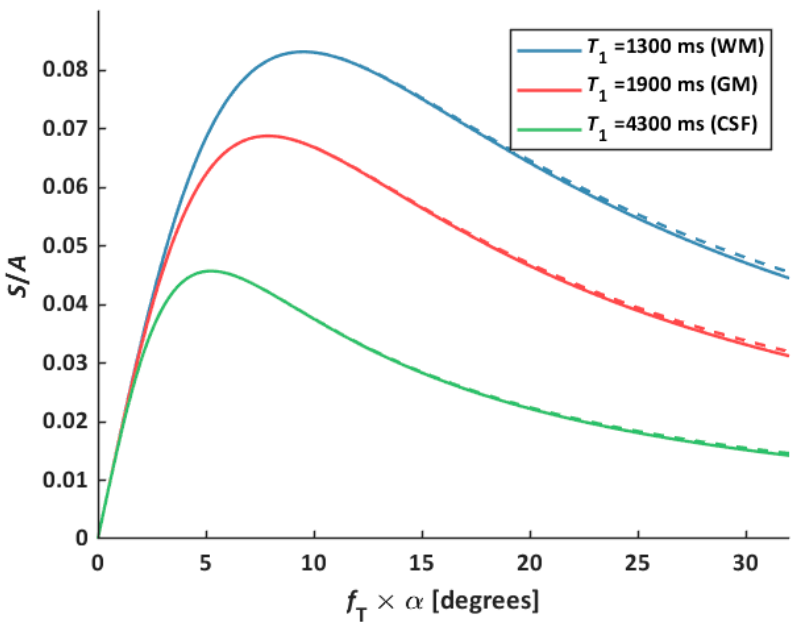

Figure 3.1. The spoiled GRE steady state signal as a function of the local flip angle for *TR* = 18 ms and three typical values of T_1 representing WM, GM and CSF. The flip angle for which the signal maximum is reached at each T_1 is referred to as the Ernst angle, α_E. Dotted lines represent the rational approximation which result in a slight overestimation at high local flip angles and short T_1.

Magnetization transfer saturation (MT_{sat})

Magnetization transfer saturation (MT_{sat}) is a semiquantitative metric denoting the fraction of M_{zf} saturated by a single MT pulse during TR as introduced by Helms & Piringer (2005). MT_{sat} is inherently corrected for T_1 and (in the absence of direct saturation) directly proportional to δ_b (Eq. (2.18)) and consequently to F_b (Eq. (2.15)). It is derived by adding an MT-weighted spoiled GRE to the previously described DFA experiment. By virtue of being independent of the already estimated $R_1 = 1/T_1$, it is more directly representative of F_b than the MTR (as before, rates are used as is the convention in MT literature). Expanding on the rational approximation of the Ernst equation (Eq. (3.6)), an MT saturation event, δ_{MT}, separate from the saturation due to the readout excitation, $(f_T\alpha)^2/2$, can be added in the denominator to describe the steady state signal in an MT-weighted spoiled GRE sequence (Helms, Dathe, Kallenberg, et al., 2008):

$$S_{MT} \approx A f_T \alpha \frac{R_1 TR}{(f_T\alpha)^2/2 + \delta_{MT} + R_1 TR}. \tag{3.13}$$

Solving for δ_{MT} yields:

$$\delta_{MT} = (A f_T \alpha / S_{MT} - 1) R_1 TR + (f_T\alpha)^2/2. \tag{3.14}$$

Note that since R_1 and A are determined from the DFA experiment, any biases will carry over when calculating δ_{MT}. Eq. (3.14) serves as the definition of δ_{MT} and the "approximately equal to" sign is thus dropped. Since δ_{MT} is directly related to δ_b, it is approximately proportional to the power integral and thus f_T^2 (equations (2.17) and (2.18)).

By substituting R_1 and A with their apparent counterparts, obtained when using nominal flip angles (equations (3.11) and (3.12)), f_T cancels out from Eq. (3.14):

$$\delta_{MT,app} = \left(A_{app}\alpha / S_{MT} - 1\right) R_{1,app} TR + \alpha^2/2. \tag{3.15}$$

Thus, $\delta_{MT,app}$ is corrected for the primary influence of f_T^2. Albeit the somewhat confusing terminology, this implies that $\delta_{MT,app}$, not δ_{MT}, is inherently corrected for B_1^+ inhomogeneities. There is still a residual transmit field related bias, however, and it will be shown later that correction through external flip angle mapping is still necessary, at least at UHF strengths.

In a recent review study of MT in relapsing-remitting MS it was suggested to use MT_{sat} instead of MTR to increase comparability between different studies and

research sites (York et al., 2021). Also recently, it has been used to determine the inner to outer myelinated axon diameter (g-ratio), which in turn was used to study disease progression in MS through brain network topologies (Kamagata et al., 2019). Further, MT_{sat} is not sensitive to iron and has thus been used for improved automated segmentation of deep brain structures compared to conventional T_1-weighted images (Helms, Draganski, Frackowiak, Ashburner, & Weiskopf, 2009).

Spoiling

The Ernst equation assumes perfect spoiling of transverse magnetization before each new excitation. If this condition is not fulfilled, alternative echo pathways will form, and full Bloch equation simulations become necessary to model the signal. It follows that the subsequent DFA-based T_1-mapping will be biased (Preibisch & Deichmann, 2009). A very straightforward way to achieve complete spoiling would be to set $TR \geq 5 \times T_2$ so that all transverse magnetization has decayed before the next TR period. This is, however, not a feasible solution because of the long acquisition times this would entail. Another way is to apply a spoiler gradient at the end of the TR period. Spoiling gradients are by themselves unsuitable since gradients are spatially varying and thus the effectiveness of the spoiling will also show a spatial dependence. The third option is to use RF spoiling where the phase of the excitation pulse is varied according to a phase-cycling scheme (Crawley, Wood, & Henkelman, 1988; Zur, Wood, & Neuringer, 1991):

$$\phi_j = \phi_{j-1} + j\phi_0, \qquad j = 1,2,3,\ldots \tag{3.16}$$

where ϕ_j denotes the phase of the jth pulse and the starting value, ϕ_0, is referred to as the *phase difference increment*. Eq. (3.16) can be solved for to reveal a quadratic dependence of index j:

$$\phi_j = \frac{1}{2}\phi_0(j^2 + j + 2), \qquad j = 1,2,3,\ldots \tag{3.17}$$

The net transverse magnetization vector, $\vec{\boldsymbol{M}}_j$, produced by the jth pulse will thus have a different phase than the net magnetization, $\vec{\boldsymbol{M}}_{j-1}$, remaining from the previous pulse. The resulting transverse magnetization, $\vec{\boldsymbol{M}}_{\mathrm{xy}}$, that is measured will be a superposition of all residual magnetizations that have not yet completely decayed and is thus generally somewhat smaller than what would be expected from the Ernst equation.

The phase cycling scheme complicates the Bloch equations as $\mathbf{B}_1$ is applied solely in the x-direction only for $\phi_j = 0$. For numerical simulations, the rotation matrix must thus be modified to account for ϕ_j (Yarnykh, 2010):

$$\mathbf{R}(\alpha, \phi_j) = \begin{bmatrix} \cos\alpha + (1-\cos\alpha)\cos^2\phi_j & (1-\cos\alpha)\sin\phi_j\cos\phi_j & -\sin\alpha\sin\phi_j \\ (1-\cos\alpha)\sin\phi_j\cos\phi_j & \cos\alpha + (1-\cos\alpha)\sin^2\phi_j & \sin\alpha\cos\phi_j \\ \sin\alpha\sin\phi_j & -\sin\alpha\cos\phi_j & \cos\alpha \end{bmatrix}, \quad (3.18)$$

which is equal to Eq. (2.7) for $\phi_j = 0$.

The length of the phase cycle, N_ϕ, refers to the number of TR periods until an RF pulse with $\phi_j = \phi_0$ is produced again. For instance, $\phi_0 = 120°$ yields a phase cycle of $N_\phi = 3$ and would thus be a poor choice as ϕ_0 should pertain to yielding $N_\phi \gg T_2/TR$. The poorness of $\phi_0 = 120°$ in particular is interesting since phase difference increments that yields very long phase cycles, such as $\phi_0 = 117°$ (Zur et al., 1991) or $\phi_0 = 123°$ (both yielding $N_\phi = 16$) become somewhat sensitive to instabilities in the assigned phase. Some typical values of ϕ_0 include 117° ($N_\phi = 16$, GE), 50° ($N_\phi = 9$, Siemens) and 150° ($N_\phi = 9$, Philips).

Typically, spoiling gradients and RF phase cycling are combined to increase spoiling efficiency. In the spoiled GRE experiments used for this thesis, the phase difference increment was $\phi_0 = 150°$ and spoiling gradients were applied in the readout and slice directions with areas of ~13 mT·ms/m each.

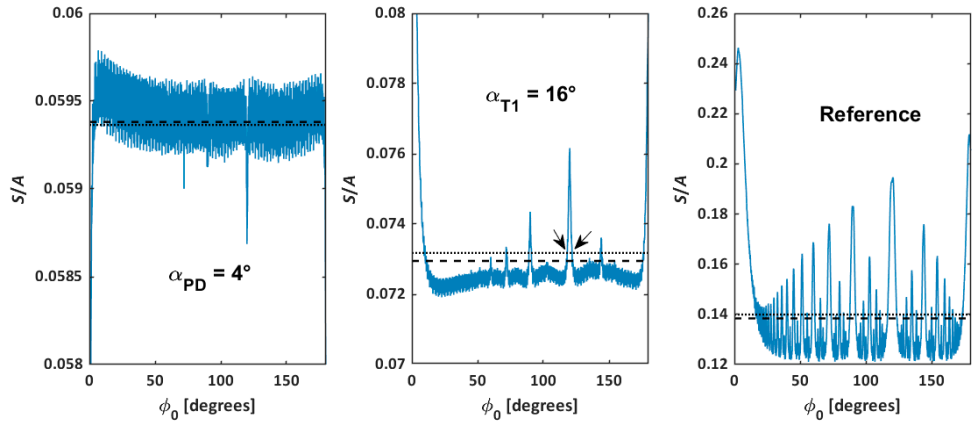

Figure 3.2. Steady state signal derived from the Bloch simulations (solid) or the Ernst equation (dashed=exact, dotted=rational approximation) as a function of ϕ_0 for α_{PD} = 4° and α_{T1} = 16°. The signal is generally well-represented by the Ernst equation for α_{PD} = 4° but at α_{T1} = 16° the signal is systematically ~1% lower than predicted. Some values of ϕ_0, like 118.2° and 121.9°, result in perfect agreement but are situated on steep slopes (arrows) close to 120° and therefore sensitive to instabilities. A phase difference increment situated on a plateu such as ϕ_0 = 150° is more stable although it will lead to a consistent bias if not corrected for. Simulation details: Number of isochromats = 360, T_1 = 1300 ms, T_2 = 50 ms, TR = 18 ms, f_T = 1. The "Reference" plot was simulated with the parameters given by Preibisch & Deichmann (2009), i.e. α = 30°, T_1 = T_2 = 1000 ms, TR = 50 ms, and served as validation of the other simulations. Note the difference in vertical scales.

Most spoiling schemes will result in at least some deviation from the Ernst equation. The deviation often becomes substantial past a certain upper threshold of the local flip angle, where it will result in an increasing overestimation of the signal (Ganter, 2006). This upper threshold can be determined experimentally and is most sensitively identified visually by the linear Eq. (3.8) (Helms, Dathe, Weiskopf, & Dechent, 2011). By performing a VFA experiment and determining for which flip angle the measurement deviates from the expected linear relationship, the upper limit of α_{T1} for the expected conditions (range of f_T, T_1, T_2, TR) can be determined. Figure 3.3 shows a simulation of this deviation corresponding to the experiment performed in Paper II. Here, the measured signal is replaced by simulations of the Bloch equations. Noticeable deviations from the Ernst equation occur beyond a local flip angle of $f_T\alpha \approx 20°$.

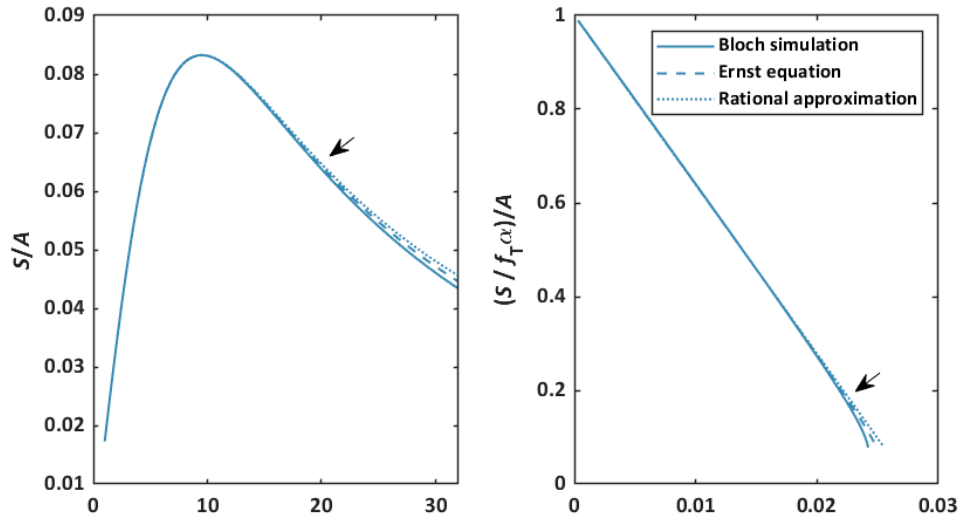

Figure 3.3. Deviations of the exact and approximated Ernst equation from the simulated steady state signal. The linear form of the Ernst equation (right-hand panel) more readily shows the deviation from the simulated signal at a local flip angle of approximately 20° (arrows). This is in accordance with the experimental results described in Paper II. Simulation details: *TR* = 18 ms, T_1 = 1300 ms, T_2 = 50 ms, ϕ_0 = 150°, 1000 spin isochromats where each spin was rotated by different increments between 0 and 2π at the end of each *TR* to simulate full gradient spoiling.

The effect of incomplete spoiling in a DFA T_1-mapping experiment can also be corrected for post hoc by protocol-specific (α_{T1}, α_{PD} and TR) correction factors derived from Bloch equation simulations (Preibisch & Deichmann, 2009). Unless separate T_2-mapping is performed, it becomes necessary to assume a fixed T_2 in the simulations. This is justified since T_2 does not vary much between WM and GM. Since T_2 is shorter at higher field strengths, the correction factors will, however, still be field strength dependent. For 7T measurements of T_2, see Oros-Peusquens et al. (2008) and Wiggermann, MacKay, Rauscher, & Helms (2021).

The relationship between the true T_1 and the biased $T_{1,sp}$ is linear (Preibisch & Deichmann, 2009):

$$T_1 = m(f_T)T_{1,sp} + b(f_T), \tag{3.19}$$

where the slope, $m(f_T)$, and intercept, $b(f_T)$, must be determined through protocol- and field strength-specific simulations. Accordingly, simulations were performed for protocol- and 7T-specific conditions over a range of T_1 values between 1100 ms and 2200 ms in increments of 100 ms, f_T values between 0.2 and 2.0 in increments of 0.1 and $T_2 = 50$ ms. The results can be seen in Figure 3.4. The parameters $m(f_T)$ and $b(f_T)$ can both be described by respective cubic polynomials that, after curve fitting, yields the following equations:

$$m = 0.0437 f_{\mathrm{T}}^3 - 0.0673 f_{\mathrm{T}}^2 + 0.0505 f_{\mathrm{T}} + 0.9905, \tag{3.20}$$

$$b = -33.1972 f_{\mathrm{T}}^3 + 59.8589 f_{\mathrm{T}}^2 - 34.2340 f_{\mathrm{T}} - 1.8759 \text{ ms}. \tag{3.21}$$

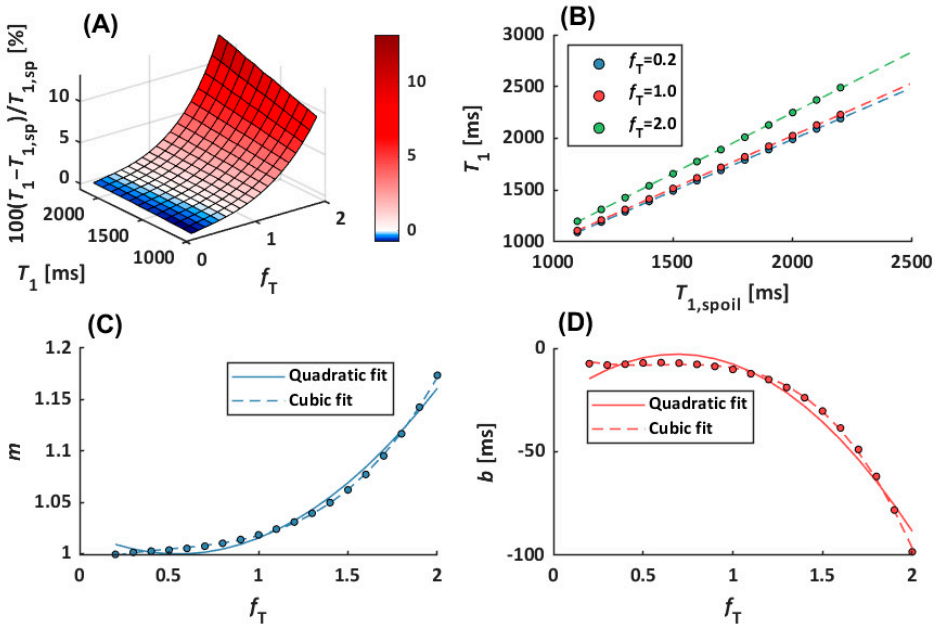

Figure 3.4. Bias in T_1 estimation due to incomplete spoiling and how to correct it for a specific 7T DFA protocol. (A) The relative difference between the true T_1 and $T_{1,sp}$ increases strongly with f_T and weakly with T_1. (B) The relationship between the true T_1 and $T_{1,sp}$ is linear where the slope, m, and intercept, b, depends on f_T. (C) The slope m is very well described by a cubic function and less so by a quadratic one. (D). The same as in (C) applies to the intercept, b.

In the original work, two quadratic polynomials for m and b were proposed (Preibisch & Deichmann, 2009). Because the simulation behind this correction also accounts for differences between the rational and exact solutions of the Ernst equation, and because of the wider range of f_{T} ($0.2 \leq f_{\mathrm{T}} \leq 2.0$ vs $0.7 \leq f_{\mathrm{T}} \leq 1.3$), two cubic polynomials resulted in much better fits, $r_2 = 0.988$ vs $r_2 = 1.000$ for m and $r_2 = 0.973$ vs $r_2 = 0.999$ for b.

To circumvent protocol-specific simulations, separately acquired flip angle maps can be modified by a factor (Baudrexel, Noth, Schure, & Deichmann, 2018):

$$C_{\phi 0} = \sum_{k,l=0}^{k+l \leq 5} P_{k,l} \cdot \alpha_{\mathrm{T1}}^k \cdot TR^l \tag{3.22}$$

where α_{T1} should be given in degrees and TR in ms. The 2D set of polynomial parameters, $P_{k,l}$, was obtained for the three most common values of ϕ_0 (50°, 117° and 150°) and provided to allow calculation of $C_{\phi 0}$. The underlying assumption is

that deviations in the T_1 estimation will stem solely from inefficient spoiling of the highest flip angle, α_{T1}, and that the bias will be largely unaffected by T_1 (supported by Figure 3.4, panel A, for $f_{\mathrm{T}} < \sim 1.5$). In practice, the procedure is done as follows: (1) Scale the flip angle map to $f_{\mathrm{T}}\alpha_{\mathrm{T1}}$. (2) Calculate a map of $C_{\phi 0}$ from Eq. (3.22). (3) Multiply $f_{\mathrm{T}}\alpha_{\mathrm{T1}}$ by $C_{\phi 0}$. (4) Divide by α_{T1} to obtain $f_{\mathrm{T,mod}}$. The modified $f_{\mathrm{T,mod}}$ is then used to correct the $T_{1,\mathrm{app}}$ map. Since the protocol-specific simulation was not available at the time, this approach was implemented for the experiments pertaining to Paper II. Note that the simulations were originally performed with 3T in mind and hence for a rather long $T_2 = 85$ ms and a somewhat lower range of T_1 (700 ms – 1800 ms). Furthermore, CSF has much longer T_1 and T_2 than brain tissue and the correction may thus not be valid in those pixels. Since α_{T1} had already been experimentally restricted (Figure 3.3), this was deemed a sufficient correction at the time. Note also that the shorter T_2 of 7T benefits spoiling (Corbin & Callaghan, 2021).

Lastly, it should be noted that spoiler gradients induce diffusion which will effectively increase spoiling efficiency (Yarnykh, 2010). In the strong spoiling regimen, with gradient areas between 280-450 mT·ms/m, spatial averaging of spin isochromats due to diffusion leads to very effective spoiling in combination with RF phase cycling. However, this strong spoiling feature will require prolonged TR (or removal of the multi-echo readout) and was therefore not implemented. Note also that the above simulations (Figure 3.4) did not account for diffusion effects.

Shape of excitation pulse

VFA-based T_1-mapping is mostly performed with 3D encoding and nonselective excitation rather than by multislice excitation. This increases SNR and reduces slice profile effects since there is no risk of crosstalk between overlapping non-rectangular slice profiles (Helms et al., 2011). However, the frequency response profile of the nonselective excitation must be sufficiently constant across the range of Larmor frequencies resulting from B_0 inhomogeneities at 7T. The deviation in Larmor frequency, $\Delta\nu_0$, is usually within ±500 Hz at 7T after second order gradient shimming. If the response profile is not sufficiently flat, areas with a high $|\Delta\nu_0|$ will experience deviating (likely smaller) local flip angles. This effect is not monitored by independent flip angle mapping unless the same RF pulse is applied in both techniques. Increasing the bandwidth of the pulse by reducing its duration, t_{RF}, is not appropriate because of subsequent increase of the power integral (Eq. (2.17)) and ensuing MT effects (covered later in this Chapter). Instead, the shape of the excitation pulse should be considered. Figure 3.5 shows four different RF pulse shapes with three different t_{RF} and their frequency responses. All the pulses yields a flip angle of 16° at $\Delta\nu_0 = 0$ Hz. Three of the shapes (block, sinc main lobe and

sinc) show a narrow frequency response profile within $-500 \leq \Delta\nu_0 \leq +500$ Hz unless the pulse duration is short ($t_{RF} = 211$ µs). Even at $t_{RF} = 211$ µs, the block-shaped pulse saturates M_z slightly less close to $\Delta\nu_0 = \pm 500$ Hz. The fourth shape, an asymmetric sinc with a single sidelobe on the negative side, yields a flat frequency response even at a moderately long $t_{RF} = 698$ µs. The peak B_1 value also needs to be considered. A sinc-shaped pulse with $t_{RF} = 211$ µs for instance, requires a peak B_1 of 21.2 µT to produce a flip angle of 16° which exceeds the limit of 20 µT deliverable by the RF coil. To summarize, four out of the 4×3 = 12 RF pulse options presented in Figure 3.5, show a sufficiently narrow frequency response. In the study reported in Paper II, incidental MT effects were minimized using the asymmetric sinc-shaped pulse with duration $t_{RF} = 698$ µs. The same pulse was then also applied for readout excitation in Papers IV and V. The other three pulses (sinc main lobe/sinc/asymmetric sinc with $t_{RF} = 211$ µs) have a higher power integral and will thus result in incidental MT effects.

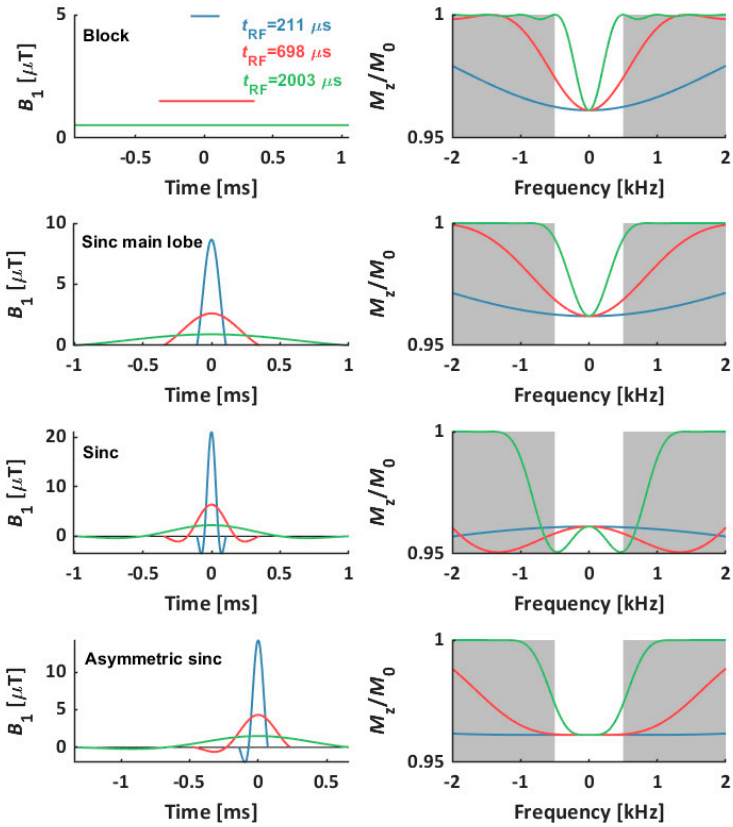

Figure 3.5. Four RF pulse shapes, each with three different durations (t_{RF}=211, 698 and 2003 µs), (left column) and their corresponding frequency responses (right column). Each RF pulse yields a flip angle of 16° at the center frequency. Unless the pulse duration is short (t_{RF}=211 µs), all shapes except the asymmetric sinc with a single side lobe (bottom row) result in uneven profiles within the expected range of Larmor frequencies, i.e. $\Delta\nu_0$ = ±500 Hz (highlighted white area). This will lead to varying local flip angles across the imaged object which cannot be corrected for by flip angle mapping. A short pulse duration entails a high power integral which is undesirable due to incidental MT effects. Simulations were performed using the PulseWizard tool available from de Graaf (2018).

MT pulse

The purpose of the MT pulse is to maximize the saturation of the bound pool (δ_{b} in Eq. (2.18)) without directly saturating the free pool (i.e. the "direct effect"), while also keeping within SAR limits. The parameters of the MT pulse that can be controlled experimentally through the user interface on the scanner are (1) the nominal flip angle, α_{sat}, (2) the duration, t_{sat}, (3) the shape of the pulse and (4) the offset frequency, Δ.

To derive a relation between α_{sat}, t_{sat} and pulse shape to the power integral in Eq. (2.17) (and thus δ_{b}), the local flip angle is first re-written as:

$$f_{\mathrm{T}}\alpha_{\mathrm{sat}} = \int_0^{t_{\mathrm{sat}}} \omega_1(t)dt = \omega_{1,\mathrm{max}} t_{\mathrm{sat}} \int_0^1 \acute{\omega}_1(\acute{t})d\acute{t} = \omega_{1,\mathrm{max}} t_{\mathrm{sat}} q_1, \quad (3.23)$$

where $\omega_{1,\mathrm{max}}$ is the maximum amplitude of the RF pulse and the unitless shape factor $q_1 = \int_0^1 \acute{\omega}_1(\acute{t})d\acute{t} \leq 1$ describes the shape of the pulse.

Secondly, performing the analogous operation on the power integral yields:

$$\int_0^{t_{\mathrm{sat}}} \omega_1^2(t)dt = \omega_{1,\mathrm{max}}^2 t_{\mathrm{sat}} \int_0^1 \acute{\omega}_1^2(\acute{t})d\acute{t} = \omega_{1,\mathrm{max}}^2 t_{\mathrm{sat}} q_2, \quad (3.24)$$

where the next shape factor $q_2 = \int_0^1 \acute{\omega}_1^2(\acute{t})d\acute{t} \leq 1$ describes the shape of the RF power integral. The substitutions $\omega_{1,\mathrm{max}} t_{\mathrm{sat}} = f_{\mathrm{T}}\alpha / q_1$ and $\omega_{1,\mathrm{max}} = f_{\mathrm{T}}\alpha_{\mathrm{sat}} / q_1 t_{\mathrm{sat}}$ in Eq. (3.24) yields:

$$\int_0^{t_{\mathrm{sat}}} \omega_1^2(t)dt = Q\,(f_{\mathrm{T}}\alpha_{\mathrm{sat}})^2 / t_{\mathrm{sat}}, \quad (3.25)$$

where Q is the final shape factor. Eq. (3.25) relates the power integral to pulse parameters that can be defined at the console. For a given pulse shape:

$$Q = \frac{q_2}{q_1^2} = \frac{\int_0^1 \acute{\omega}_1^2(\acute{t})d\acute{t}}{\left(\int_0^1 \acute{\omega}_1(\acute{t})d\acute{t}\right)^2} \geq 1, \quad (3.26)$$

describes the normalized energy. A lower Q translates to a higher normalized energy where a rectangular pulse has the lowest $Q = 1$. In other words, Q describes the

time efficiency of a certain pulse shape, with a rectangular shape being the most efficient. The upper limit of the MT pulse power will be set by SAR restrictions and can only be further increased by increasing TR. Although the pulse power is thus set, the question of how to trade-off Q, α_{sat} and t_{sat} can make for an interesting optimization problem since these parameters affect the frequency response profile of the MT pulse. If the frequency response of the MT pulse overlaps with the free water resonance, the direct saturation will bias the $\mathrm{MT_{sat}}$ estimate. An MT pulse with low Q and short t_{sat} will generally have a wider frequency response. Thus, care must be taken so that a time-efficient MT pulse still has a sufficiently narrow response so as not to induce direct saturation. This is the opposite rationale to the readout pulse of the non-selective excitation, where the frequency response should be as wide as possible.

Furthermore, the MT pulse offset frequency, Δ, is important to consider both with regard to the direct effect and induced δ_{b}. Obviously, the risk of direct saturation decreases at higher values of Δ. However, a larger Δ also entails a smaller δ_{b} through the absorption lineshape of the bound pool, $g_{\mathrm{b}}(\Delta, T_{2\mathrm{b}})$. How much smaller it will become depends on which function best describes $g_{\mathrm{b}}(\Delta, T_{2\mathrm{b}})$. In the BSB model, $g_{\mathrm{b}}(\Delta, T_{2\mathrm{b}})$ has been described by several different functions. These include (among others) Lorentzian (like the free water lineshape, ($g_{\mathrm{f}}(\Delta, T_{2\mathrm{f}})$) (Grad & Bryant, 1990), Gaussian (Henkelman et al., 1993) and super-Lorentzian (Morrison & Henkelman, 1995). In textbook literature, the lineshape is often illustrated as being Gaussian, i.e. with a rather flat top. However, in a clinical setting (i.e. for brain tissue and $\Delta < 20$ kHz) the super-Lorentzian line shape has been shown to give the best fit to experimental data (Li, Graham, & Henkelman, 1997).

The free pool Lorentzian lineshape is expressed as:

$$g_{\mathrm{f}}(\Delta, T_{2\mathrm{f}}) = \frac{T_{2\mathrm{f}}}{\pi} \cdot \frac{1}{1 + (2\pi\Delta \cdot T_{2\mathrm{f}})^2}, \tag{3.27}$$

while the super-Lorentzian bound pool lineshape (Wennerström, 1973) is given by:

$$g_{\mathrm{b}}(\Delta, T_{2\mathrm{b}}) = \sqrt{\frac{2}{\pi}} \int_0^{\pi/2} \frac{T_{2\mathrm{b}}}{|3\cos^2\theta - 1|} \exp\left(-2\left(\frac{2\pi\Delta T_{2\mathrm{b}}}{3\cos^2\theta - 1}\right)^2\right) \sin\theta \, d\theta. \tag{3.28}$$

The super-Lorentzian shape of g_{b} means that δ_{b} increases somewhat faster with decreasing Δ than one would expect for a Gaussian shape (Figure 3.6). It follows that Δ should be set as small as is allowed by the frequency response. Such a minimum Δ was experimentally identified in an experiment described in Paper IV by varying Δ and examining the estimated δ_{MT} in GM relative to WM. In the absence of a direct effect, δ_{MT} should increase solely due to $g_{\mathrm{b}}(\Delta, T_{2\mathrm{b}})$ as Δ is decreased, i.e. the ratio $\delta_{\mathrm{MT}}(\mathrm{GM})/\delta_{\mathrm{MT}}(\mathrm{WM})$ should be approximately constant and

independent of Δ as can be seen in Figure 3.6. However, in the presence of a direct effect there will be a Δ-dependent "shift" in both $\delta_{\mathrm{MT}}(\mathrm{GM})$ and $\delta_{\mathrm{MT}}(\mathrm{WM})$ which depends on $g_{\mathrm{f}}(\Delta, T_{2\mathrm{f}})$. Note that $T_{2\mathrm{f}}$ is similar in GM and WM (Wiggermann, MacKay, Rauscher, & Helms, 2021). Thus, the above ratio increases by decreasing Δ in the presence of a direct effect. In this way, the onset of the direct effect and thus the minimum Δ for a particular MT pulse can be determined. An observed $\delta_{\mathrm{MT}}(\mathrm{CSF}) > 0$ is also a sign of direct saturation since the CSF should be practically devoid of macromolecular content and consist only of a free pool. Lastly, it should be noted that the above rationale assumes identical $g_{\mathrm{b}}(\Delta, T_{2\mathrm{b}})$ and thus identical $T_{2\mathrm{b}}$ in WM and GM which is not strictly the case as $T_{2\mathrm{b}}$ in GM is very slightly shorter (~1 μs). This should have a very minor, and also opposite effect, on the Δ-dependency of $\delta_{\mathrm{MT}}(\mathrm{GM})/\delta_{\mathrm{MT}}(\mathrm{WM})$, i.e. the ratio should decrease at decreasing Δ.

Another important aspect of Δ is its sign, i.e. whether the MT pulse should be applied on the negative (lower frequency, upfield in NMR terminology) or the positive (higher frequency, downfield in NMR terminology) side of the free water resonance. In the traditional MT literature, this issue is not considered and only positive offsets have been studied at 1.5T (Henkelman et al., 1993; Morrison & Henkelman, 1995; Sled & Pike, 2000). It has been shown that $g_{\mathrm{b}}(\Delta, T_{2\mathrm{b}})$ is not centered at the water resonance but is instead shifted towards lower frequencies (Hua et al., 2007). In human WM, this shift was measured to be −2.34±0.17 ppm. This means that a rather substantial increase in δ_{b} is obtained simply by changing the sign of Δ from "+" to "–" on the console. Further, this means that, as the absolute shift in Hz is field dependent, the increase in δ_{b} obtainable in this way is quite a bit higher at 7T compared to 3T or 1.5T. At absolute shifts of −697±51 Hz, −299±22 Hz and −149±11 Hz, the relative increase in $g_{\mathrm{b}}(\Delta = \pm 2\ \mathrm{kHz}, T_{2\mathrm{b}} = 10.4\ \mu\mathrm{s})$, and thus δ_{b}, should be about 8%, 16% and 39%. Most of the classical MT literature was conducted at 1.5T, and this may explain why this shift was not recognized. As described in Paper IV, an increase of 45% of δ_{MT} in WM was indeed observed when altering the sign as $\Delta = \pm 2$ kHz. Figure 3.6 illustrates the shift of the super-Lorentzian g_{b} at 7T for two different values of $T_{2\mathrm{b}}$, representing WM and GM, as well as the Lorentzian line shape of free water. Note that there is no data on the shift in GM available, so identical shifts were assumed in the figure to facilitate comparison of $g_{\mathrm{b}}(\Delta, T_{2\mathrm{b}})$.

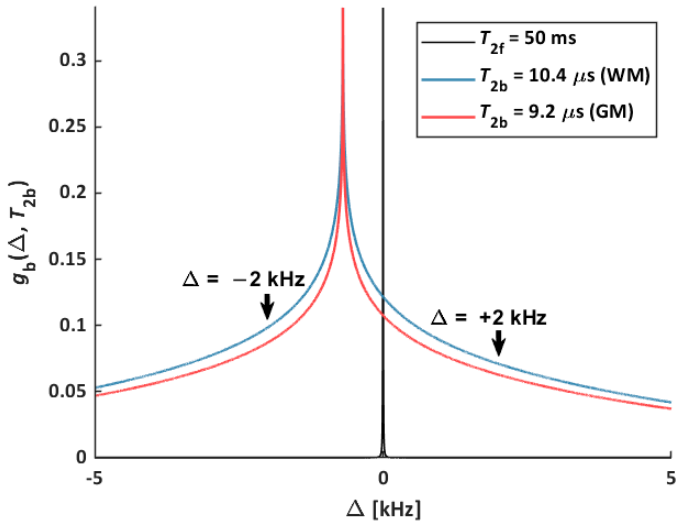

Figure 3.6. Super-Lorentzian absorption line shapes of the bound pool, $g_b(\Delta, T_{2b})$, as a function of offset frequency (Δ) for WM (blue, T_{2b}=10.4 µs) and GM (red, T_{2b}=9.2 µs). The Lorentzian free pool line shape $g_f(\Delta, T_{2f})$ at T_{2f}=50 ms is shown in black. The arrows indicate the increase in $g_b(\Delta, T_{2b})$ and thus δ_b that can be obtained when changing the sign of the applied MT pulse. The T_{2b} values were obtained from Morrison & Henkelman (1995).

Incidental MT effects caused by the excitation pulse

When an excitation pulse with duration t_{RF} is applied on-resonance to a two-pool spin system, it acts on both the free and the bound pool, resulting in partial saturation of both M_{zf} and M_{zb}. The degree to which the bound pool is saturated is determined by the power integral while the saturation of the free pool is determined by the local flip angle as $\delta_f = 1 - \cos(f_T \alpha)$, which after second order Taylor expansion (valid for small flip angles) is approximated by:

$$\delta_f \approx (f_T \alpha)^2 / 2. \tag{3.29}$$

If the proportion between M_z in the two pools is disturbed by the excitation pulse so that it no longer conform to the original pool size ratio (i.e. $M_{zb}/M_{zf} \neq M_{0b}/M_{0f}$), MT is induced in addition to T_1 relaxation. These MT effects lead to deviations from the single pool Ernst equation (Ou & Gochberg, 2008). The incidental MT observed on the free pool ($\delta_{MT,inc}$) can be described in analogy to the δ_{MT} imposed by off-resonance irradiation in Eq. (3.13). Conventional MT (as in an MT experiment) is directed from the bound to the free pool and typically occurs when using high power pulses whereas "inverse" MT (from the free to the bound pool) occurs for low power "soft" pulses. The direction of MT can be described by the sign of $\delta_{MT,inc}$ which is governed by the initial difference in partial saturation, i.e. $\delta_b - \delta_f$ (Helms, 2021).

Looking at the Ernst equation in the presence of MT (Eq. (3.13)), it can be seen that a positive $\delta_{\mathrm{MT,inc}}$ (conventional MT, $\delta_{\mathrm{b}} > \delta_{\mathrm{f}}$) will decrease the steady state signal while a negative $\delta_{\mathrm{MT,inc}}$ (inverse MT, $\delta_{\mathrm{f}} > \delta_{\mathrm{b}}$) entails an increase in the steady state signal. If the readout excitation pulse induces MT in either direction, the single pool Ernst equation is no longer valid and any subsequent estimation of T_1 (and consequently δ_{MT}) will be biased.

To express $\delta_{\mathrm{b}} - \delta_{\mathrm{f}}$ in parameters that can readily be defined on the console, the previously introduced shape factor Q (Eq. (3.26)) is used to obtain:

$$\delta_{\mathrm{b}} - \delta_f = A \int_0^{t_{\mathrm{RF}}} \omega_1^2(t)dt - (f_{\mathrm{T}}\alpha)^2/2 = \left(A\frac{Q}{t_{\mathrm{RF}}} - \frac{1}{2}\right)(f_{\mathrm{T}}\alpha)^2 \quad (3.30)$$

where A is an unknown proportionality factor. Since both δ_{b} and δ_f are functions of $(f_{\mathrm{T}}\alpha)^2$ and Q is a pulse shape-specific constant, there should exist a value of t_{RF} which result in a balance between the two pools, i.e. $\delta_{\mathrm{b}} - \delta_f = 0$ and hence $\delta_{\mathrm{MT,inc}} = 0$ for all values of $f_{\mathrm{T}}\alpha$. Since the above derivation assumes that the RF pulses producing $f_{\mathrm{T}}\alpha_{\mathrm{T1}}$ and $f_{\mathrm{T}}\alpha_{\mathrm{PD}}$ in a DFA experiment have the same t_{RF} and Q, the following is valid:

$$\delta_{\mathrm{MT,inc}}(f_{\mathrm{T}}\alpha_{\mathrm{T1}}) = (\alpha_{\mathrm{T1}}/\alpha_{\mathrm{PD}})^2 \delta_{\mathrm{MT,inc}}(f_{\mathrm{T}}\alpha_{\mathrm{PD}}). \quad (3.31)$$

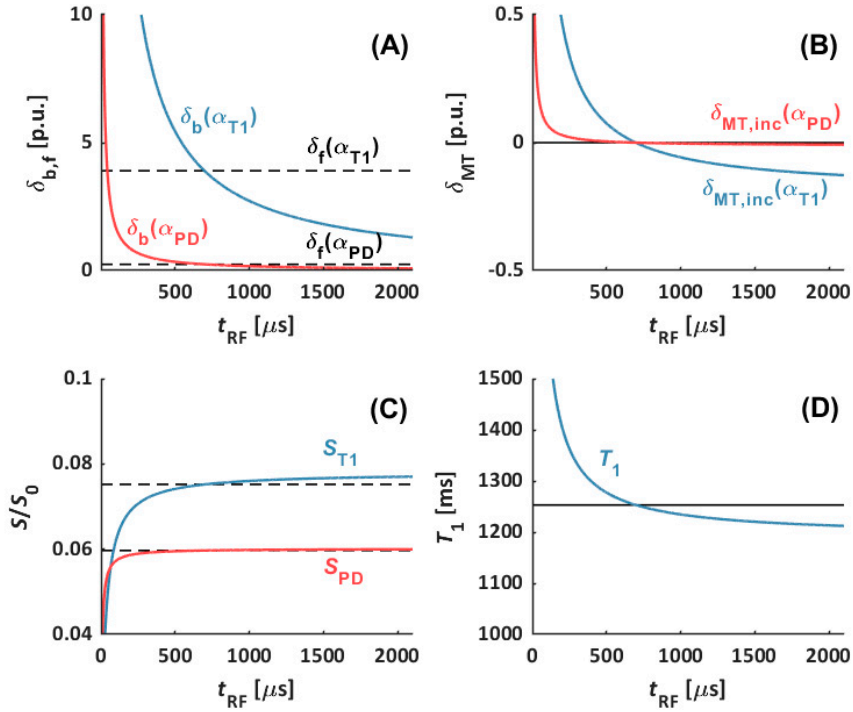

Figure 3.7 Simulation of how incidental MT can influence T_1-mapping in a DFA experiment with α_{PD}=4° and α_{T1}=16°. (A) The saturation of the free pool (dashed black line) is independent of t_{RF} but the saturation of the bound pool will decrease as the energy of the pulse decreases. This means that there should be a common "balanced" t_{RF} where $\delta_b=\delta_f$ regardless of α. (B) The incidental MT saturation becomes negative past this "balanced" value of t_{RF}=698 μs where "inverse" MT is induced. (C) The steady state signals (S_{T1} and S_{PD}) are decreased by conventional MT (short t_{RF}, high power) and increased by "inverse" MT (long t_{RF}, low power). Black dashed lines denote the steady state signals when $\delta_{MT,inc}$=0. (D) Since α_{T1} will disturb the equilibrium more than α_{PD}, the T_1 calculation is dominated by S_{T1}. When S_{T1} is decreased due to conventional MT, T_1 is underestimated. When S_{T1} is increased due to inverse MT, T_1 is overestimated. Black solid line denotes the true T_1=1253 ms obtained when $\delta_{MT,inc}$=0. Note that this simulation is entirely for illustrative purposes and that the proportionality factor was set as $A=1.46\cdot10^{-4}$ s^{-1} for Q=2.39 so that t_{RF}=698 μs yielded $\delta_{MT,inc}$=0 to match the empirical results reported in in Paper II. For simplicity, f_T=1.

This means that the bias in the T_1 calculation is dominated by S_{T1} where conventional MT ($\delta_{MT,inc}(f_T\alpha_{T1}) > 0$) leads to an overestimation while inverse MT ($\delta_{MT,inc}(f_T\alpha_{T1}) < 0$) leads to an underestimation. The MT_{sat} that is created by an MT pulse (i.e. δ_{MT} in Eq. (3.14)) is based on the T_1 map, so this parameter will also be biased by incidental MT in the underlying DFA experiment, albeit in the opposite direction (overestimated at long t_{RF} and vice versa). To test the above hypothesis regarding T_1-mapping and to attempt to determine a "balanced" t_{RF}, measurements were performed in the study relating to Paper II in which t_{RF} was kept fixed between α_{PD} and α_{T1} (instead varying the peak B_1) but changed in between different DFA experiments. The resulting T_1 maps did indeed show the expected dependence on t_{RF} (shorter estimated T_1 at longer t_{RF}). A value of t_{RF} = 698 μs yielded the T_1 map most comparable with an IR-derived reference as well as with literature values of the three durations examined (211, 698 and 2003 μs),

and was thus deemed the most "balanced". Figure 3.7 shows an illustrative sketch of the above rationale, using $\delta_{\mathrm{MT}}(t_{\mathrm{RF}} = 698\ \mu\mathrm{s}) = 0$ from the experimental results as the ground-truth.

Residual transmit field bias on $\mathrm{MT_{sat}}$

As shown in equations (3.14) and (3.15), $\mathrm{MT_{sat}}$ is approximately compensated for transmit field (f_{T}) inhomogeneities when using nominal flip angles in the calculation ($\delta_{\mathrm{MT,app}}$). However, the assumption of instantaneous saturation (Eq. (2.18)) is only an approximation and there will, in fact, be a moderate decrease in M_{zb} during the MT pulse itself (Eq. (2.24)). Induced δ_{b} will thus increase slightly less than by f_{T}^2, and the observed $\delta_{\mathrm{MT,app}}$ will consequently be somewhat overcompensated. In other words, $\delta_{\mathrm{MT,app}}$ will be overestimated in low B_1^+ areas and vice versa. At 3T, this residual transmit field bias on $\delta_{\mathrm{MT,app}}$ has been empirically shown to follow a linear dependence (Helms, 2015):

$$\delta_{\mathrm{MT,app}}(f_{\mathrm{T}}) = A_{\mathrm{c}}\alpha_{\mathrm{sat}}^2(1 - B\alpha_{\mathrm{sat}}f_{\mathrm{T}}), \tag{3.32}$$

where A_{c} and B are phenomenological parameters, specific to the shape (Q), offset (Δ) and duration (t_{sat}) of the MT pulse. Re-writing Eq. (3.32) on the form:

$$\delta_{\mathrm{MT,app}}/\alpha_{\mathrm{sat}}^2 = -A_{\mathrm{c}}Bf_{\mathrm{T}}\alpha_{\mathrm{sat}} + A_{\mathrm{c}}, \tag{3.33}$$

reveals that A_{c} and B can be obtained by varying the nominal α_{sat} and performing a linear regression of $\delta_{\mathrm{MT,app}}/\alpha_{\mathrm{sat}}^2$ versus $f_{\mathrm{T}}\alpha_{\mathrm{sat}}$, where f_{T} is obtained from a separate flip angle map. After A_{c} has been obtained as the intercept, B is calculated from the slope ($m = -A_{\mathrm{c}}B$) as:

$$B = -m/A_{\mathrm{c}}. \tag{3.34}$$

The transmit field-corrected estimate, $\delta_{\mathrm{MT,corr}}$, represents $\delta_{\mathrm{MT,app}}$ in the absence of flip angle bias (i.e. $f_{\mathrm{T}} = 1$):

$$\delta_{\mathrm{MT,corr}} = \delta_{\mathrm{MT,app}}(f_{\mathrm{T}} = 1) = A_{\mathrm{c}}\alpha_{\mathrm{sat}}^2(1 - B\alpha_{\mathrm{sat}}). \tag{3.35}$$

Dividing Eq. (3.35) by Eq. (3.32) to remove the tissue-specific parameter A_{c} and solving for $\delta_{\mathrm{MT,corr}}$ yields:

$$\delta_{\mathrm{MT,corr}} = (1 - B\alpha_{\mathrm{sat}})/(1 - B\alpha_{\mathrm{sat}} f_{\mathrm{T}}). \quad (3.36)$$

where $B\alpha_{\mathrm{sat}} = C$ forms a pulse-specific linear correction factor. For the sake of completeness, the final post-hoc transmit field correction formula is as follows:

$$\delta_{\mathrm{MT,corr}} = (1 - C)/(1 - f_{\mathrm{T}} C). \quad (3.37)$$

If a pixelwise linear regression is performed, maps of A_{c} and B are obtained. In the original 3T work, B was independent of tissue type and only moderately varying across the brain. This motivated a global correction factor of $C = 0.4$ for a $t_{\mathrm{sat}} = 4$ ms Gaussian pulse with $\alpha_{\mathrm{sat}} = 220°$ and $\Delta = +2.0$ kHz.

In the work relating to Paper IV, it was of interest to assess whether the linear f_{T}-dependence observed at 3T, was indeed valid also for the wider range of local flip angles encountered at 7T. Furthermore, if the dependence was linear, it was relevant to resolve whether C needed to be adjusted for the slightly different MT pulse ($t_{\mathrm{sat}} = 4$ ms sinc main lobe with $\alpha_{\mathrm{sat}} = 180°$ and $\Delta = -2.0$ kHz).

In the subsequent 7T experiments, derived maps of A and B were quite noisy. At small local flip angles, it becomes very difficult to discern any potential non-linear behaviour, as noise becomes completely dominant (Figure 3.8). At the higher end of local flip angles, the residual bias does indeed appear to be linear. However, at the lower end, the true dependence remains obscure. As for C, it varied rather strongly between subjects and between different areas within the same subject. This is also visualized in Figure 3.8, where two similar linear fits result in either $C = 0.20$ or $C = 0.34$. In the end, a linear correction with $C = 0.34$ was settled for after calculating the mean value from multiple subjects and ROIs. In this context, it should be noted that the linear correction considerably improved homogeneity in the $\mathrm{MT_{sat}}$ maps, as demonstrated in Paper IV.

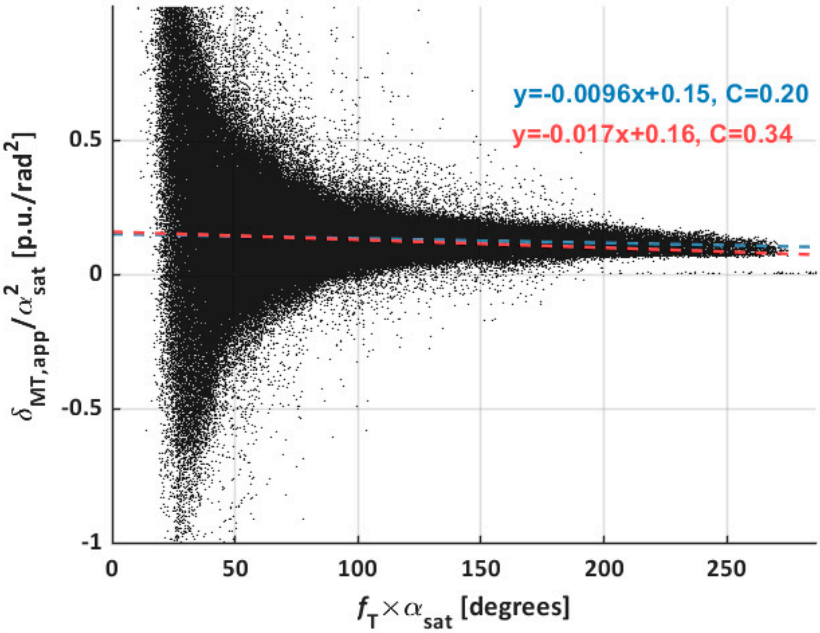

Figure 3.8. Normalized apparent MT_{sat} as a function of local flip angle. Data points were acquired from segmented WM in a subject where α_{sat} was varied as 45, 60, 80, 90, 100, 120, 135, 140, 160, and 180 degrees.There is a weak negative dependence, indicating the residual transmit field bias. The magnitude and exact behaviour of this residual bias is, however, difficult to determine due to the very low SNR at small local flip angles. Note that *x* in the equations denote the horizontal axis in radians. The blue fit with was weighted by the inverse of the SD at each local flip angle while the red fit was obtained by determining the slope and intercept from a fixed *C*=0.34.

Concluding remarks on MPM

The MPM-related research in this thesis focused almost exclusively on the derivation of T_1 and MT_{sat} maps. However, the MPM approach also facilitates mapping of PD through A and (if a multi-echo readout is employed) T_2^* (N. Weiskopf et al., 2013). Here, maps of the magnetic susceptibility (χ) from the phase data of the T_1-weighted scan were also derived. Recently, the hMRI toolbox was introduced which streamlines the process of DICOM to NIfTI conversion, coregistration, deriving the qMRI maps, as well as nonlinear registration to MNI space for multi-subject studies (Tabelow et al., 2019).

The A map derived from the DFA experiment is the product of PD and the RF receive sensitivity bias, f_R. The hMRI toolbox allows for correction of f_R through a separately acquired scan, scaled by a reference obtained by a homogenous body coil. Since a homogenous body coil is not available at 7T, this is not an option. The toolbox also provides the option to remove spatial intensity bias through the *Unified Segmentation* algorithm (Ashburner & Friston, 2005). In brief, *Unified Segmentation* assumes smoothly varying pixel intensities due to f_R, distinct from the

sharp pixel intensity gradients that arise close to tissue borders. The algorithm uses this assumption to perform simultaneous tissue segmentation and bias field correction. When f_R has been separated from A, the latter is scaled to obtain an assumed mean PD value of 69 p.u. in normal appearing WM as determined in (Volz et al., 2012).

Eight equidistant echoes with multiples of TE = 1.97 ms were routinely acquired when performing MPM. This approach allowed for an increase in SNR by averaging the echoes (Helms & Dechent, 2009) and facilitated calculation of both T_2^* and χ. By employing a log-linear fit over TE, performed simultaneously (using an approach named ESTATICS (N. Weiskopf, Callaghan, Josephs, Lutti, & Mohammadi, 2014)) for all three different weightings (T_1, PD, MT), calculation of T_2^* was again facilitated by the hMRI toolbox. ESTATICS has been shown to reduce the effects of subject motion on derived maps, assuming constant T_2^* across the different weightings. The phase data of the T_1-weighted echo train was used to perform QSM with either the MSDI (Acosta-Cabronero et al., 2018) or the MEDI algorithm (Liu et al., 2012).

The entire MPM approach is visualized in Figure 3.9, showing the same axial slice of a subject.

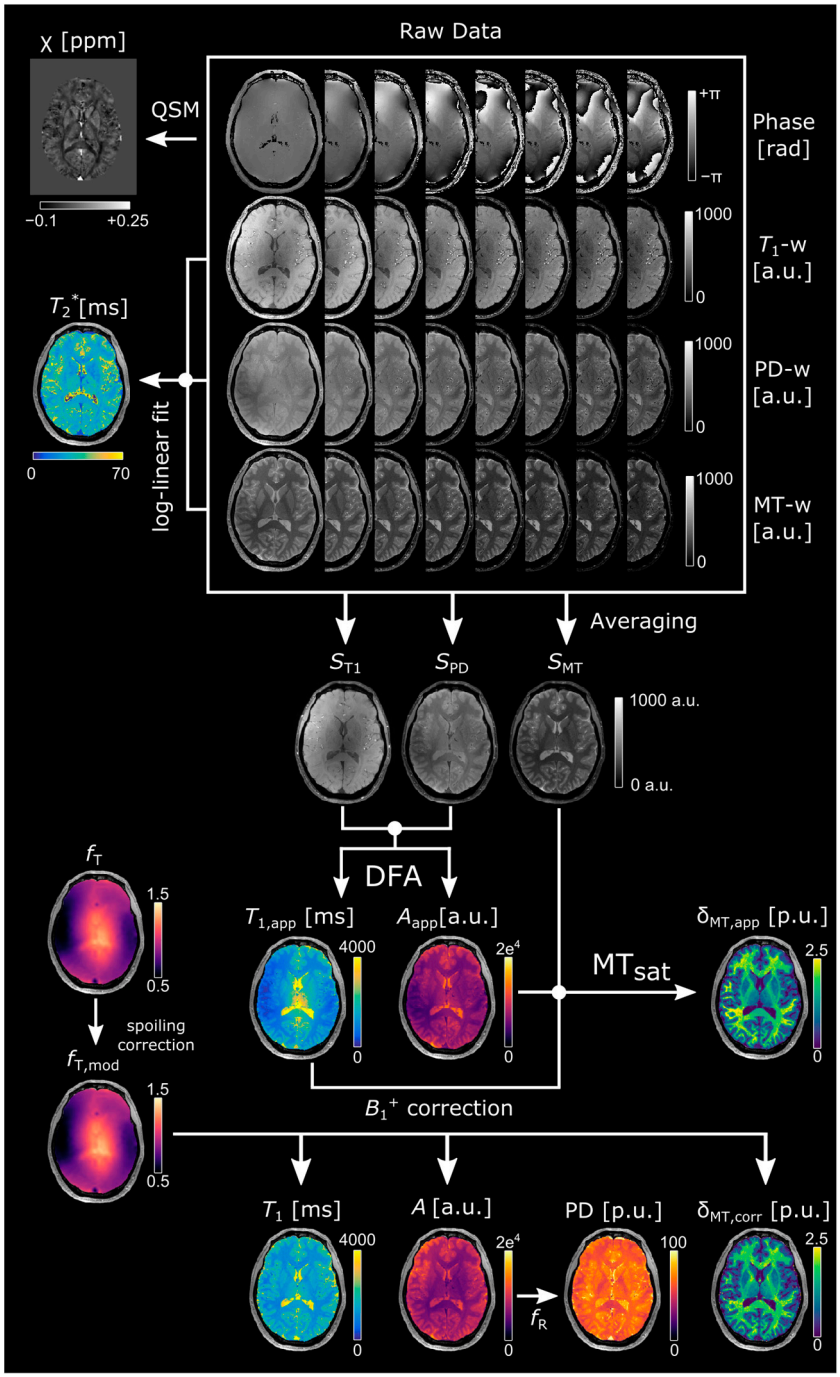

Figure 3.9. Flowchart of the MPM approach showing data from a representative subject. Note the increased spatial homogeneity after B_1^+ correction.

4 – Flip angle mapping and DREAM

The inhomogeneity of the B_1 field increases at higher B_0 due to the shortening of the RF wavelength at higher Larmor frequencies (Eq. (2.2)). At 7T, the wavelength in tissue is approximately 11-12 cm and thus somewhat smaller than the width of an average human head (15-18 cm). This means that the MRI experiment is no longer performed in the near field region, but instead in the intermediate region, where run time effects start to affect the phase of B_1. The B_1 inhomogeneity can be improved by using coils with several RF transmit channels that are driven with adapted phases and amplitudes ("RF shimming"). For a dual-channel setup, the degrees of freedom will increase from 0 to 2 compared to a single-channel coil transmitting in quadrature mode (identical amplitude of the two ports and a fixed phase difference of 90°). The resulting interferences are, however, difficult to predict and large inhomogeneities will likely remain. With the dual-transmit head coil used here, B_1 can vary from approximately 20% up to 170% of the prescribed amplitude, depending on subject head size and positioning (Figure 4.1). As the amplitude of B_1 governs the flip angle according to Eq. (2.6), the variation in local flip angle to the nominally prescribed value (as set in the user interface) is the same. For any qMRI technique based on the local flip angle being known, it thus becomes necessary to perform a correction based on a separately acquired flip angle map, and this requirement includes most techniques that are based on changes of M_z. At non-UHF strengths, it is not strictly necessary to correct qMRI maps obtained with techniques that are only moderately biased by flip angle inhomogeneities, such as MT_{sat} or MP2RAGE-based T_1-mapping. Strongly biased techniques such as DFA-based T_1-mapping will still require correction. At 7T however, inhomogeneities are so pronounced that even techniques with only a weak dependence on the local flip angle may show a visually appreciable spatially varying bias.

It is customary to use the terms "flip angle map" and "B_1^+ map" interchangeably. The latter term stems from the concept that the linearly polarized B_1 can be separated into two counter-rotating components denoted B_1^+ and B_1^-. The B_1^+ component rotates in the same direction as the rotating frame of reference and is the component related to the flip angle. The B_1^+ component is thus referred to as the transmit field of a coil. The B_1^- component rotates in the other direction (against the precession of the spin isochromats) and is thus far off resonance but relates to receive sensitivity (see *Principle of Reciprocity*, Chapter 2)). In practice, the final B_1 field is a superposition of all the fields created by each of the coils and different coils are used

for transmission and reception. Thus, the term “flip angle map” would be the more correct wording for the topic treated in this chapter.

When used to correct qMRI maps, it is convenient to denote the flip angle map by the transmit field bias (f_{T}) defined as the ratio of the local flip angle (α_{loc}) to the nominal flip angle (α):

$$f_{\mathrm{T}} = \alpha_{\mathrm{loc}}/\alpha, \tag{4.1}$$

which can alternatively be expressed in percent.

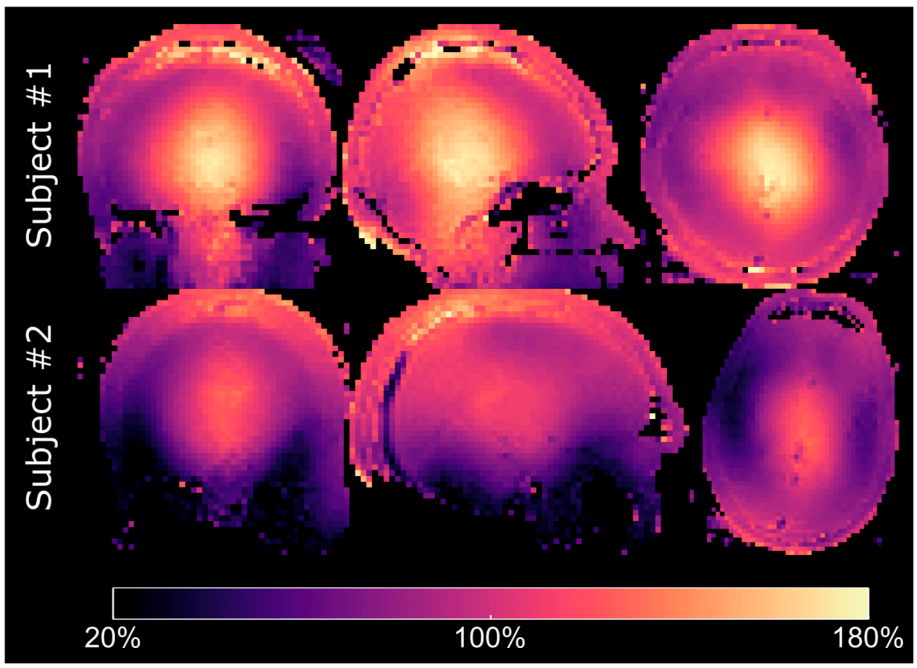

Figure 4.1. Example flip angle maps from two subjects using a dual channel transmit coil. The maps are shown in percent of the nominal flip angle. The central areas, particularly around the basal ganglia, exhibits larger local flip angles while peripheral areas such as the temporal lobess and cerebellum show smaller ones. Subject #2 has a larger and more elongated head in the anterior-posterior direction compared to Subject #1. This results in lower flip angles in the center for Subject #2 (~130% vs. ~170%). On the other hand, Subject #2 shows smaller local flip angles in the temporal lobes compared to subject #1 (~40%-~60% vs. ~70%). Note also the stronger right-left asymmetry of Subject #2.

Dual Refocusing Echo Acquisition Mode (DREAM)

Dual refocusing echo acquisition mode (DREAM) is a very fast flip angle mapping sequence, able to map the whole brain in a few seconds (Nehrke & Bornert, 2012). The multislice DREAM pulse sequence consists of a stimulated echo acquisition mode (STEAM) preparation module with preparation flip angle α (Frahm, Merboldt, Hänicke, & Haase, 1985), followed by a train of GRE modules with readout flip angle β. This produces a GRE signal of the free induction decay (FID), S_{FID}, and a stimulated echo (STE) signal, S_{STE}. Dividing the signal equations:

$$S_{\mathrm{STE}} = \sin(f_{\mathrm{T}}\beta)\frac{1}{2}\sin^2(\alpha_{\mathrm{loc}})\,M_0, \tag{4.2}$$

and

$$S_{\mathrm{FID}} = \sin(f_{\mathrm{T}}\beta)\cos^2(\alpha_{\mathrm{loc}})\,M_0, \tag{4.3}$$

and solving for α_{loc} yields:

$$\alpha_{\mathrm{loc}} = \tan^{-1}\sqrt{2\,S_{\mathrm{STE}}/2S_{\mathrm{FID}}}. \tag{4.4}$$

From here, f_{T} is obtained from Eq. (4.1). The STEAM preparation module consists of two preparation α pulses separated by time interval T_{S} and dephaser gradient G_{m2}. The first α pulse excites magnetization into the transverse plane where it is dephased ("prepared") by G_{m2} and then returned ("stored") to the longitudinal plane by the second α pulse. If $\alpha_{\mathrm{loc}} \neq 90°$, transverse magnetization will remain and is subsequently spoiled by gradient G_{spoil} (a spoiler gradient is simply a dephaser gradient with a larger area). The imaging module starts with a β pulse that excites "fresh" magnetization into the transverse plane as well as inverting a small portion of the longitudinally stored magnetization. This is followed by dephaser gradient G_{m1} and then readout gradient G_{m} (standard GRE sequence) under which the echo constituting S_{FID} is formed first, followed by S_{STE}.

The process of different echoes being formed during the same pulse sequence through alternative "echo pathways" is nicely illustrated by the concept of extended phase graphs (Weigel, 2015). In brief, magnetization is described as being partitioned into "configuration states" that describe the degree and direction of dephasing, as well as in which plane (longitudinal/transverse) the magnetization resides. Figure 4.2 visualizes the DREAM sequence using the extended phase graph concept. When a pathway crosses the horizontal axis, an echo is formed. The echo

classification (FID, spin echo or STE) is determined by the pathway of the magnetization prior to echo formation.

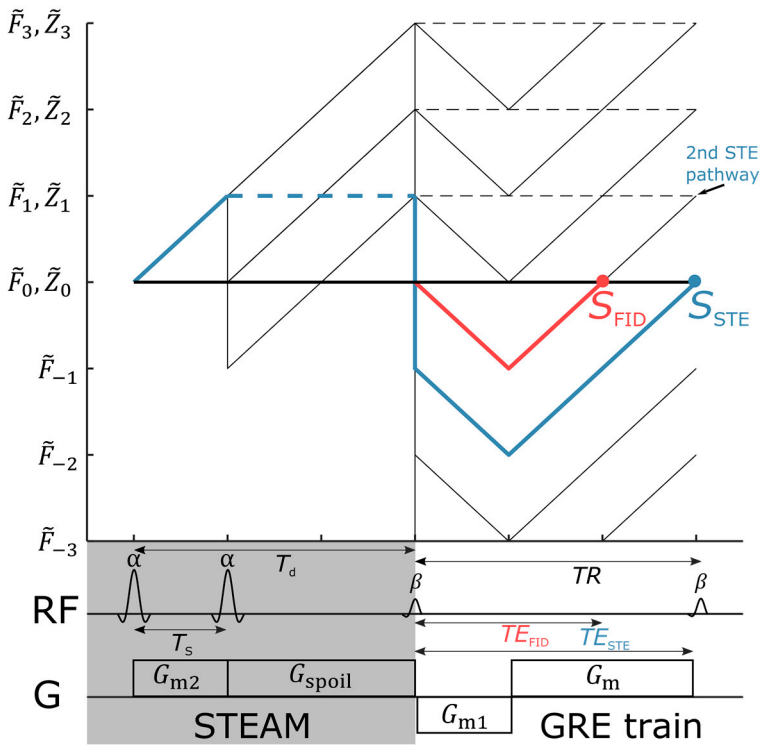

Figure 4.2. Extended phase graph visualization and pulse sequence diagram showing a simplified version of a DREAM sequence. Black lines show different pathways of the magnetization created by RF excitation. Dashed lines denote magnetization that is "stored" in the longitudinal plane and therefor not dephased/rephased by gradients. When a pathway crosses the bold horizontal line at $\tilde{\boldsymbol{F}}_{\boldsymbol{0}}, \tilde{\boldsymbol{Z}}_{\boldsymbol{0}}$, the spin isochromats are rephased and an echo is formed. The pathway of the STE is denoted in blue and the pathway of the FID is denoted in red. There is also a spin echo formed during the STEAM preparatory module but it is not acquired. Note also the pathway (arrow) that will form the *next* STE during the second imaging module within the GRE train.

The periodicity of the tangent function sets the theoretical limit of the DREAM approach to $0° \leq \alpha_{\mathrm{loc}} \leq 90°$. At $\alpha_{\mathrm{loc}} > 90°$, DREAM will return underestimated values as $180° - \alpha_{\mathrm{loc}}$. Effects from the Rician noise floor can affect the estimation at the lower end of the theoretical range (Figure 4.3). At the lower end, S_{STE} will approach the noise floor faster than S_{FID} and thus dominate imposed bias which manifests as an overestimation of α_{loc}. At the upper end, this dynamic is reversed as S_{FID} will be very low while S_{STE} is high, and α_{loc} could be consequently underestimated. In the experiments pertaining to Paper III, an underestimation was observed at high local flip angles although this was attributed to slice profile effects, and Rician noise effects was not considered in this regard. The observed overestimation at the lower end was, however, attributed to Rician noise which will lead to a stronger bias than at the upper end.

Relaxation will generally affect S_{FID} and S_{STE} differently. From Figure 4.2, it is clear that spin isochromats associated with S_{STE} will experience more T_2 decay due to being in the transverse plane longer than the S_{FID} components (×2 in the figure). Ideally, TE_{STE} should be set as short as possible, since a long TE_{STE} (relative TE_{FID}) in combination with a short T_2 will result in an underestimation of α_{loc} (Figure 4.4). A shorter TE_{STE} can be obtained by inverting the polarity of G_{m2} as this will result

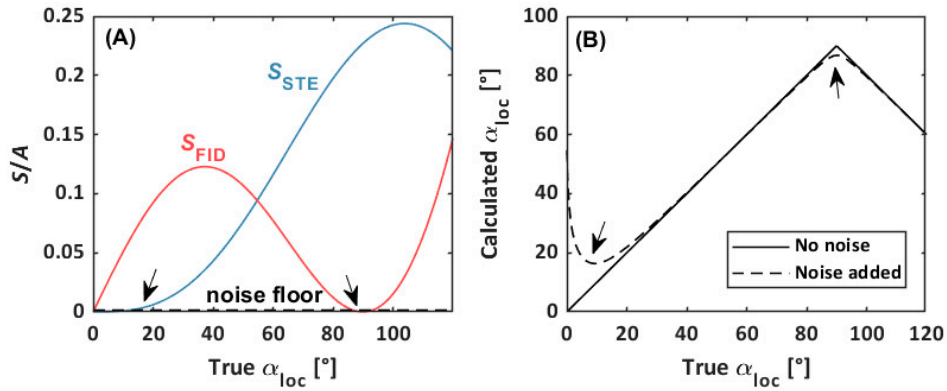

Figure 4.3. (A) The S_{STE} (blue) and S_{FID} (red) signal as a function of the local preparatory flip angle (α). (B) The calculated local flip angle with/without (dashed/solid) additive noise from the noise floor in panel A. The arrows denote when either S_{STE} or S_{FID} approaches the noise floor, resulting in bias. Note the steep decline in calculated αloc passed 90°. Simulation details: α/β=40°/12°, $0 \leq f_{\mathrm{T}} \leq 2$. Noise floor set to 1% of the maximum of S_{FID}.

in the S_{STE} echo forming before the S_{FID} echo (not done in the experiments pertaining to Paper III). Furthermore, the S_{STE} signal will undergo T_1 relaxation when stored in the longitudinal plane which may result in a small underestimation of α_{loc} at short T_1. Finally, T_{S} can be modified so that the T_2^* decay of S_{STE} is matched to the T_2^* decay of S_{FID}. At $T_{\mathrm{S}} = TE_{\mathrm{STE}}$, S_{STE} will be fully compensated for T_2^* decay, which introduces a bias in the flip angle map since S_{FID} will always have a T_2^* decay governed by TE_{FID}. By setting $T_{\mathrm{S}} = TE_{\mathrm{STE}} + TE_{\mathrm{FID}}$ (as done in the experiments pertaining to Paper III), both S_{STE} and S_{FID} experience the same T_2^* decay which thus factors out when applying Eq. (4.4). The simplified diagram in Figure 4.2 would also be compensated for T_2^* effects at $T_{\mathrm{S}} = TE_{\mathrm{STE}} - TE_{\mathrm{FID}}$. The practical implication of this timing would be either a very long TE_{STE} (suboptimal with respect to SNR) or a very high amplitude of G_{m2}.

Since DREAM is commonly a multislice sequence, it may suffer from slice profile related bias caused by crosstalk between neighbouring slices. Acquiring slices in an interleaved manner (odd slices first and then the even slices) is a prerequisite to obtain unbiased flip angle maps. Slice profile bias in Eq. (4.4) is further alleviated by using a broader slice thickness in the STEAM module relative the GRE imaging module. The ratio of the slice thickness in the STEAM module relative the GRE module is referred to as the slice thickness ratio. Lastly, the time between excitation of two neighbouring slices (T_{shot}) can be increased to allow for full relaxation ($5 \times T_1$). In the original work, this was done by increasing the number of slices

beyond the imaged object, but the current implementation allows to set T_{shot} independently of the FOV. Slice profile bias relates to T_1 but is separate from the negligible T_1 bias in Figure 4.4.

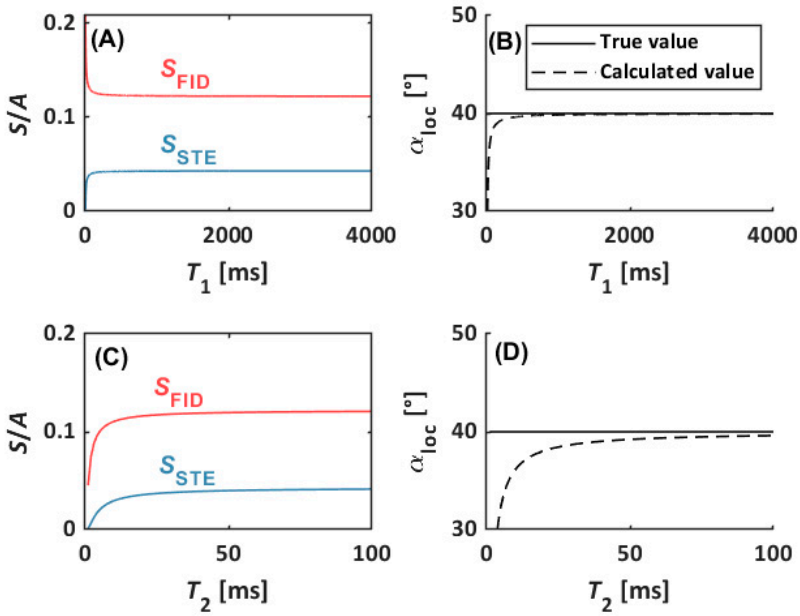

Figure 4.4. Bias in DREAM flip angle mapping due to T_1 or T_2 relaxation. Left column shows the S_{STE} (blue) and S_{FID} (red) relative signal as a function of either T_1 (A) or T_2 (C). The T_1 bias is quite negigble (B) while the T_2 bias of this ("FID" first pulse sequence) becomes quite serious at short T_2 values (D). At the 7T average of T_2 = 50 ms the bias is, however, <1°. Simulation details: α/β=40°/12°, $TE_{STE}/TE_{FID}/TS/TD$ = 1.39/0.99/2.38/6.08 ms. The T_2 was set infiniteley long when simulating T_1-related bias and vice versa.

As T_1 increases at 7T, sensitivity to slice crosstalk increases, demanding a longer T_{shot}. The increased range of α_{loc} due to B_1 inhomogeneities compared to 3T will increase sensitivity to bias from Rician noise and slice profile effects.

The use of several preparation flip angles

In Paper III, a small underestimation of the local flip angle at $\alpha_{\mathrm{loc}} > 50°$ in a phantom and in vivo is demonstrated. In the paper, this is tentatively explained by deviations in the slice profiles, not represented by the signal equations (4.2) and (4.3). This claim was supported by simulations of the STEAM pulse shape at various α_{loc}, indicating that the deviations were relevant even at a slice thickness ratio of 2.0. At the lower end of the f_{T} range, an overestimation was observed at $\alpha_{\mathrm{loc}} < 20°$ which was likely due to Rician noise. Here, it is worth noting that the upper limit of 50° should be independent of research site, while the lower limit of 20° will depend

on other factors of the pulse sequence, such as β, TE_{FID}, TE_{STE}, voxel size, and also on receiver equipment since it pertains to low SNR.

The work described in Paper III was initially motivated by observed blurring artifacts, appearing in the temporal lobes and cerebellum (areas with low f_{T}) of DFA-derived T_1 maps. It was determined that the cause of these artifacts was the low SNR of the DREAM flip angle map used for correction. Increasing the preparation flip angle α resulted in signal voids in the center of the brain as α_{loc} approached 90°. Thus, more than one DREAM sequence was acquired with different α. It was then revealed that the DREAM flip angle maps systematically varied in estimated α_{loc} based on the nominal α. To solve this problem, three DREAM sequences with nominal $\alpha = 25°$, 40°, and 60° were acquired. The obtained $100 \times f_{\mathrm{T}}$ maps (calculated directly on the scanner in %) were scaled to α_{loc} whereafter pixels where $\alpha_{\mathrm{loc}} < 20°$ and $\alpha_{\mathrm{loc}} > 50°$ were masked. The three masked maps were then combined into a single high-SNR map free of bias from Rician noise and slice profile effects. In pixels where there are more than one non-zero value, the average is calculated. Since the $\alpha = 60°$ map will contain a signal void in the center, it is important to perform the combination prior to coregistration to any high-resolution image volume, as this procedure will interpolate between finite-valued and zero-valued pixels, creating artificially underestimated local flip angles. The steps of the combination process are visualized in Figure 4.5.

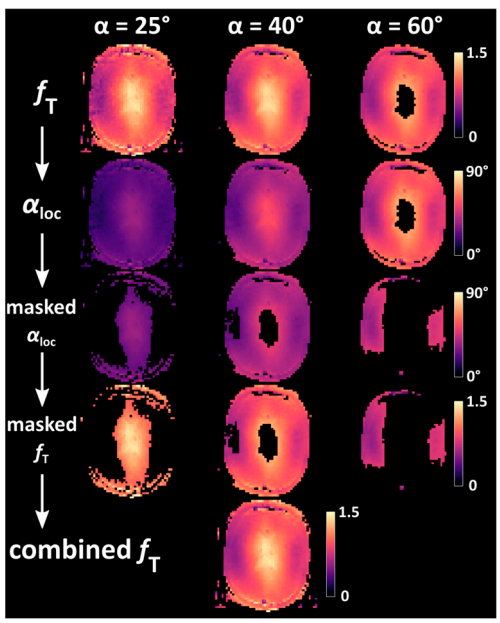

Figure 4.5. Flowchart showing the process of combining separately acquired DREAM flip angle maps with nominal preparation flip angles of α = 25, 40 and 60°. The flip angle maps (f_T) are first scaled to the local flip angle, α_{loc}, separately masked in pixels with $\alpha_{loc} < 20°$ or $\alpha_{loc} > 50°$, scaled back to f_T and then combined through non-zero averaging into a high-SNR bias-free map. Note the central signal void in the α = 60° map.

5 – MPRAGE-based qMRI

The MPRAGE sequence was introduced to obtain T_1-weighted 3D images with a high WM-GM contrast and short scan time (Mugler & Brookeman, 1990, 1991). It has since become a standard for structural imaging T_1-weighted imaging (Deichmann, Good, Josephs, Ashburner, & Turner, 2000). The sequence consists of three modules within an encompassing cycle, TC (Figure 5.1). Enhanced tissue contrast is obtained by a magnetization preparation (MP) module consisting of an inversion pulse and a subsequent period of free T_1 relaxation. This is followed up by a train of $TF = N_\mathrm{y}$ spoiled GREs with a varying inner loop phase encoding gradient, sampling a 2D plane of the 3D k-space. The last module consists of a recovery period, TD, before the magnetization is inverted again and a new cycle (with a different outer loop phase encoding) starts. The process is repeated N_z times until the desired 3D k-space has been sampled. The M_z reaches a steady state *between* sequential cycles after only a few iterations. The default acquisition time is:

$$T_\mathrm{acq} = N_\mathrm{z} \times TC. \tag{5.1}$$

The readout train, referred to as a rapid acquisition gradient echo (RAGE), has a duration of $TF \times TR$. The inversion time, TI, is defined as the time from inversion to the center of the 2D k-space plane. Note that the definitions of TI, TD etc. tend to vary in the literature.

For three typical Cartesian phase encoding orders, TC is calculated as:

Linear: $$TC = TI - \frac{TF \times TR}{2} + TF \times TR + TD, \tag{5.2a}$$

Centric: $$TC = TI + TF \times TR + TD, \tag{5.2b}$$

Reverse centric: $$TC = TI + TD. \tag{5.2c}$$

The T_1 contrast is governed by these sequence timings as well as the flip angle. The TE is typically very short and T_2^*-weighting can thus be ignored. Unlike the ordinary spoiled GRE, the RAGE is acquired under transient conditions, i.e. a changing M_z and thus a changing WM-GM contrast. This means that the phase encoding order

also influences the overall contrast, which is dominated by M_z at the center of k-space. During the RAGE, M_z approaches an inner loop steady state ($M_0^* < M_0$) with time constant ($T_1^* < T_1$) (Deichmann et al., 2000; Deichmann & Haase, 1992):

$$T_1^* = [1/T_1 - 1/TR \cdot \ln(\cos(f_T \alpha))]^{-1}, \tag{5.3}$$

$$M_0^* = M_0 \cdot \frac{1 - \exp(-TR/T_1)}{1 - \exp(-TR/T_1^*)}. \tag{5.4}$$

For $f_T \alpha \to 0$ it follows that $T_1^* \to T_1$ and $M_0^* \to M_0$. This steady state can be referred to as a driven equilibrium to distinguish it from the outer loop steady state between sequential cycles. The transition in M_z leads to a signal weighting across k-space which manifests as a distortion of the point spread function (PSF). This distortion is exacerbated if the polarity of M_z changes sign close to acquisition of (Deichmann et al., 2000). The TR is typically kept short to reduce the duration of the RAGE. In summary, an MPRAGE image has the benefit of enhanced WM-GM contrast, compared to a standard spoiled GRE, by the use of inversion and a corresponding increase in the dynamic range of M_z. However, MPRAGE may suffer from PSF distortions as well as a longer scan time.

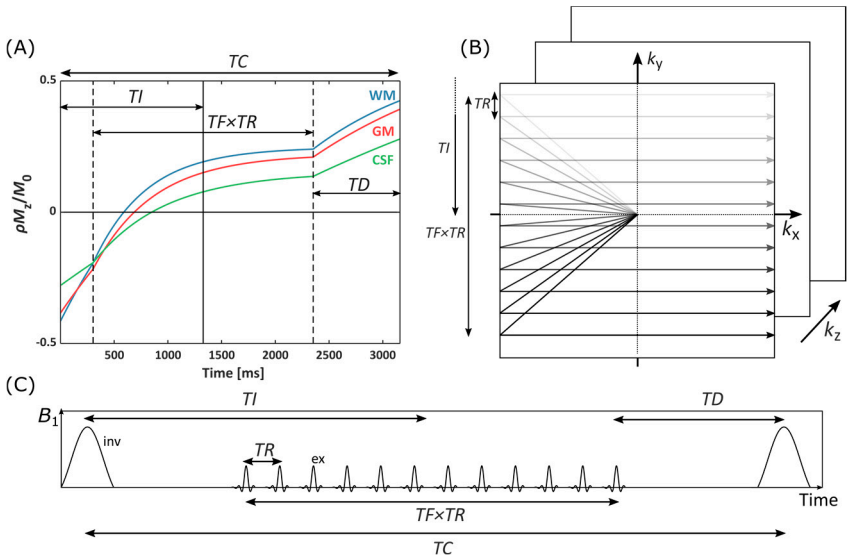

Figure 5.1. Summary of a single-shot MPRAGE sequence with linear phase encoding and full k-space sampling.(A) Development of M_z during *TC* for WM (blue, T_1 = 1300 ms, ρ = 0.65), GM (red, T_1 = 1900 ms, ρ = 0.75) and CSF (green, T_1 = 4300 ms, ρ=1.0). The MP leads to a larger separation of WM and GM at *TI* (solid black vertical line) compared to the steady state acquired by the end of the RAGE (the RAGE is encompassed by the dashed lines). (B) Sampling of a plane in k-space during *TR*×*TF*. When *TF* lines have been sampled, the next inversion pulse is applied and the process is repeated N_z times. (C) Applied RF pulses during *TC*. The cycle begins with an inversion pulse, followed by a delay and then a readout train of excitation pulses (RAGE). Lastly, there is another delay, *TD*, until the next inversion pulse at the beginning of the next cycle. Simulation details: *TC*/*TI*/*TD*/*TR* = 3500/1200/808/8 ms, *TF* = 256, $f_{\mathrm{T}}\alpha$ = 8°, f_{inv} = 0.96, 3 cycles to obtain an outer loop steady state. The *TF* was reduced to 12 in (B) and (C) for visual clarity.

Partial k-space sampling

Other acquisition considerations pertain to partial k-space sampling techniques such as partial Fourier, parallel imaging and elliptical k-space sampling. The common purpose of all these techniques is to reduce scan time by sampling less k-space lines. In partial Fourier, asymmetric sampling is employed so that only one half of k-space is fully sampled (Feinberg, Hale, Watts, Kaufman, & Mark, 1986). Unmeasured k-space data is then substituted through zero-filling or homodyne processing. In parallel imaging, the distance between k-space lines are increased while the maximal extent in k-space is maintained. If a phased array is used, ensuing aliasing due to the reduced FOV can be either removed or prevented by the individual sensitivity of the coil elements. One such technique is SENSE, where the aliased images are unfolded in image space (Pruessmann et al., 1999). Elliptical k-space sampling pertains to omitting the low-SNR diagonal corners of k-space. In 3D, the sampled portion forms an elliptic cylinder inside the cuboid k-space. To maintain a constant *TI*, a zigzag *k*-space trajectory is employed, alternating between the inner and outer phase encoding directions (k_y and k_z) during the RAGE. Trajectories in

the periphery have a larger variation in the outer loop phase encoding direction to maintain the same number of sampled k-space lines (Figure 5.2), and *TF* can thus be chosen independently of N_y. The trajectories are optimized in such a way that the contrast is unaffected. An analogous concept for TSE-imaging has been introduced as "view orders" (Busse et al., 2008). On the system used here, it is referred to as the "3D free factor".

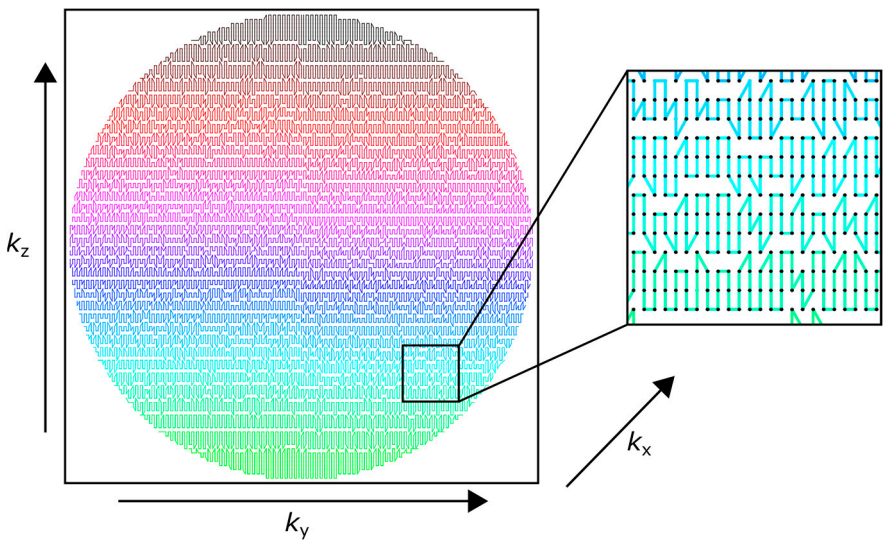

Figure 5.2. Ellipitcal phase encoding, showing zigzag k-space trajectories during individual RAGE trains (color coded). Since k_y denotes the inner loop, variation during each RAGE is primarily in this direction. However, there is also some variation in the outer loop (k_z) direction, ensuring that each RAGE contains the same number of k-space lines (denoted as dots since the readout k_x direction is through plane). Thus, trajectories far from k_z=0 (black and light green), varies more in the k_z direction.

Some partial k-space sampling settings may have an influence on the pulse sequence timing parameters. For instance, a varying *TI* between RAGE trains was observed when using partial Fourier in the inner loop phase encoding direction in conjunction with an elliptical phase encoding.

Correction of B_1-induced spatial bias in MPRAGE

In a standard spoiled GRE, M_z is always in a driven equilibrium in all voxels of the acquired volume as the central k-space line is acquired. Only the value of M_0^* and the amount of magnetization flipped into the transverse plane by $f_T\alpha$ will vary and lead to a B_1-dependent spatial bias. For MPRAGE on the other hand, signal homogeneity is affected by a third factor in the form of T_1^* (Eq. (5.3)). Whether M_z is in a steady state (as well as the closeness to that steady state) depends on T_1^* and will be spatially dependent. This further implies that the phase encoding order may have an influence on the spatial signal homogeneity. An ordinary T_1-weighted spoiled GRE may still show a stronger spatial bias depending on coil setup, however, since it typically employs a higher flip angle than MPRAGE.

Sensitivity to B_1 inhomogeneity in MPRAGE can be reduced by a separately acquired spoiled GRE with a predominantly PD-weighted contrast (Van de Moortele et al., 2009). If S_{MP} is the magnetization prepared signal and S_{GRE} is the reference GRE signal, the corrected signal is obtained by a simple ratio:

$$S_{MP/GRE} = \frac{S_{MP}}{S_{GRE}} = \frac{f_R \rho M_{z,MP}(T_1^*)\sin(f_T\alpha_{MP})\exp(-TE/T_2^*)}{f_R \rho M_{z,GRE}\sin(f_T\alpha_{GRE})\exp(-TE/T_2^*)} = \frac{M_{z,MP}(T_1^*)\sin(f_T\alpha_{MP})}{M_{z,GRE}\sin(f_T\alpha_{GRE})}, \quad (5.5)$$

where f_R denotes the receive sensitivity after combination of channels and ρ is the PD. The underlying idea is that S_{MP} and S_{GRE} are affected by the same sensitivity and transmit fields and that the influence of those fields can be "divided out" in the corrected image. Further, since S_{GRE} lacks the MP-induced T_1-contrast of S_{MP}, T_1-weighting is not reduced by the division. On the contrary, given that both acquisition voxels are the same size, they will also share the same spin system so that influence of PD and T_2^* is removed from the normalized image to create a "pure" T_1 contrast. Removal of PD influence will, in fact, increase the WM-GM contrast as ρ is typically higher in GM than in WM. This was successfully demonstrated in Paper I. Both acquisitions should further have identical bandwidths per pixel so that the fat signal displacement does not vary. As previously mentioned, $M_{z,MP}$ experiences an additional influence from f_T in the form of T_1^*. Thus, the transmit component of B_1 is partly compensated for by the division, but not removed entirely (even for $\alpha_{MP} = \alpha_{GRE}$) as is the case for f_R. Careful choice of α_{MP} and α_{GRE} will minimize the residual f_T dependence. To this end, α_{GRE} should be kept small. A small α_{GRE} also means that the T_1 contrast in $S_{MP/GRE}$ is not reduced.

As in the MPM-technique, algebraic operations applied to the raw images will lead to noise propagation into the resulting image or map. Compared to the SNR of S_{MP} (SNR_{MP}), the SNR of $S_{MP/GRE}$ ($SNR_{MP/GRE}$) will be (Van de Moortele et al., 2009):

$$SNR_{\mathrm{MP/GRE}} = \frac{SNR_{\mathrm{MP}}}{\sqrt{1 + S^2_{\mathrm{MP/GRE}}}}. \quad (5.6)$$

A benefit of Eq. (5.6) is that the reduction in SNR is larger for high values of $S_{\mathrm{MP/GRE}}$, so that pixels with low S_{MP} and thus low inherent SNR are less affected by the noise progression. For some typical normalized pixel intensities of $SNR_{\mathrm{MP/GRE}} = 0.97/0.60/0.39$ in WM/GM/CSF respectively (acquired by the 0.7 mm isotropic protocol described in Paper I) the decrease in SNR would be 28/14/6.8% compared to the initial SNR_{MP}. The previously described increase in WM-GM contrast will counteract this decrease in SNR and the CNR may actually be higher in $S_{\mathrm{MP/GRE}}$.

As the spatial variation of B_1 is dominated by low spatial frequencies, the voxel size of the reference GRE could be increased to reduce scan time (van Gelderen, Koretsy, de Zwart, & Duyn, 2006), although this can potentially blur the "pure" T_1 contrast as the above rationale regarding identical spin systems is no longer strictly true. The sequential acquisition of S_{MP} and S_{GRE} is suboptimal since it is likely to require offline post-processing in the form of rigid (6 parameters) co-registration. Perhaps more importantly, it cannot exploit the negative dynamic range of M_z to increase conventional WM-GM contrast (bright WM, darker GM), as the polarity of M_z cannot be determined from two separate scans. A sequential approach is, however, less sensitive to intra-scan subject motion.

Inversion pulse

It is suboptimal to employ standard RF pulses for inversion as the inversion efficiency (the proportion of M_z that is inverted at the end of the cycle) will vary due to B_1 inhomogeneities. This is of course especially true at UHF strengths. Hence; an adiabatic RF pulse is normally employed instead. An adiabatic pulse is both amplitude and frequency modulated and very insensitive to B_1 inhomogeneities above a certain threshold amplitude, referred to as the adiabatic condition. As the duration of an adiabatic inversion pulse is typically of the same order of magnitude as the T_2 in tissue, local inversion efficiency could potentially be biased as observed at 9.4T (Hagberg et al., 2017). Due to the B_0-dependency of T_2, this spatially imposed bias should be smaller at 7T compared to 9.4T although larger than at 3T. In the experiments relating to Paper V, an adiabatic 13 ms inversion pulse, tailored for UHF, was used (Hurley et al., 2010).

MP2RAGE

The reference GRE can also be acquired in an interleaved fashion to reduce inter-scan subject motion and facilitate inherent coregistration of the two image volumes (Van de Moortele et al., 2009). The MPRAGE and reference GRE are acquired within the same TC at two different TI values: S_1 at TI_1 and S_2 at TI_2 (Figure 5.3). The two RAGE trains may be separated by an additional short delay. The MP2RAGE approach expanded on this concept by replacing $S_{\mathrm{MP/GRE}}$ in the standard ratio of Eq. (5.4) with the complex combination (Marques et al., 2010):

$$S_{\mathrm{MP2RAGE}} = \mathrm{Re}\left(\frac{S_1 \cdot S_2^*}{|S_1|^2 + |S_2|^2}\right), \tag{5.7}$$

where the asterisk denotes the complex conjugate. As opposed to their respective counterparts (the magnitude signals S_{MP} and S_{GRE} in Eq (5.5)), S_1 and S_2 here denotes complex signals with $|S_1|$ and $|S_2|$ being the respective magnitudes. Eq. (5.7) implies the same benefits as Eq. (5.5), i.e. removal of influence from PD, T_2^* and f_{R} as well as a reduction of f_{T} bias. The added benefit comes from the preservation of the relative phase information, i.e. any change in sign in the polarity of M_{z} between TI_1 and TI_2 can be identified. This becomes clear if Eq. (5.7) is first expanded as (Helms, Lätt, & Olsson, 2020):

$$S_{\mathrm{MP2RAGE}} = \frac{\mathrm{Re}(S_1)\mathrm{Re}(S_2) + \mathrm{Im}(S_1)\mathrm{Im}(S_2)}{\mathrm{Re}(S_1)^2 + \mathrm{Im}(S_1)^2 + \mathrm{Re}(S_2)^2 + \mathrm{Im}(S_2)^2}. \tag{5.8}$$

An identical result is obtained if the numerator in Eq. (5.7) is instead $S_1^* S_2$. Thus, both versions can be found in the literature (Marques & Gruetter, 2013; Marques et al., 2010). If Eq. (5.8) is instead expressed in terms of magnitude

$$|S_{1,2}| = \sqrt{\mathrm{Re}(S_{1,2})^2 + \mathrm{Im}(S_{1,2})^2}, \tag{5.9a}$$

and phase

$$\phi_{1,2} = \tan^{-1}\left(\mathrm{Im}(S_{1,2})/\mathrm{Re}(S_{1,2})\right), \tag{5.9b}$$

the following expression is obtained:

$$S_{\mathrm{MP2RAGE}} = \frac{|S_1|/|S_2|\cos(\phi_1 - \phi_2)}{|S_1|^2/|S_2|^2 + 1}. \tag{5.10}$$

Here, the removal of f_{R} bias and the semi-quantitative nature of MP2RAGE becomes evident by the ratio $|S_1|/|S_2|$. The change in polarity is identified by the cosine function, where ϕ_2 serves as a reference which is assumed to be of positive polarity. This means that the central k-space line no longer needs to be acquired after the zero-crossing. Thus, TI_1 can be shortened to better utilize the dynamic range obtained after the inversion. This can considerably increase WM-GM contrast. Other benefits of Eq. (5.7) includes the fact that S_{MP2RAGE} will be limited to values between −0.5 and +0.5. This increases comparability between different research sites and protocols since this range of possible values determines the display window range. It also conveniently limits the values of background noise pixels. A potential drawback of such a constriction is that pixel intensities may become "saturated" for a certain protocol after, for example, injection of a contrast agent, which would strongly reduce contrast. Further, the SNR in the case described by Eq. (5.7) is increased compared to the one in Eq. (5.5). The MP2AGE protocol used as a comparison in Paper I yielded pixel intensities in WM/GM/CSF of approximately +0.36/−0.15/−0.47, an increase in the WM-GM pixel intensity difference by 38% compared to the protocol for sequential normalization.

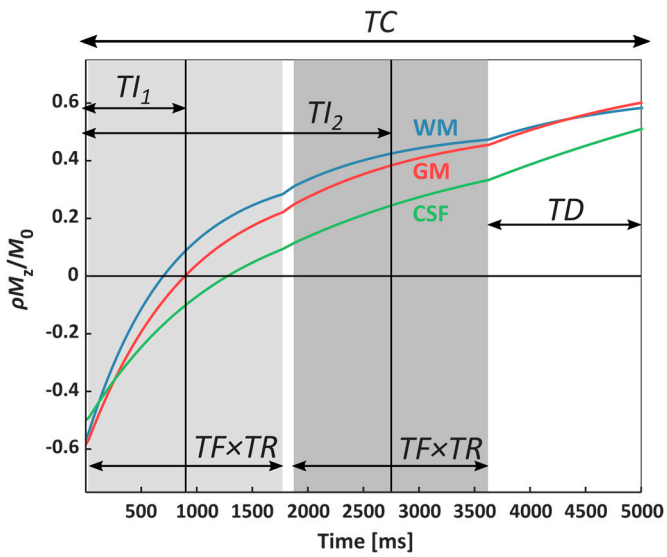

Figure 5.3. Development of M_z during *TC* in an MP2RAGE experiment, analogous to panel A in Figure 5.1 for MPRAGE. The colored lines denote WM (blue, T_1 = 1300 ms, ρ = 0.65), GM (red, T_1 = 1900 ms, ρ = 0.75) and CSF (green, T_1 = 4300 ms, ρ = 1.0). The first RAGE is marked by a light gray background with a vertical line denoting TI_1 and starts almost instantly after the inversion. The second RAGE is marked by a darker gray background with TI_2 denoted by a second vertical line. Note the larger dynamic range of M_z compared to the standard MPRAGE in Figure 5.1. Note also that the M_z of CSF has a negative polarity at TI_1. Simulation details: *TC*/TI_1/TI_2/*TD*/*TR* = 5000/900/2750/6.8 ms, *TF* = 256, $f_{\mathrm{T}}\alpha_{\mathrm{TI1}}/f_{\mathrm{T}}\alpha_{\mathrm{TI2}}$ = 5°/3°, f_{inv} = 0.96, 3 cycles to obtain an outer loop steady state.

MP2RAGE T_1-mapping

The restriction of $-0.5 \leq S_{\mathrm{MP2RAGE}} \leq +0.5$ and semi-quantitative nature of the MP2RAGE technique allows for conversion of S_{MP2RAGE} into T_1 by forward signal modeling (Figure 5.4). If mono-exponential relaxation is assumed, M_z and hence S_{MP2RAGE} can be rather easily simulated as the MP2RAGE cycle alternates between free T_1 relaxation towards M_0, and a driven progression during the readout train towards M_0^* with time constant T_1^*, as described by equations (5.3) and (5.4). To simulate M_z requires stating the flip angles (α_1 and α_2), TF, TR, TI_1, TI_2 as well as TC. For a more accurate simulation, a separate flip angle map can be added to obtain the local flip angles $f_T\alpha_1$ and $f_T\alpha_2$ (Marques & Gruetter, 2013).

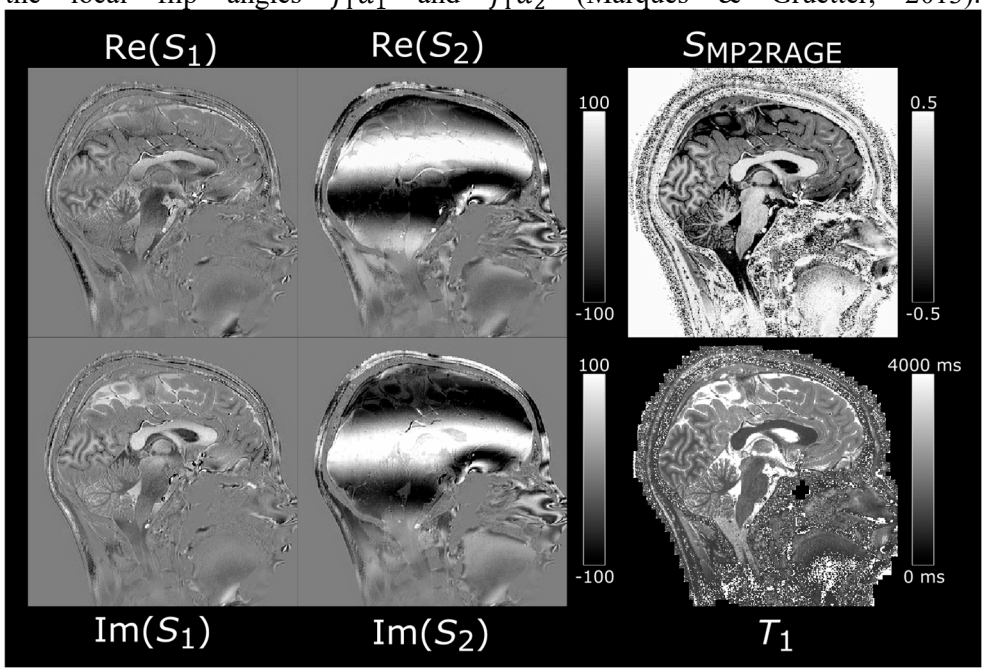

Figure 5.4. Complex MP2RAGE raw data at TI_1 and TI_2. The "MP2RAGE image" ($S_{MP2RAGE}$) is derived using Eq. (5.7) and the T_1 map is derived from forward signal modeling of $S_{MP2RAGE}$ (f_{inv} = 0.96). The T_1 map also used a separetley acquired flip angle map for f_T bias correction. Note the lack of tissue contrast at TI_2 as M_z has passed the zero-crossing for all T_1 values. Acquisition details: $TC/TI_1/TI_2/TD/TR$ = 5000/900/2750/6.8 ms, TF = 256, $\alpha_{TI1}/\alpha_{TI2}$ = 5°/3°.

MP3RAGE

The residual f_T bias in MP2RAGE-derived T_1 maps served as a motivation for introducing the MP3RAGE sequence in Paper V. The purpose of this technique is to quantify both T_1 and f_T simultaneously, thereby obtaining inherently co-registered whole brain maps of both these MR parameters at the same high spatial resolution. As the name implies, a third RAGE is appended to the end of the MP2RAGE cycle (Figure 5.5). This third RAGE is applied with a relatively high flip angle (α_{high}) compared to what is typically used in MP2RAGE sequences. The high flip angle quickly forces the spin system into a T_1-weighted driven equilibrium

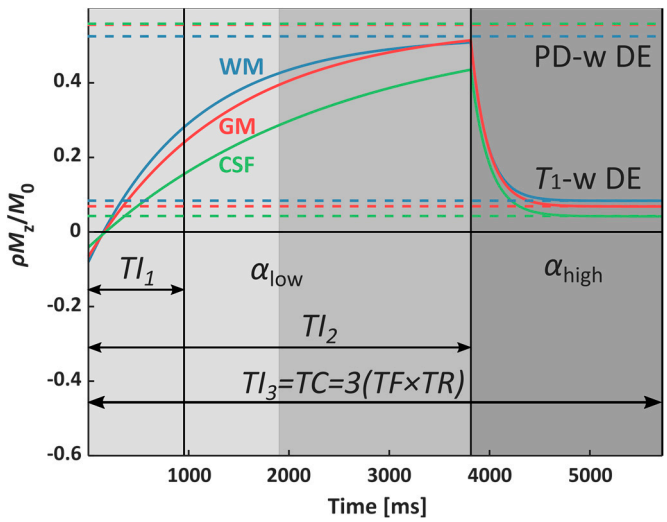

Figure 5.5. Development of M_z (solid colored lines) during *TC* in an MP3RAGE sequence, analogous to Figure 5.3 for MP2RAGE. The colored lines denote WM (blue, T_1 = 1300 ms, ρ = 0.65), GM (red, T_1 = 1900 ms, ρ = 0.75) and CSF (green, T_1 = 4300 ms, ρ = 1.0). The three readout trains are denoted by different shades of gray background. The cycle contains no "dead time" of free relaxation (no white background). The first two readout trains are acquired using the same low flip angle (α_{low}) so that M_z can progress undisturbed towards a PD-weighted driven equilibrium (DE) (upper dashed lines). The third RAGE is acquired with a higher flip angle (α_{high}) and is quickly forced into a T_1-weighted driven equilibrium (lower dashed lines) before TI_3 = *TC* and the next inversion. Note the smaller dynamic range compared to MP2RAGE in Figure 5.3 which affects precision. The three readout trains are acquired using a linear/reverse centric/reverse centric phase encoding order. Simulation details: *TC*/TI_1/TI_2/TI_3/*TR* = 5721/954/3814/5721/7.45 ms, *TF* = 256, $f_T\alpha_{low}/f_T\alpha_{high}$ = 3°/16°, f_{inv} = 0. 96, 3 cycles to obtain an outer loop steady state.

(very short T_1^* and a low M_0^*). Note that there is no free T_1 relaxation after the third RAGE. Thus, if the driven equilibrium is reached during the cycle, the outer loop steady state is automatically enforced. Immediately after inversion, the first and second readout trains are acquired at a lower flip angle (α_{low}) and identical TR under transient conditions towards a PD-weighted (high M_0^*) driven equilibrium with a longer T_1^*. The three resulting images, acquired at TI_1, TI_2 and TI_3, respectively, are referred to as S_1, S_2 and S_3. The S_1 image obtains a T_1-weighting from the inversion recovery with moderate f_T bias and resembles a typical MPRAGE image. The S_2 image is PD-weighted with moderate f_T bias and

resembles the S_{PD} image in a DFA experiment. The S_3 image is T_1-weighted with a heavy f_{T} bias and should be completely analogous to the S_{T1} image in a DFA experiment (but the S_3 nomenclature will be used in the context of MP3RAGE).

The idea is to combine a DFA experiment with an MP2RAGE sequence and to exploit the f_{T} dependence of both $T_{1,\mathrm{app}}$ and T_1^* to solve for T_1 and f_{T} simultaneously. The first step is to perform a fit of the progressive partial saturation towards M_0^* under α_{PD} during the first two RAGE trains, based on S_1 and S_2, thus, determining the longer T_1^* as well as the hypothetical signal acquired at the PD-weighted driven equilibrium (S_{PD}) at $TI \to \infty$ as:

$$S_{1,2} = S_{\mathrm{PD}} + (S_0 - S_{\mathrm{PD}})\exp\left(-TI_{1,2}/T_1^*\right). \tag{5.11}$$

where S_0 is the hypothetical signal that would have been acquired at $TI = 0$ ms, α_{low} and the same TR as S_1 and S_2. As S_{PD} here is analogous to S_{PD} in the DFA experiment (but different from S_2) it will be referred to by that same nomenclature. This is analogous to a standard inversion recovery experiment (Eq. (2.10)) albeit with T_1^* instead of T_1. The problem is ill-posed with three unknown parameters and only two data points. However, if a global f_{inv} can be assumed (and $TD = 0$ ms), S_0 can be approximated from S_3 as:

$$S_0 = -f_{\mathrm{inv}} S_3 \frac{\sin(f_{\mathrm{T}}\alpha_{\mathrm{low}})}{\sin\left(f_T\alpha_{\mathrm{high}}\right)} \approx -f_{\mathrm{inv}} S_3 \frac{\sin(\alpha_{\mathrm{low}})}{\sin\left(\alpha_{\mathrm{high}}\right)}. \tag{5.12}$$

The right-hand approximation is necessary to eliminate f_{T}, which is yet unknown. The highly saturated driven equilibrium of S_3 ensures that this error has only a limited effect on the absolute value of the calculated S_0. The same applies to any moderate deviation of the assumed global f_{inv} from the local, actual, efficiency.

The fitted S_{PD} and acquired $S_3 = S_{\mathrm{T1}}$ constitutes the DFA experiment. Using the rational approximation and nominal flip angles, the apparent T_1 is obtained as:

$$T_{1,\mathrm{app}} = 2TR \frac{S_{\mathrm{PD}}/\alpha_{\mathrm{low}} - S_3/\alpha_{\mathrm{high}}}{S_3\alpha_{\mathrm{high}} - S_{\mathrm{PD}}\alpha_{\mathrm{low}}}, \tag{5.13}$$

with a quadratic f_{T} dependence (Eq. (3.11)):

$$T_{1,\mathrm{app}} = f_{\mathrm{T}}^2 T_1. \tag{5.14}$$

The next step is to exploit the f_{T} dependencies of the calculated $T_{1,\mathrm{app}}$ and the fitted T_1^* to obtain closed-form solutions for both T_1 and f_{T}. To do this, T_1^* (Eq. (5.3)) is

re-written as a rational function like $T_{1,\mathrm{app}}$, valid for small flip angles and short TR. This is done first by the linear approximation $\ln(\cos(f_\mathrm{T}\alpha_\mathrm{low})) \approx \cos(f_\mathrm{T}\alpha_\mathrm{low}) - 1$ and then by the rational approximation $\cos(f_T\alpha_\mathrm{low}) - 1 \approx -(f_\mathrm{T}\alpha_\mathrm{low})^2/2$. This yields:

$$T_1^* = \left(\frac{1}{T_1} + \frac{f_\mathrm{T}^2\alpha_\mathrm{low}^2}{2TR}\right)^{-1}. \tag{5.15}$$

By the substitution:

$$f_\mathrm{T} = \sqrt{T_{1,\mathrm{app}}/T_1}, \tag{5.16}$$

and solving for T_1, a rational expression for T_1 is obtained as follows:

$$T_1 = T_1^*\left(1 + T_{1,\mathrm{app}}\frac{\alpha_\mathrm{low}^2}{2TR}\right). \tag{5.17}$$

Once T_1 has been calculated, f_T can be obtained from Eq. (5.16).

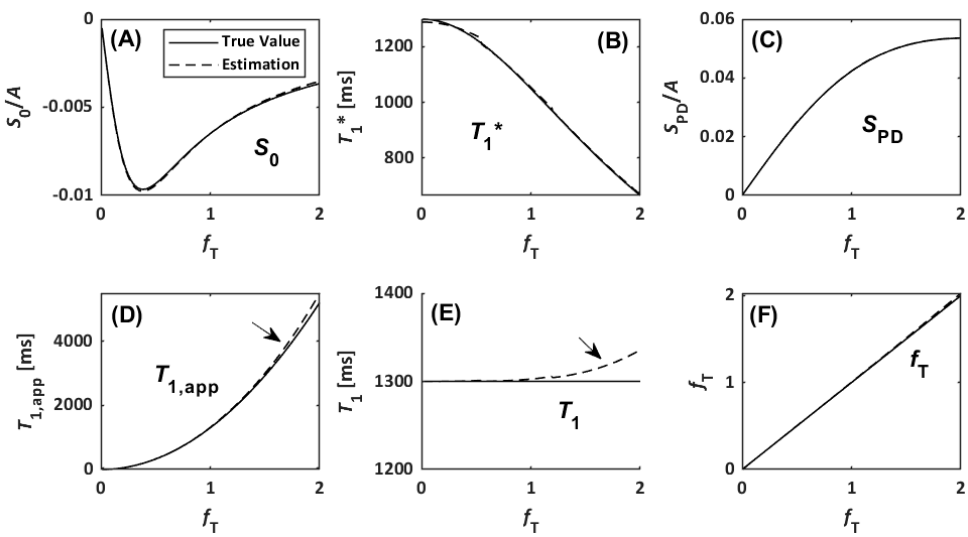

Figure 5.6. Simulation of bias in MP3RAGE, caused by the rational approximation. Deviation in S_0 due to the omission of f_T in Eq. (5.12) is very small (A) and leads to negligible bias in the fitting of T_1* (B) and S_PD (C). Likewise, deviation in T_1* caused by the rational approximation is very small due to both the small α_low = 3° and short TR = 7.45 ms. Due to the higher α_high = 16°, the bias in $T_{1,\mathrm{app}}$ is larger (D). At f_T = 1.7, there is a deviation of +130 ms (arrow) compared to +3 ms for T_1*. This bias is reduced in the estimated T_1 (E) to +13 ms (arrow) and +0.017 in estimated f_T (F). This simulation assumes that the T_1-weighted driven equilibrium has been reached by the end of TC and that f_inv = 0.96 is known.

The rational approximation of Eq. (5.15) is very accurate because of the small $\alpha_{\mathrm{low}} = 3°$ and short $TR = 7.45$ ms (Figure 5.6). The rational approximation of $T_{1,\mathrm{app}}$ is not as accurate due to the higher $\alpha_{\mathrm{high}} = 16°$. This will translate to a small overestimation of estimated T_1 and f_{T} at high B_1^+. It is possible to solve for f_{T} (and thus T_1) numerically without using the rational approximation although this will yield a quite complicated expression considered to be beyond the scope of this text. A flowchart of the MP3RAGE approach can be seen in Figure 5.7.

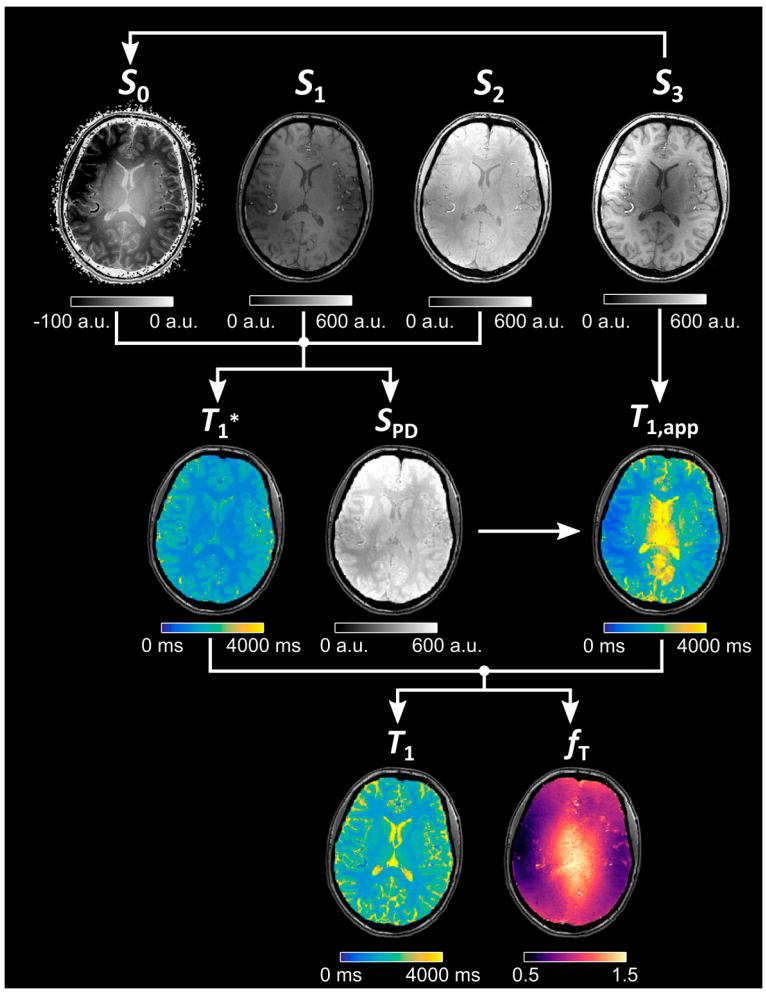

Figure 5.7. Flowchart of the MP3RAGE calculations. Note the lack of contrast in the basal ganglia of the T_1^* map compared to the T_1 map and the high resolution of the flip angle map (f_T).

Phase encoding order

The MP3RAGE cycle contains no period of free relaxation and the three TI values are therefore restricted by the phase encoding order. The encoding order determines where in the RAGE the central k-space line (k_0) is acquired (Figure 5.5). The three Cartesian encoding orders treated here are centric (k_0 acquired in the beginning), linear (k_0 acquired in the middle) and reverse centric (k_0 acquired in the end).

Regarding signal fitting to obtain T_1^* and S_{PD}, the encoding orders of S_1 and S_2 are important to increase precision as the orders determine TI_1 and TI_2. The issue of optimizing precision in an IR experiment with N TI values has been treated by (Ogg & Kingsley, 2004). The longest TI ($TI_{\mathrm{N}-1}$) should be set as close to full relaxation ($5 \times T_1$) as possible (in practice, as long as possible) while the shortest TI (TI_0) should be set as short as possible. The remaining TI values should be geometrically spaced between TI_0 and TI_{N-1} (Labadie, Gounot, Mauss, & Dumitresco, 1994):

$$TI_{\mathrm{n}} = TI_0 + (TI_{\mathrm{N}-1} - TI_0)[(2^n - 1)/(2^{N-1} - 1)]. \tag{5.18}$$

In MP3RAGE, N is limited to 3 and TI_0 is fixed at 0 ms. The value of $TI_2 = TI_{N-1}$ is maximized by a reverse centric order which for $TF \times TR = 7.45{\times}256$ ms (as in the experiments pertaining to Paper V) amounts to 3821 ms. This leaves only $TI_{\mathrm{n}} = TI_1$ left to be determined, and it should then be set as close to 1274 ms as possible. Out of the three encoding orders, a linear order with $TI_1 = 960$ ms yields the closest value ($TI_1 = TI_0$ for centric and $TI_1 = 1914$ ms for reverse centric). The increase in precision was experimentally confirmed in an experiment pertaining to Paper V.

The encoding order of S_3 is only relevant to ensure that M_z is fully in the T_1-weighted driven equilibrium by TI_3. This is essential to reduce bias when calculating $T_{1,\mathrm{app}}$. For the third RAGE, a reverse centric order should thus be chosen. Figure 5.5 depicts the optimal combination of encoding orders, i.e. linear/reverse centric/reverse centric.

Solving for T_1^* and S_{PD} analytically

It is possible to forego the curve fitting of Eq. (5.11) and instead obtain T_1^* and S_{PD} analytically. First, consider the simplest scenario when the three TI values of S_0, S_1 and S_2 are equidistantly spaced by the time constant τ, i.e. $TI_0/TI_1/TI_2 = 0/\tau/2\tau$. This corresponds to a reverse centric (or high-low) phase encoding order of both S_1 and S_2. The signal equation is re-written as:

$$S_{\mathrm{i}} = F - DE^i, \tag{5.19}$$

where $i = 0,1,2$, $E = \exp(-\tau/T_1^*)$, $D = (S_0 - S_{\mathrm{PD}})$, and $F = S_{\mathrm{PD}}$. To eliminate D and F, P is introduced as:

$$P = \frac{S_0 - S_2}{S_0 - S_1} = \frac{(F-D)-\left(F-DE^2\right)}{(F-D)-(F-DE)} = \frac{1-E^2}{1-E} = \frac{(1-E)(1+E)}{(1-E)} = 1 + E, \tag{5.20}$$

which yields:

$$E = \frac{S_0 - S_2 - S_0 - S_1}{S_0 - S_1} = \frac{S_1 - S_2}{S_0 - S_1}. \tag{5.21}$$

Now T_1^* can be solved for in closed form:

$$T_1^* = -\tau/\ln(E). \tag{5.22}$$

Setting up the difference $S_1 - S_0$ yields D as:

$$S_1 - S_0 = D(1 - E) \Rightarrow D = \frac{S_1 - S_0}{1 - E}, \tag{5.23}$$

from which $F = S_{\mathrm{PD}}$ is finally obtained:

$$F = S_0 + D. \tag{5.24}$$

If the TI values are not equidistantly spaced, it becomes necessary to introduce "fictitious" evenly spaced time points on the T_1^* curve, which can be treated algebraically. Consider five points on the T_1^* curve during the 1st and 2nd RAGE trains, all equidistantly spaced with time interval $\tau/2$ (Figure 5.8). Each point represents possible values of TI_1 and TI_2 when using either a centric, linear, or reverse centric phase encoding order. With the new time interval, E becomes $E = \exp\left(-\frac{\tau/2}{T_1^*}\right)$. The signal equation is again re-written as:

$$S_{\mathrm{j}} = F - DE^j, \tag{5.25}$$

where $j = 0,1,2,3,4$. For a linear order of the 1st and 2nd RAGE ($j = 0,1,3$), P becomes:

$$P = \frac{S_0 - S_3}{S_0 - S_1} = \frac{(1 - E)(E^2 + E + 1)}{(1 - E)} = E^2 + E + 1. \tag{5.26}$$

Note that the index of S now denotes j and no longer a particular RAGE train. The positive root of E is obtained from the quadratic formula:

$$E = -1/2 + \sqrt{(1/2)^2 + P - 1}. \tag{5.27}$$

To obtain T_1^*, the correct time interval must be used:

$$T_1^* = -\frac{\tau/2}{\ln(E)}. \tag{5.28}$$

Lastly, D and F are solved for as above (equations (5.23) and (5.24)).

For a linear-reverse centric order ($j = 0,1,4$), solving for E requires finding the roots of the cubic polynomial:

$$P = \frac{S_0 - S_4}{S_0 - S_1} = \frac{1 - E^4}{1 - E} = E^3 + E^2 + E + 1. \tag{5.29}$$

A fully analytical approach would be beneficial compared to signal fitting with regards to processing time. The effect on noise progression has not yet been evaluated, however.

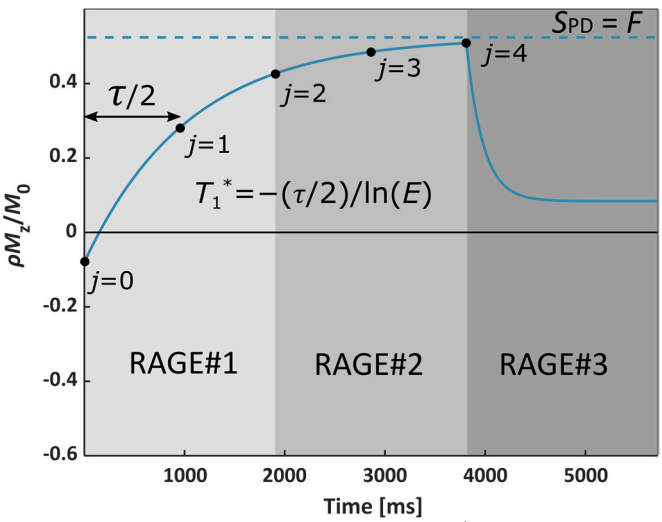

Figure 5.8. Illustration of how to analytically solve for T_1^* and S_{PD} if $TI_0/TI_1/TI_2$ are not equidistantly spaced. Each point on the T_1^* curve during RAGE#1 and RAGE#2 represents possible values of TI_1 and TI_2 using either centric, linear or reverse centric phase encoding order. The points on the T_1* curve during RAGE#1 and RAGE#2 are equidistantly spaced by τ/2 and represent possible values of $TI_0/TI_1/TI_3$ for any combination of the three phase encoding orders. All combinations must have three values of *j*, where the first must be $j = 0$.

High spatial frequency artifacts and the T_1-weighted driven equilibrium

When the third RAGE (S_3) is acquired, there is an initial steep decline in M_z as the magnetization is forced into the T_1-weighted driven equilibrium (cf. Figure 5.5 and 5.8). This leads to a strong weighting of the signal across k-space. If S_3 is acquired with a reverse centric encoding order, it is the high spatial frequencies at the edge of k-space that receive the highest weighting. In the image, this manifests as strong ringing artifacts near the border between the brain and the dura mater. This is basically the opposite effect of the broadening of the PSF typically experienced in MPRAGE imaging. In the experiments pertaining to Paper V, these artifacts were successfully suppressed by an adiabatic saturation pulse, applied immediately before acquisition of S_3 (Figure 5.9). In most of the brain, this prepares M_z so that the distance between the starting point and M_0^* is decreased. The saturation pulse could thus also aid in ensuring that the driven equilibrium is reached. However, if f_T is low, M_0^* will increase by the increased T_1^* (see equations (5.3) and (5.4)). This means that in areas of low f_T and long T_1, the distance between the starting point of M_z and M_0^* could instead be increased by the saturation pulse. How to ensure that the driven equilibrium is reached in the entirety of the brain is still an unresolved issue with the MP3RAGE technique.

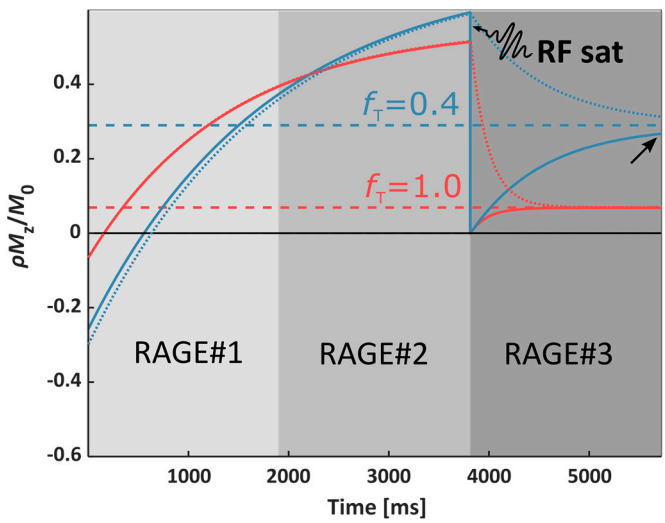

Figure 5.9. An RF saturation pulse is applied prior to RAGE#3. At f_T = 1.0 (red), M_z is prepared much closer to M_0^* (dashed line) compared to when the pulse is not applied (dotted line). This eliminates ringing artifacts in S_3 and the system reaches a driven equilibrium earlier. At low B_1^+ (blue), M_0^* is elevated elevated away from the starting point of M_z when a saturation pulse is applied. Thus, the driven equilibrium is not reached at TI_3 neither with nor without the saturation pulse (arrow). Simulation details: T_1 = 1900 ms, ρ = 0.75 (GM), α_{high} = 16°, TR = 7.45 ms, TF = 256.

Concluding remarks on MP3RAGE

Other uses of the nomenclature "MP3RAGE" exists in the literature (conference abstracts) (Hung, Chen, Chuang, Chang, & Wu, 2013; Rioux, Saranathan, & Rutt, 2014). However, the concept of incorporating a DFA experiment within an MP3RAGE cycle and solving for T_1 and f_T analytically appears to be new. Ideally, the technique should be fully analytical, without the need for a signal fit to acquire T_1^* and S_PD. For Paper V, a signal fit was, however, used to acquire T_1^* and S_PD instead of trying to find the roots of the cubic polynomial in Eq. (5.29), although this should be solvable using the well-established cubic formula (Guilbeau, 1930). Such an approach would make post-processing virtually instantaneous as no co-registration is required. It is possible to obtain T_1 and f_T through a LUT-based approach as with MP2RAGE, and this was shown in a preliminary report (Olsson, Andersen, Kadhim, & Helms, 2021). This method would remove the necessity to force the system into a driven equilibrium by the end of the cycle. The increased dimensionality would, however, increase the processing time dramatically.

It is possible that using a non-adiabatic saturation pulse that scales with f_T would be beneficial, to prepare M_z closer to M_0^* also in low f_T areas, while also avoiding edge enhancement artifacts.

The inherently coregistered flip angle map will be of an unusually high spatial resolution (1 mm isotropic was used in Paper V). Conventionally, flip angle maps are acquired at low spatial resolution, justified by the supposedly smoothly varying B_1 field. However, flip angle mapping based on DREAM, dual *TR* (Yarnykh, 2007), and the Bloch-Siegert shift (Sacolick, Wiesinger, Hancu, & Vogel, 2010), all show elevated B_1^+ estimates in the CSF of the ventricles (Brink, Bornert, Nehrke, & Webb, 2014). Simulations of the electromagnetic field have indicated that this could be caused by the higher electrical conductivity of CSF. The sharp edge at the border between the ventricles and surrounding tissue could thus result in PVEs when a flip angle map of low spatial resolution is used to correct a quantitative map, and the same concern should apply to sulcal CSF close to cortical GM.

The T_1 maps acquired with MP3RAGE show generally higher T_1 estimates compared to the DFA technique, and substantially higher than the MP2RAGE LUT-based approach. This overestimation is larger than expected based on the rational approximation (Figure 5.6) and does not appear to be B_1^+ related (not spatially dependent). The adiabatic inversion pulse should introduce an MT-related bias in the T_1^* calculation as in MP2RAGE (Rioux et al., 2016). However, due to the T_1-weighted driven equilibrium at the end of the cycle, the difference in magnetization between the free and the bound pool ($M_{0\mathrm{b}}/M_{0\mathrm{f}} - M_{\mathrm{zb}}/M_{\mathrm{zf}}$) should be considerably less than in MP2RAGE. The MP3RAGE technique should thus be less sensitive to incidental MT effects than MP2RAGE, albeit more sensitive than DFA.

6 – Concluding remarks

The work presented in this thesis has aimed at implementing existing and novel qMRI techniques and optimizing them for 7T-specific conditions. Efforts have been made to identify and correct biases in derived parameter maps, as well as forming an understanding of the underlying physical origin of these biases. The strong inhomogeneity of the B_1 field at 7T is the primary source of bias and well-established techniques such as MPM requires more care to control or exclude different biases compared to 3T. On this note, it would be interesting to evaluate the performance of the MP3RAGE technique at 3T, as the reduced B_1^+ inhomogeneity would allow to more reliable reach the driven equilibrium across the whole brain. Similarly, the performance of MP3RAGE using a more advanced parallel transmit array at 7T would also be interesting to explore.

The scope of this thesis has been rather broad, as the parameter mapping has focused on both T_1, MT_{sat}, and the local flip angle (Figure 6.1). Regarding pulse sequences, they have ranged from the standard spoiled GRE, to variations of the MPRAGE sequence, to the STEAM-prepared DREAM sequence. A common theme amongst the pulse sequence protocols treated here is that they can all be considered to be rather fast, which is a critical aspect for any clinical application. More research regarding the variability of especially T_1-mapping techniques is needed. This statement is valid not only for the techniques used in this thesis and for UHF, but for T_1-mapping in general, as noted by Stikov et al. (2015). It is my personal hope that the findings presented in this thesis can be useful to other researchers pursuing increased robustness and reproducibility within the qMRI field.

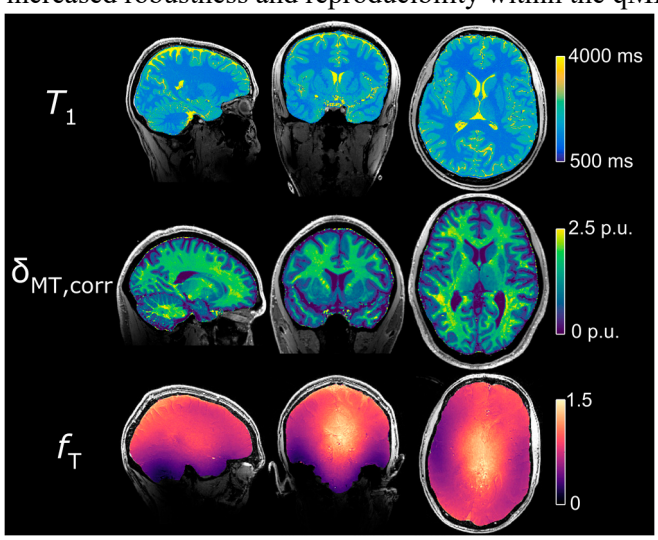

Figure 6.1. Maps of the three main parameters in this thesis: The longitudinal relaxation time (T_1), the magnetization transfer saturation ($\delta_{MT,corr}$), and the local flip angle (f_T).

Acknowledgements

I would like to thank my main supervisor, Gunther Helms. His tireless efforts trying to turn me into an MR physicist far exceeds what can reasonably be expected from a PhD supervisor. I feel privileged to have had such a knowledgeable and distinguished scientist as a mentor during these five years.

I would like to thank my co-supervisors, Ronnie Wirestam and Mads Andersen. Ronnie Wirestam was responsible for sparking my initial interest in the field of MRI and has guided me through both my undergraduate and postgraduate studies with his excellent teaching abilities and calming presence. Mads Andersen became my co-supervisor halfway through my doctoral studies and has since then been an indispensable resource of knowledge regarding the 7T system and more, always helpful and of a practical mindset.

I would like to thank my other co-authors, Jimmy Lätt, Mustafa Kadhim and Mikael Novén. I enjoyed working with all of you and would love to do so again.

I would like to thank the staff at the Swedish 7T facility for all their help with practical issues and their always friendly attitude. Likewise, the MR-physics group and the department of Medical Radiation Physics deserves thanks. I regret not seeing more of all of you because of the pandemic.

I would like to thank every person that has ever taken time of their day to act as a volunteer in the scanner. This thesis would literally not have been possible without you. You may multiply my thanks by the number of times you volunteered.

Thanks to my friends that have supported me through these years, each in in their own way. Special thanks to Robin Kämpe for initially suggesting me to pursue a PhD.

A huge thank you to my mom, dad and sister for your love and support and for practically raising my kids during these final months.

Thank you to Ebba and Fabian for contrasting magnetization transfer and RF inhomogeneities with monster trucks and princesses. You bring me endless joy.

Finally, a heartfelt thank you to my fiancée Chia-Yen (Juno) Hsu. Thank you for sticking by me and pushing me forward through all these years and for all the sacrifices you have made to do so. 我愛你.

References

A. G. Teixeira, R. P., Neji, R., Wood, T. C., Baburamani, A. A., Malik, S. J., & Hajnal, J. V. (2020). Controlled saturation magnetization transfer for reproducible multivendor variable flip angle T1 and T2 mapping. *Magn Reson Med, 84*(1), 221-236. doi:10.1002/mrm.28109

Acosta-Cabronero, J., Milovic, C., Mattern, H., Tejos, C., Speck, O., & Callaghan, M. F. (2018). A robust multi-scale approach to quantitative susceptibility mapping. *Neuroimage, 183*, 7-24. doi:10.1016/j.neuroimage.2018.07.065

Ashburner, J., & Friston, K. J. (2005). Unified segmentation. *Neuroimage, 26*(3), 839-851. doi:10.1016/j.neuroimage.2005.02.018

Balchandani, P., & Naidich, T. P. (2015). Ultra-High-Field MR Neuroimaging. *AJNR Am J Neuroradiol, 36*(7), 1204-1215. doi:10.3174/ajnr.A4180

Barisano, G., Sepehrband, F., Ma, S., Jann, K., Cabeen, R., Wang, D. J., . . . Law, M. (2019). Clinical 7 T MRI: Are we there yet? A review about magnetic resonance imaging at ultra-high field. *Br J Radiol, 92*(1094), 20180492. doi:10.1259/bjr.20180492

Baudrexel, S., Noth, U., Schure, J. R., & Deichmann, R. (2018). T1 mapping with the variable flip angle technique: A simple correction for insufficient spoiling of transverse magnetization. *Magn Reson Med, 79*(6), 3082-3092. doi:10.1002/mrm.26979

Baudrexel, S., Nurnberger, L., Rub, U., Seifried, C., Klein, J. C., Deller, T., . . . Hilker, R. (2010). Quantitative mapping of T1 and T2* discloses nigral and brainstem pathology in early Parkinson's disease. *Neuroimage, 51*(2), 512-520. doi:10.1016/j.neuroimage.2010.03.005

Bloch, F. (1946). Nuclear Induction. *Physical Review, 70*(7-8), 460-474. doi:10.1103/PhysRev.70.460

Bottomley, P. A., Foster, T. H., Argersinger, R. E., & Pfeifer, L. M. (1984). A review of normal tissue hydrogen NMR relaxation times and relaxation mechanisms from 1-100 MHz: dependence on tissue type, NMR frequency, temperature, species, excision, and age. *Medical physics, 11*(4), 425–448. doi:https://doi.org/10.1118/1.595535

Brink, W. M., Bornert, P., Nehrke, K., & Webb, A. G. (2014). Ventricular B1 (+) perturbation at 7 T - real effect or measurement artifact? *NMR Biomed, 27*(6), 617-620. doi:10.1002/nbm.3112

Busse, R. F., Brau, A. C., Vu, A., Michelich, C. R., Bayram, E., Kijowski, R., Reeder, S. B., & Rowley, H. A. (2008). Effects of refocusing flip angle modulation and view ordering in 3D fast spin echo. *Magnetic resonance in medicine*, *60*(3), 640–649. https://doi.org/10.1002/mrm.21680

Callaghan, M. F., Helms, G., Lutti, A., Mohammadi, S., & Weiskopf, N. (2015). A general linear relaxometry model of R1 using imaging data. *Magn Reson Med, 73*(3), 1309-1314. doi:10.1002/mrm.25210

Christensen, K. A., Grant, D. M., Schulman, E. M., & Walling, C. (1974). Optimal determination of relaxation times of fourier transform nuclear magnetic resonance. Determination of spin-lattice relaxation times in chemically polarized species. *The Journal of Physical Chemistry, 78*(19), 1971-1977. doi:10.1021/j100612a022

Corbin, N., & Callaghan, M. F. (2021). Imperfect spoiling in variable flip angle T1 mapping at 7T: Quantifying and minimizing impact. *Magn Reson Med, 86*(2), 693-708. doi:10.1002/mrm.28720

Crawley, A. P., Wood, M. L., & Henkelman, R. M. (1988). Elimination of transverse coherences in FLASH MRI. *Magn Reson Med, 8*(3), 248-260. doi:10.1002/mrm.1910080303

Dathe, H., & Helms, G. (2010). Exact algebraization of the signal equation of spoiled gradient echo MRI. *Phys Med Biol, 55*(15), 4231-4245. doi:10.1088/0031-9155/55/15/003

Davies, G. R., Hadjiprocopis, A., Altmann, D. R., Chard, D. T., Griffin, C. M., Rashid, W., Parker, G. J., Tofts, P. S., Kapoor, R., Thompson, A. J., & Miller, D. H. (2007). Normal-appearing grey and white matter T1 abnormality in early relapsing-remitting multiple sclerosis: a longitudinal study. *Multiple sclerosis (Houndmills, Basingstoke, England)*, *13*(2), 169–177. https://doi.org/10.1177/1352458506070726

de Graaf RA. *In vivo NMR Spectroscopy: Principles and Techniques*. 3rd ed. Hoboken, NJ: John Wiley & Sons Ltd; 2018. https ://www.wiley.com/en-us/In+Vivo+NMR+Spectroscopy%3A+Principles+and+Techniques %2C+3rd+Edition-p-9781119382515. Acessed September 19, 2021.

De Stefano N, Battaglini M, Stromillo ML, et al. Brain damage as detected by magnetization transfer imaging is less pronounced in benign than in early relapsing multiple sclerosis. Brain : a Journal of Neurology. 2006 Aug;129(Pt 8):2008-2016. DOI: 10.1093/brain/awl152. PMID: 16815879.

Deichmann, R., Good, C. D., Josephs, O., Ashburner, J., & Turner, R. (2000). Optimization of 3-D MP-RAGE sequences for structural brain imaging. *Neuroimage, 12*(1), 112-127. doi:10.1006/nimg.2000.0601

Deichmann, R., & Haase, A. (1992). Quantification of T1 values by SNAPSHOT-FLASH NMR imaging. *Journal of Magnetic Resonance (1969), 96*(3), 608-612. doi:https://doi.org/10.1016/0022-2364(92)90347-A

Deoni, S. C., Rutt, B. K., & Peters, T. M. (2003). Rapid combined T1 and T2 mapping using gradient recalled acquisition in the steady state. *Magn Reson Med, 49*(3), 515-526. doi:10.1002/mrm.10407

Dexter, D. T., Jenner, P., Schapira, A. H., & Marsden, C. D. (1992). Alterations in levels of iron, ferritin, and other trace metals in neurodegenerative diseases affecting the basal ganglia. The Royal Kings and Queens Parkinson's Disease Research Group. *Ann Neurol, 32 Suppl*, S94-100. doi:10.1002/ana.410320716

Dousset, V., Grossman, R. I., Ramer, K. N., Schnall, M. D., Young, L. H., Gonzalez-Scarano, F., Lavi, E., & Cohen, J. A. (1992). Experimental allergic encephalomyelitis and multiple sclerosis: lesion characterization with magnetization transfer imaging. *Radiology*, *182*(2), 483–491. https://doi.org/10.1148/radiology.182.2.1732968

Duyn, J. H. (2012). The future of ultra-high field MRI and fMRI for study of the human brain. *Neuroimage, 62*(2), 1241-1248. doi:10.1016/j.neuroimage.2011.10.065

Ernst, R. R., & Anderson, W. A. (1966). Application of Fourier Transform Spectroscopy to Magnetic Resonance. *Review of Scientific Instruments, 37*, 93-102.

Feinberg, D. A., Hale, J. D., Watts, J. C., Kaufman, L., & Mark, A. (1986). Halving MR imaging time by conjugation: demonstration at 3.5 kG. *Radiology, 161*(2), 527-531. doi:10.1148/radiology.161.2.3763926

Filippi, M., & Agosta, F. (2007). Magnetization transfer MRI in multiple sclerosis. *J Neuroimaging, 17 Suppl 1*, 22S-26S. doi:10.1111/j.1552-6569.2007.00132.x

Frahm, J., Merboldt, K. D., Hänicke, W., & Haase, A. (1985). Stimulated echo imaging. *Journal of Magnetic Resonance (1969), 64*(1), 81-93. doi:https://doi.org/10.1016/0022-2364(85)90033-2

Ganter, C. (2006). Steady state of gradient echo sequences with radiofrequency phase cycling: analytical solution, contrast enhancement with partial spoiling. *Magn Reson Med, 55*(1), 98-107. doi:10.1002/mrm.20736

Grad, J., & Bryant, R. G. (1990). Nuclear magnetic cross-relaxation spectroscopy. *Journal of Magnetic Resonance, 90*, 1-8. doi:10.1016/0022-2364(90)90361-C

Graham, S. J., & Henkelman, R. M. (1997). Understanding pulsed magnetization transfer. *J Magn Reson Imaging, 7*(5), 903-912. doi:10.1002/jmri.1880070520

Griffin, C. M., Dehmeshki, J., Chard, D. T., Parker, G. J., Barker, G. J., Thompson, A. J., & Miller, D. H. (2002). T1 histograms of normal-appearing brain tissue are abnormal in early relapsing-remitting multiple sclerosis. *Mult Scler, 8*(3), 211-216. doi:10.1191/1352458502ms807oa

Guilbeau, L. (1930). The History of the Solution of the Cubic Equation. *Mathematics News Letter, 5*(4), 8-12. doi:10.2307/3027812

Haase, A., Frahm, J., Matthaei, D., Hanicke, W., & Merboldt, K. D. (1986). FLASH imaging. Rapid NMR imaging using low flip-angle pulses. *Journal of Magnetic Resonance (1969), 67*(2), 258-266. doi:https://doi.org/10.1016/0022-2364(86)90433-6

Hagberg, G. E., Bause, J., Ethofer, T., Ehses, P., Dresler, T., Herbert, C., Pohmann, R., Shajan, G., Fallgatter, A., Pavlova, M. A., & Scheffler, K. (2017). Whole brain MP2RAGE-based mapping of the longitudinal relaxation time at 9.4T. *NeuroImage*, *144*(Pt A), 203–216. https://doi.org/10.1016/j.neuroimage.2016.09.047

Hajnal, J. V., Baudouin, C. J., Oatridge, A., Young, I. R., & Bydder, G. M. (1992). Design and implementation of magnetization transfer pulse sequences for clinical use. *J Comput Assist Tomogr, 16*(1), 7-18. doi:10.1097/00004728-199201000-00003

Helms, G. (2015). *Correction for residual effects of B1+ inhomogeneity on MT saturation in FLASH-based multi-parameter mapping of the brain.* In proceedings of the the 23rd Annual Meeting of ISMRM, Toronto, Ontario.Abstract 3360

Helms, G. (2021). *A simple approach to control rms(B1) by pulse length in variable flip angle (VFA).* In proceedings of the 2021 ISMRM Annual Meeting & Exhibition, virtual meeting. Abstract 3073

Helms, G., Dathe, H., & Dechent, P. (2008). Quantitative FLASH MRI at 3T using a rational approximation of the Ernst equation. *Magn Reson Med, 59*(3), 667-672. doi:10.1002/mrm.21542

Helms, G., Dathe, H., Kallenberg, K., & Dechent, P. (2008). High-resolution maps of magnetization transfer with inherent correction for RF inhomogeneity and T1 relaxation obtained from 3D FLASH MRI. *Magn Reson Med, 60*(6), 1396-1407. doi:10.1002/mrm.21732

Helms, G., Dathe, H., Weiskopf, N., & Dechent, P. (2011). Identification of signal bias in the variable flip angle method by linear display of the algebraic Ernst equation. *Magn Reson Med, 66*(3), 669-677. doi:10.1002/mrm.22849

Helms, G., & Dechent, P. (2009). Increased SNR and reduced distortions by averaging multiple gradient echo signals in 3D FLASH imaging of the human brain at 3T. *J Magn Reson Imaging, 29*(1), 198-204. doi:10.1002/jmri.21629

Helms, G., Draganski, B., Frackowiak, R., Ashburner, J., & Weiskopf, N. (2009). Improved segmentation of deep brain grey matter structures using magnetization transfer (MT) parameter maps. *Neuroimage, 47*(1), 194-198. doi:10.1016/j.neuroimage.2009.03.053

Helms, G., & Hagberg, G. E. (2004). Pulsed saturation of the standard two-pool model for magnetization transfer. Part I: The steady state. *Concepts in Magnetic Resonance Part A, 21A*(1), 37-49. doi:https://doi.org/10.1002/cmr.a.20004

Helms, G., & Hagberg, G. E. (2009). In vivo quantification of the bound pool T1 in human white matter using the binary spin-bath model of progressive magnetization transfer saturation. *Phys Med Biol, 54*(23), N529-540. doi:10.1088/0031-9155/54/23/N01

Helms, G., Lätt, J., & Olsson, H. (2020). Cross-vendor transfer and RF coil comparison of high-resolution MP2RAGE protocol for brain imaging at 7T. *Acta Scientiarum Lundensia, 2020*(001), 1-12.

Helms, G., & Piringer, A. (2005). Simultaneous measurement of saturation and relaxation in human brain by repetitive magnetization transfer pulses. *NMR Biomed, 18*(1), 44-50. doi:10.1002/nbm.920

Henkelman, R. M., Huang, X., Xiang, Q. S., Stanisz, G. J., Swanson, S. D., & Bronskill, M. J. (1993). Quantitative interpretation of magnetization transfer. *Magn Reson Med, 29*(6), 759-766. doi:10.1002/mrm.1910290607

Henkelman, R. M., Stanisz, G. J., & Graham, S. J. (2001). Magnetization transfer in MRI: a review. *NMR Biomed, 14*(2), 57-64. doi:10.1002/nbm.683

Hennig, J., Nauerth, A., & Friedburg, H. (1986). RARE imaging: a fast imaging method for clinical MR. *Magn Reson Med, 3*(6), 823-833. doi:10.1002/mrm.1910030602

Hinks, R. S., & Constable, R. T. (1994). Gradient moment nulling in fast spin echo. *Magn Reson Med, 32*(6), 698-706. doi:10.1002/mrm.1910320604

Homer, J., & Beevers, M. S. (1985). Driven-equilibrium single-pulse observation of T1 relaxation. A reevaluation of a rapid "new" method for determining NMR spin-lattice relaxation times. *Journal of Magnetic Resonance (1969), 63*(2), 287-297. doi:https://doi.org/10.1016/0022-2364(85)90318-X

Hoult, D. I. (2000). The principle of reciprocity in signal strength calculations—A mathematical guide. *Concepts in Magnetic Resonance, 12*(4), 173-187. doi:https://doi.org/10.1002/1099-0534(2000)12:4<173::AID-CMR1>3.0.CO;2-Q

Hoult, D. I., & Richards, R. E. (1976). The signal-to-noise ratio of the nuclear magnetic resonance experiment. *Journal of Magnetic Resonance (1969), 24*(1), 71-85. doi:https://doi.org/10.1016/0022-2364(76)90233-X

Hua, J., Jones, C. K., Blakeley, J., Smith, S. A., van Zijl, P. C., & Zhou, J. (2007). Quantitative description of the asymmetry in magnetization transfer effects around the water resonance in the human brain. *Magn Reson Med, 58*(4), 786-793. doi:10.1002/mrm.21387

Hung, W., Chen, P., Chuang, T., Chang, H., & Wu, M. (2013, 20-26 April). *High resolution volumetric T1 mapping using a novel MP3RAGE method.* In proceedings of the 21st Annual Meeting of ISMRM, Salt Lake City, Utah. Abstract 2353

Hurley, A. C., Al-Radaideh, A., Bai, L., Aickelin, U., Coxon, R., Glover, P., & Gowland, P. A. (2010). Tailored RF pulse for magnetization inversion at ultrahigh field. *Magn Reson Med, 63*(1), 51-58. doi:10.1002/mrm.22167

Ilott, A. J., & Jerschow, A. (2018). Aspects of NMR reciprocity and applications in highly conductive media. *Concepts in Magnetic Resonance Part A: Bridging Education and Research, 47A*(2), e21466. doi:https://doi.org/10.1002/cmr.a.21466

Janve, V. A., Zu, Z., Yao, S. Y., Li, K., Zhang, F. L., Wilson, K. J., . . . Gochberg, D. F. (2013). The radial diffusivity and magnetization transfer pool size ratio are sensitive markers for demyelination in a rat model of type III multiple sclerosis (MS) lesions. *Neuroimage, 74*, 298-305. doi:10.1016/j.neuroimage.2013.02.034

Juchem, C., & de Graaf, R. A. (2017). B0 magnetic field homogeneity and shimming for in vivo magnetic resonance spectroscopy. *Anal Biochem, 529*, 17-29. doi:10.1016/j.ab.2016.06.003

Kaldoudi, E., Williams, S. C., Barker, G. J., & Tofts, P. S. (1993). A chemical shift selective inversion recovery sequence for fat-suppressed MRI: theory and experimental validation. *Magn Reson Imaging, 11*(3), 341-355. doi:10.1016/0730-725x(93)90067-n

Kamagata, K., Zalesky, A., Yokoyama, K. *et al.* MR g-ratio-weighted connectome analysis in patients with multiple sclerosis. *Sci Rep* **9,** 13522 (2019). https://doi.org/10.1038/s41598-019-50025-2

Kessler, L. G., Barnhart, H. X., Buckler, A. J., Choudhury, K. R., Kondratovich, M. V., Toledano, A., Guimaraes, A. R., Filice, R., Zhang, Z., Sullivan, D. C., & QIBA Terminology Working Group (2015). The emerging science of quantitative imaging biomarkers terminology and definitions for scientific studies and regulatory submissions. *Statistical methods in medical research*, *24*(1), 9–26. https://doi.org/10.1177/0962280214537333

Kingsley, P. B., & Monahan, W. G. (2001). Effect of increased repetition time TR on precision of inversion-recovery T(1) measurements. *Magn Reson Imaging, 19*(2), 279-282. doi:10.1016/s0730-725x(01)00294-6

Labadie, C., Gounot, D., Mauss, Y., & Dumitresco, B. (1994). Data sampling in MRI relaxation. *Magnetic Resonance Materials in Physics, Biology, and Medicine, 2*, 383-385. doi:10.1007/BF01705278

Langkammer, C., Pirpamer, L., Seiler, S., Deistung, A., Schweser, F., Franthal, S., . . . Schwingenschuh, P. (2016). Quantitative Susceptibility Mapping in Parkinson's Disease. *PLoS One, 11*(9), e0162460. doi:10.1371/journal.pone.0162460

Larkman, D. J., & Nunes, R. G. (2007). Parallel magnetic resonance imaging. *Phys Med Biol, 52*(7), R15-55. doi:10.1088/0031-9155/52/7/R01

Lee, Y., Callaghan, M. F., & Nagy, Z. (2017). Analysis of the Precision of Variable Flip Angle T1 Mapping with Emphasis on the Noise Propagated from RF Transmit Field Maps. *Front Neurosci, 11*, 106. doi:10.3389/fnins.2017.00106

Lescher, S., Jurcoane, A., Veit, A., Bahr, O., Deichmann, R., & Hattingen, E. (2015). Quantitative T1 and T2 mapping in recurrent glioblastomas under bevacizumab: earlier detection of tumor progression compared to conventional MRI. *Neuroradiology, 57*(1), 11-20. doi:10.1007/s00234-014-1445-9

Li, J. G., Graham, S. J., & Henkelman, R. M. (1997). A flexible magnetization transfer line shape derived from tissue experimental data. *Magn Reson Med, 37*(6), 866-871. doi:10.1002/mrm.1910370610

Liu, J., Liu, T., de Rochefort, L., Ledoux, J., Khalidov, I., Chen, W., Tsiouris, A. J., Wisnieff, C., Spincemaille, P., Prince, M. R., & Wang, Y. (2012). Morphology enabled dipole inversion for quantitative susceptibility mapping using structural consistency between the magnitude image and the susceptibility map. *NeuroImage*, *59*(3), 2560–2568. https://doi.org/10.1016/j.neuroimage.2011.08.082

Loureiro JR, Himmelbach M, Ethofer T, et al. In-vivo quantitative structural imaging of the human midbrain and the superior colliculus at 9.4T.

Neuroimage. 2018 Aug;177:117-128. DOI: 10.1016/j.neuroimage.2018.04.071. PMID: 29729391.
Lutti, A., Dick, F., Sereno, M. I., & Weiskopf, N. (2014). Using high-resolution quantitative mapping of R1 as an index of cortical myelination. *Neuroimage, 93 Pt 2*, 176-188. doi:10.1016/j.neuroimage.2013.06.005
Marques, J. P., & Gruetter, R. (2013). New developments and applications of the MP2RAGE sequence--focusing the contrast and high spatial resolution R1 mapping. *PLoS One, 8*(7), e69294. doi:10.1371/journal.pone.0069294
Marques, J. P., Kober, T., Krueger, G., van der Zwaag, W., Van de Moortele, P. F., & Gruetter, R. (2010). MP2RAGE, a self bias-field corrected sequence for improved segmentation and T1-mapping at high field. *Neuroimage, 49*(2), 1271-1281. doi:10.1016/j.neuroimage.2009.10.002
McConnell, H. (1958). Reaction Rates by Nuclear Magnetic Resonance. *Journal of Chemical Physics, 28*, 430-431.
Morrison, C., & Henkelman, R. M. (1995). A model for magnetization transfer in tissues. *Magn Reson Med, 33*(4), 475-482. doi:10.1002/mrm.1910330404
Mugler, J. P., 3rd, & Brookeman, J. R. (1990). Three-dimensional magnetization-prepared rapid gradient-echo imaging (3D MP RAGE). *Magn Reson Med, 15*(1), 152-157. doi:10.1002/mrm.1910150117
Mugler, J. P., 3rd, & Brookeman, J. R. (1991). Rapid three-dimensional T1-weighted MR imaging with the MP-RAGE sequence. *J Magn Reson Imaging, 1*(5), 561-567. doi:10.1002/jmri.1880010509
Nehrke, K., & Bornert, P. (2012). DREAM--a novel approach for robust, ultrafast, multislice B(1) mapping. *Magn Reson Med, 68*(5), 1517-1526. doi:10.1002/mrm.24158
Nurnberger, L., Gracien, R. M., Hok, P., Hof, S. M., Rub, U., Steinmetz, H., . . . Baudrexel, S. (2017). Longitudinal changes of cortical microstructure in Parkinson's disease assessed with T1 relaxometry. *Neuroimage Clin, 13*, 405-414. doi:10.1016/j.nicl.2016.12.025
Ogg, R. J., & Kingsley, P. B. (2004). Optimized precision of inversion-recovery T1 measurements for constrained scan time. *Magn Reson Med, 51*(3), 625-630. doi:10.1002/mrm.10734
Olsson, H., Andersen, M., Kadhim, M., & Helms, G. *Simultaneous 3D T1 and B1+ mapping at 7T using MPRAGE with multiple volumes and driven equilibrium.* In proceedings of the 2021 ISMRM Annual Meeting & Exhibition, virtual meeting. Abstract 0550
Oros-Peusquens, A. M., Laurila, M., & Shah, N. J. (2008). Magnetic field dependence of the distribution of NMR relaxation times in the living human brain. *MAGMA, 21*(1-2), 131-147. doi:10.1007/s10334-008-0107-5
Ou, X., & Gochberg, D. F. (2008). MT effects and T1 quantification in single-slice spoiled gradient echo imaging. *Magn Reson Med, 59*(4), 835-845. doi:10.1002/mrm.21550
Peters, A. M., Brookes, M. J., Hoogenraad, F. G., Gowland, P. A., Francis, S. T., Morris, P. G., & Bowtell, R. (2007). T2* measurements in human brain at

1.5, 3 and 7 T. *Magn Reson Imaging, 25*(6), 748-753. doi:10.1016/j.mri.2007.02.014

Pike, G. B. (1996). Pulsed magnetization transfer contrast in gradient echo imaging: a two-pool analytic description of signal response. *Magn Reson Med, 36*(1), 95-103. doi:10.1002/mrm.1910360117

Pohmann, R., Shajan, G., & Balla, D. Z. (2011). Contrast at high field: relaxation times, magnetization transfer and phase in the rat brain at 16.4 T. *Magn Reson Med, 66*(6), 1572-1581. doi:10.1002/mrm.22949

Pohmann, R., Speck, O., & Scheffler, K. (2016). Signal-to-noise ratio and MR tissue parameters in human brain imaging at 3, 7, and 9.4 tesla using current receive coil arrays. *Magn Reson Med, 75*(2), 801-809. doi:10.1002/mrm.25677

Preibisch, C., & Deichmann, R. (2009). Influence of RF spoiling on the stability and accuracy of T1 mapping based on spoiled FLASH with varying flip angles. *Magn Reson Med, 61*(1), 125-135. doi:10.1002/mrm.21776

Pruessmann, K. P., Weiger, M., Scheidegger, M. B., & Boesiger, P. (1999). SENSE: sensitivity encoding for fast MRI. *Magn Reson Med, 42*(5), 952-962.

Reynolds, L., Morris, S. R., Vavasour, I. M., Barlow, L., Laule, C., MacKay, A. L., & Michal, C. A. (2021). *T1 Relaxation of White Matter Following Adiabatic Inversion.* In proceedings of ISMRM 29th Annual Meeting & Exhibition, Virtual meeting

Rioux, J. A., Levesque, I. R., & Rutt, B. K. (2016). Biexponential longitudinal relaxation in white matter: Characterization and impact on T1 mapping with IR-FSE and MP2RAGE. *Magn Reson Med, 75*(6), 2265-2277. doi:10.1002/mrm.25729

Rioux, J. A., Saranathan, M., & Rutt, B. K. (2014, 10-16 May). *Simultaneous Whole-Brain T1 and Flip Angle Mapping with MP3RAGE.* In proceedings of the 22nd Annual meeting of ISMRM, Milan. Abstract 3216

Robinson, S. D., Bredies, K., Khabipova, D., Dymerska, B., Marques, J. P., & Schweser, F. (2017). An illustrated comparison of processing methods for MR phase imaging and QSM: combining array coil signals and phase unwrapping. *NMR Biomed, 30*(4). doi:10.1002/nbm.3601

Roemer, P. B., Edelstein, W. A., Hayes, C. E., Souza, S. P., & Mueller, O. M. (1990). The NMR phased array. *Magn Reson Med, 16*(2), 192-225. doi:10.1002/mrm.1910160203

Rooney, W. D., Johnson, G., Li, X., Cohen, E. R., Kim, S. G., Ugurbil, K., & Springer, C. S., Jr. (2007). Magnetic field and tissue dependencies of human brain longitudinal 1H2O relaxation in vivo. *Magn Reson Med, 57*(2), 308-318. doi:10.1002/mrm.21122

Sacolick, L. I., Wiesinger, F., Hancu, I., & Vogel, M. W. (2010). B1 mapping by Bloch-Siegert shift. *Magn Reson Med, 63*(5), 1315-1322. doi:10.1002/mrm.22357

Schenck, J. F., & Zimmerman, E. A. (2004). High-field magnetic resonance imaging of brain iron: birth of a biomarker? *NMR Biomed, 17*(7), 433-445. doi:10.1002/nbm.922

Sled, J. G., & Pike, G. B. (2000). Quantitative interpretation of magnetization transfer in spoiled gradient echo MRI sequences. *J Magn Reson, 145*(1), 24-36. doi:10.1006/jmre.2000.2059

Sled, J. G., & Pike, G. B. (2001). Quantitative imaging of magnetization transfer exchange and relaxation properties in vivo using MRI. *Magn Reson Med, 46*(5), 923-931. doi:10.1002/mrm.1278

Stehling, M. K., Ordidge, R. J., Coxon, R., & Mansfield, P. (1990). Inversion-recovery echo-planar imaging (IR-EPI) at 0.5 T. *Magn Reson Med, 13*(3), 514-517. doi:10.1002/mrm.1910130320

Stikov, N., Boudreau, M., Levesque, I. R., Tardif, C. L., Barral, J. K., & Pike, G. B. (2015). On the accuracy of T1 mapping: searching for common ground. *Magn Reson Med, 73*(2), 514-522. doi:10.1002/mrm.25135

Stockmann, J. P., & Wald, L. L. (2018). In vivo B0 field shimming methods for MRI at 7T. *Neuroimage, 168*, 71-87. doi:10.1016/j.neuroimage.2017.06.013

Tabelow, K., Balteau, E., Ashburner, J., Callaghan, M. F., Draganski, B., Helms, G., . . . Mohammadi, S. (2019). hMRI - A toolbox for quantitative MRI in neuroscience and clinical research. *Neuroimage, 194*, 191-210. doi:10.1016/j.neuroimage.2019.01.029

Ugurbil, K., Adriany, G., Andersen, P., Chen, W., Garwood, M., Gruetter, R., . . . Zhu, X. H. (2003). Ultrahigh field magnetic resonance imaging and spectroscopy. *Magn Reson Imaging, 21*(10), 1263-1281. doi:10.1016/j.mri.2003.08.027

Van de Moortele, P. F., Auerbach, E. J., Olman, C., Yacoub, E., Ugurbil, K., & Moeller, S. (2009). T1 weighted brain images at 7 Tesla unbiased for Proton Density, T2* contrast and RF coil receive B1 sensitivity with simultaneous vessel visualization. *Neuroimage, 46*(2), 432-446. doi:10.1016/j.neuroimage.2009.02.009

van Gelderen, P., Koretsy, A. P., de Zwart, J. A., & Duyn, J. H. (2006). *A simple B1 correction method for high resolution neuroimaging.* Presented at the 14th Scientific Meeting ISMRM, Seattle, WA.

van Zijl, P. C. M., Lam, W. W., Xu, J., Knutsson, L., & Stanisz, G. J. (2018). Magnetization Transfer Contrast and Chemical Exchange Saturation Transfer MRI. Features and analysis of the field-dependent saturation spectrum. *Neuroimage, 168*, 222-241. doi:10.1016/j.neuroimage.2017.04.045

Vaughan, J. T., Garwood, M., Collins, C. M., Liu, W., DelaBarre, L., Adriany, G., . . . Ugurbil, K. (2001). 7T vs. 4T: RF power, homogeneity, and signal-to-noise comparison in head images. *Magn Reson Med, 46*(1), 24-30. doi:10.1002/mrm.1156

Weigel, M. (2015). Extended phase graphs: dephasing, RF pulses, and echoes - pure and simple. *J Magn Reson Imaging, 41*(2), 266-295. doi:10.1002/jmri.24619

Weiskopf, N., Callaghan, M. F., Josephs, O., Lutti, A., & Mohammadi, S. (2014). Estimating the apparent transverse relaxation time (R2(*)) from images

with different contrasts (ESTATICS) reduces motion artifacts. *Front Neurosci, 8*, 278. doi:10.3389/fnins.2014.00278

Weiskopf, N., Edwards, L. J., Helms, G., Mohammadi, S., & Kirilina, E. (2021). Quantitative magnetic resonance imaging of brain anatomy and in vivo histology. *Nature Reviews Physics, 3*(8), 570-588. doi:10.1038/s42254-021-00326-1

Weiskopf, N., Suckling, J., Williams, G., Correia, M. M., Inkster, B., Tait, R., . . . Lutti, A. (2013). Quantitative multi-parameter mapping of R1, PD(*), MT, and R2(*) at 3T: a multi-center validation. *Front Neurosci, 7*, 95. doi:10.3389/fnins.2013.00095

Wennerström, H. (1973). Proton nuclear magnetic resonance lineshapes in lamellar liquid crystals. *Chemical Physics Letters, 18*(1), 41-44. doi:https://doi.org/10.1016/0009-2614(73)80333-1

Wiesinger, F., Van de Moortele, P. F., Adriany, G., De Zanche, N., Ugurbil, K., & Pruessmann, K. P. (2004). Parallel imaging performance as a function of field strength--an experimental investigation using electrodynamic scaling. *Magn Reson Med, 52*(5), 953-964. doi:10.1002/mrm.20281

Wiggermann, V., MacKay, A. L., Rauscher, A., & Helms, G. (2021). In vivo investigation of the multi-exponential T2 decay in human white matter at 7 T: Implications for myelin water imaging at UHF. *NMR Biomed, 34*(2), e4429. doi:10.1002/nbm.4429

Voelker, M. N., Kraff, O., Goerke, S., Laun, F. B., Hanspach, J., Pine, K. J., . . . Quick, H. H. (2021). The traveling heads 2.0: Multicenter reproducibility of quantitative imaging methods at 7 Tesla. *Neuroimage, 232*, 117910. doi:10.1016/j.neuroimage.2021.117910

Wolff, S. D., & Balaban, R. S. (1989). Magnetization transfer contrast (MTC) and tissue water proton relaxation in vivo. *Magn Reson Med, 10*(1), 135-144. doi:10.1002/mrm.1910100113

Volz, S., Noth, U., Jurcoane, A., Ziemann, U., Hattingen, E., & Deichmann, R. (2012). Quantitative proton density mapping: correcting the receiver sensitivity bias via pseudo proton densities. *Neuroimage, 63*(1), 540-552. doi:10.1016/j.neuroimage.2012.06.076

Vymazal, J., Righini, A., Brooks, R. A., Canesi, M., Mariani, C., Leonardi, M., & Pezzoli, G. (1999). T1 and T2 in the brain of healthy subjects, patients with Parkinson disease, and patients with multiple system atrophy: relation to iron content. *Radiology, 211*(2), 489-495. doi:10.1148/radiology.211.2.r99ma53489

Yacoub, E., Shmuel, A., Pfeuffer, J., Van De Moortele, P. F., Adriany, G., Andersen, P., Vaughan, J. T., Merkle, H., Ugurbil, K., & Hu, X. (2001). Imaging brain function in humans at 7 Tesla. *Magnetic resonance in medicine*, *45*(4), 588–594. https://doi.org/10.1002/mrm.1080

Yarnykh, V. L. (2007). Actual flip-angle imaging in the pulsed steady state: a method for rapid three-dimensional mapping of the transmitted radiofrequency field. *Magn Reson Med, 57*(1), 192-200. doi:10.1002/mrm.21120

Yarnykh, V. L. (2010). Optimal radiofrequency and gradient spoiling for improved accuracy of T1 and B1 measurements using fast steady-state techniques. *Magn Reson Med, 63*(6), 1610-1626. doi:10.1002/mrm.22394

York, E. N., Thrippleton, M. J., Meijboom, R., Hunt, D. P. J., & Waldman, A. D. (2021). Quantitative magnetisation transfer imaging in relapsing-remitting multiple sclerosis: a systematic review and meta-analysis. *medRxiv*, 2021.2007.2014.21260512. doi:10.1101/2021.07.14.21260512

Zhou, X. J., Du, Y. P., Bernstein, M. A., Reynolds, H. G., Maier, J. K., & Polzin, J. A. (1998). Concomitant magnetic-field-induced artifacts in axial echo planar imaging. *Magn Reson Med, 39*(4), 596-605. doi:10.1002/mrm.1910390413

Zur, Y., Wood, M. L., & Neuringer, L. J. (1991). Spoiling of transverse magnetization in steady-state sequences. *Magn Reson Med, 21*(2), 251-263. doi:10.1002/mrm.1910210210